UNIVERSITÀ DELLA CALABRIA



University of Calabria
Department of Computer Science, Modeling, Electronics
and System Engineering

Doctor of Philosophy in
Information and Communication Technologies

Cycle
XXXI

Integration of Nanophotonic Devices on Silicon

Academic Discipline ING-INF/01

Coordinator
Prof. Felice Crupi .....

Thesis Supervisor
Prof. Giuseppe Cocorullo .....

Thesis Coadvisor
Dr. Ivo Rendina .....

Thesis Coadvisor
Dr. Emanuela Esposito .....

PhD Student
Dr. Valentina Di Meo .....

This thesis was evaluated by the two following external referees:

Stefania Campopiano, Professor, Parthenope University of Naples, Italy

Francesco Della Corte, Professor, Mediterranea University of Reggio Calabria, Italy

The time and effort of the external referees in evaluating this thesis, as well as their valuable and constructive suggestions, are very much appreciated and greatly acknowledged.

Integration of Nanophotonic Devices on Silicon
Ph.D. thesis defended on 20/06/2019. University of Calabria

© 2019 Valentina Di Meo. All rights reserved

This thesis has been typeset by LaTeX and the Sapthesis class.

Author's email: v.dimeo@dimes.unical.it

"Your time is limited, so don't waste it living someone else's life. Don't be trapped by dogma, which is living with the results of other people's thinking. Don't let the noise of others' opinions drown out your own inner voice. And most important, have the courage to follow your heart and intuition. They somehow already know what you truly want to become. Everything else is secondary."

"Il vostro tempo è limitato, per cui non lo sprecate vivendo la vita di qualcun altro. Non fatevi intrappolare dai dogmi, che vuol dire vivere seguendo i risultati del pensiero di altre persone. Non lasciate che il rumore delle opinioni altrui offuschi la vostra voce interiore. E, cosa più importante di tutte, abbiate il coraggio di seguire il vostro cuore e la vostra intuizione. In qualche modo loro sanno che cosa volete realmente diventare. Tutto il resto è secondario."

[Steve Jobs June 12, 2005]

Abstract

The purpose of this thesis research project has been the integration of photonic nanostructures on silicon substrate.

In particular, three different devices have been developed, whose application fields fall within the main research topics of silicon photonics. Indeed, a plasmonic biochemical sensor, an all-dielectric metamaterial for all-optical switching applications and a 1D photonic crystal as an interconnecting device have been successfully integrated on silicon substrate.

All of the proposed devices could lead to noticeable advances in silicon photonics, thanks to their potentiality for the development of integrated silicon-based nanodevices.

Contents

Introduction **xiii**

1 Overview on silicon photonic applications **1**
1.1 Optical sensing . . . 2
1.2 Telecommunication applications . . . 6
1.3 Intra- and inter-chip interconnections . . . 9

2 Nanofabrication technologies **15**
2.1 Lithography . . . 15
2.1.1 Optical lithography . . . 16
2.1.1.1 Optical lithography working principles . . . 16
2.1.1.2 Deep UV lithography . . . 18
2.1.1.3 Extreme UV lithography . . . 19
2.1.2 X-ray lithography . . . 20
2.1.3 Charged beam lithography . . . 21
2.1.3.1 Focused Ion Beam lithography . . . 22
2.1.3.2 Ion-solid interactions . . . 22
2.1.3.3 FIB equipment . . . 23
2.1.3.4 Resist-based FIB lithography . . . 24
2.1.3.5 FIB patterning by ion implantation . . . 24
2.1.3.6 FIB milling and gas-assisted processing . . . 25
2.1.3.7 Electron beam lithography . . . 26
2.1.3.8 EBL working principles . . . 26
2.1.3.9 Low-energy EBL . . . 29
2.1.3.10 EBL column . . . 30
2.1.3.11 EBL equipment . . . 32
2.2 Thin film deposition techniques . . . 35
2.2.1 Liquid-phase deposition techniques . . . 35
2.2.1.1 Casting coating . . . 35
2.2.1.2 Dip coating technique . . . 36
2.2.1.3 Spin coating technique . . . 36
2.2.2 Vacuum deposition technique . . . 38
2.2.2.1 Thermal evaporation . . . 38
2.2.2.2 Sputtering deposition . . . 39
2.2.2.3 Chemical Vapor Deposition . . . 41
2.3 Etching processes . . . 43

2.3.1 Wet etching processes 43
2.3.2 Dry etching process 44
2.3.2.1 RIE equipment 48

3 Integration of plasmonic and photonic devices on silicon substrate 51
3.1 Silicon-based plasmonic nanoantennas for biochemical sensing 51
3.1.1 Numerical simulations 53
3.1.2 Fabrication process 55
3.1.3 Device characterization 58
3.1.3.1 Small molecules sensing 59
3.1.3.2 Large molecules sensing 60
3.1.4 Conclusions and future perspective 62
3.2 Silicon-based dielectric metasurface for all-optical switching 63
3.2.1 Numerical simulations 64
3.2.2 Fabrication process 66
3.2.3 Device characterization 69
3.2.4 Conclusions and future perspectives 72
3.3 Silicon based dielectric grating as interconnect device 72
3.3.1 Distributed Bragg reflection theory applied to PhCs 74
3.3.2 Numerical simulations 78
3.3.3 Fabrication process 82
3.3.4 Device characterization 90
3.3.5 Conclusions and future perspectives 93

Conclusions 95

List of Publications 97
Bibliography 99

List of Figures

1.1 Schematization of the operation principle of a silicon photonic biosensor. 2
1.2 Schematic view of a microring resonator. 3
1.3 Schematization of a micro disk resonator structure. 3
1.4 Schematization of a Bragg grating resonating structure. 4
1.5 Schematization of a SWG sensing platform. 4
1.6 Schematization of interferometric sensors. 5
1.7 Schematization of PC sensing platforms. 5
1.8 LSPR working principle. 6
1.9 Schematization of III-V quantum dots Ge-on-Si laser device. 7
1.10 Picture of switches integrated on silicon substrate. 8
1.11 Picture of ring resonator optical filters. 8
1.12 Schematization of a waveguide-integrated Ge-on-Si detector. 9
1.13 Schematic view of several silicon photonics waveguides configurations. 10
1.14 Schematization of device structures of silicon optical modulators. . . 11
1.15 Schematization of power splitters. 12
1.16 Schematization of beam splitters. 12

2.1 Schematization of the photon wavelength spectrum. 16
2.2 Schematization of optical lithographies. 17
2.3 Comparison between dry and immersion project optical lithography. 18
2.4 Schematization of a EUV lithography system. 19
2.5 Schematization of an X-ray lithography system. 20
2.6 Schematization of ions-solid interactions. 23
2.7 Shape of the LMIS emitter tip without and with the Taylor cone. . . 23
2.8 SEM image of an implanted and etched line space pattern. 25
2.9 Schematization of the scattering events. 26
2.10 Dose correction for proximity effect. 28
2.11 Negative pattern biasing correction. 28
2.12 Monte Carlo simulation of the electron trajectories for different keV. 29
2.13 Schematization of a typical SEM column. 30
2.14 Schematization of the magnetic and electrostatic lenses. 31
2.15 EBL Raith 150 system. 32
2.16 Schematization of vector and raster scan mode. 33
2.17 Load lock and sample holder of the EBL Raith 150 system. 33
2.18 Raith software for exposure parameters settings. 34
2.19 Schematization of drop casting technique. 35

2.20 Schematization of the dip coating technique. 36
2.21 Schematization of spin coating process. 37
2.22 Deposition of PMMA on 1 cm x 1 cm Si substrate. 38
2.23 Schematization of the film growth by thermal evaporation. 38
2.24 Schematization of a thermal evaporation system. 39
2.25 Schematization of a DC sputtering system. 40
2.26 BAL-TEC SDC 500 sputter coater. 41
2.27 Schematization of a CVD process. 42
2.28 Schematization of the wet etching process. 43
2.29 Schematization of an undercut profile due to the over etching. 44
2.30 Schematization of dry etching plasma mechanisms. 44
2.31 Schematization of a typical RIE system. 45
2.32 Schematization of the etching of silicon. 46
2.33 Silicon etching rate trends. 47
2.34 Oxford Plasmalab 80 Plus RIE system. 48

3.1 Schematization of the simulated cross-shaped NAs array. 53
3.2 Simulated reflectivity response of the metasurfaces. 54
3.3 Fabrication flow chart for gold NAs fabrication. 55
3.4 Photograph and micrograph of fabricated devices. 56
3.5 SEM images of the L = 850 nm NAs array. 57
3.6 SEM images of the L = 1100 nm NAs array. 57
3.7 AFM analysis of NAs array. 57
3.8 Comparison of reflectance curve for naked NAs arrays. 58
3.9 Reflectance curves of Au NAs. 59
3.10 Reflection curves before and after the regeneration process. 60
3.11 Reflectance of the gold NAs array in air and with PMMA. 61
3.12 2D plots of the electric field intensity distribution on the NA unit cell. 62
3.13 Designed metamaterial and transmission spectrum changes. 64
3.14 Unit cell used for the numerical simulation and optical response. . . 65
3.15 GeTe refractive index. 66
3.16 Nanorod fabrication flow chart. 67
3.17 SEM images of the Cr mask before the RIE process. 68
3.18 SEM images of the Si nanorod on SOI substrate after the RIE process. 68
3.19 AFM analysis of the fabricated device before GeTe deposition. . . . 69
3.20 Measurement setup of the reflection from SOI-GeTe. 70
3.21 Reflection measurement of the GeTe/SOI hybrid structure. 70
3.22 Raman spectra for the amorphous and crystalline flat layers of GeTe. 71
3.23 Crystal dispersion surface close to the Bragg condition. 76
3.24 Grating parameters schematization. 77
3.25 α variations vs n_1. 78
3.26 α variations vs Δn. 79
3.27 α variations vs d/a ratio. 79
3.28 Contour plot of refractive index profile of the proposed structure. . . 80
3.29 Output vs Input angular variation. 81
3.30 Vertical field confinement inside the structure. 82
3.31 Superprism-based grating fabrication flow chart. 83

3.32 SEMCO Minilab DF 500 equipment for LTO deposition. 83
3.33 Elettrorava - MVSystem employed for the deposition of SiC films. . 84
3.34 Thickness map of PECVD a-SiC:H film and LTO film on Si substrate. 85
3.35 Ellipsometric characterization of deposited SiC film 85
3.36 A failed lift-off process due to the strong PMMA adhesion. 85
3.37 A lift-off process successfully carried out on SiC substrate 86
3.38 SEM image of the chrome mask after the lift-off process. 87
3.39 SEM metrological analysis after lift-off process. 88
3.40 A SEM overview image of the fabricated device after the RIE process. 89
3.41 SEM metrology of the etched device. 89
3.42 AFM analysis of SiC grating. 89
3.43 SEM image of the measured device. 90
3.44 Schematization of the preliminary measurement setup. 90
3.45 Picture of the measurement setup. 91
3.46 SEM image of the device edges cut and polished with FIB milling. . 91
3.47 Measurement setup used to characterize the FIB-milled device. . . . 92
3.48 SEM image of the input surface after cut and FIB milling. 92

Introduction

Silicon photonics is achieving an increasing relevance for the strategic fields of telecommunications, microelectronics and microsystems. In the optical telecommunication field, it allows to develop optoelectronic systems in which optical and photonic components are integrated in an efficient and low-cost way thanks to the well-established silicon microtechnologies. It is expected to play a central role also in microelectronics, where the progressive trend towards nanometric dimensions of Si electronic devices and the consequent increase of their on-chip density, determine an unwanted raise of interconnection lengths with a consequent delay in the signal propagation and a large amount of power density dissipated by joule effect that strongly limit further integration capabilities.

Silicon photonics in perspective could allow to overcome these limits by replacing the current electrical on-chip interconnections with optical interconnections characterized by high data rates, electromagnetic interference free operation, and no thermal dissipation. Moreover, thanks to the advanced micromachining techniques and to the excellent electrical, optical, mechanical and thermal properties of silicon, silicon photonics is assuming a growing interest in the development of microsystems with advanced sensing and actuation capabilities.

The aim of this thesis work has been the study of the fabrication technologies that allow to transfer micro- and nano-patterns on silicon substrates in order to develop silicon-based optical devices that can be of great interest for the main application fields of silicon photonics, that is: (i) sensing, (ii) telecommunications, and (iii) on-chip interconnects.

The outline of this thesis is therefore the following:

- in *Chapter 1*, a short review of the state-of-art and recent developments of the three main application fields of silicon photonics highlighted before (sensing, telecommunications, and on-chip interconnects) is reported;

- in *Chapter 2*, an overview of the most employed micro- and nanofabrication technologies is presented, with a particular attention to the systems and techniques employed for the development of the proposed devices;

- in *Chapter 3*, the description of the development of three silicon-based devices, whose applications fields fall in the three main topics highlighted in Chapter 1, is reported.

In particular, the first proposed device is a plasmonic sensor developed for infrared biochemical sensing applications. This sensor is constituted by a large area

bidimensional array of gold nanoantennas deposited on a silicon substrate able to perform Surface Enhanced InfraRed Absorption (SEIRA) spectroscopy. Thanks to the extraordinary capabilities of Electron Beam Lithography (EBL) patterning, it has been possible to tune the plasmonic response of the proposed array in two different regions of the infrared spectrum in order to perform the detection of small and large molecules, as it will be shown in the first Section of Chapter 3.

Another proposed device is a dielectric silicon-based metasurface developed for all-optical switching application. This metasurface is constituted by an array of silicon nanorods covered by a layer of a phase change material (PCM), in particular a thin film of germanium telluride (GeTe). The switching between the two room-temperature stable phases of GeTe (crystalline and amorphous), provided by the thermal heating of the structure, induces a variation of the device reflectance at $\lambda = 1.5$ µm.

Finally, the last proposed device is a one-dimensional photonic crystal (PhC) able to steer light without mechanical moving parts. In particular, this PhC is a grating constituted by alternating pillars of silicon carbide (SiC) and air fabricated on a silicon substrate with a SiO_2 film interposed between them as an optical buffer layer for the vertical confinement of light. The grating is designed to work in an in-plane configuration at $\lambda = 1.55$ µm. Moreover, a hyperbolic output surface has been designed in order to mimic the dispersion surface of the PhC and therefore to maximize the angular amplification of the proposed device, defined as the ratio between the output angular deviation and the input angular deviation.

Finally, the conclusions will summarize the results obtained in this thesis work, showing moreover the future perspectives for the three proposed devices.

Chapter 1

Overview on silicon photonic applications

Silicon (Si) is one of the most employed materials for both microelectronic industries and academic research. Silicon chips are cheap and easy to fabricate with an extremely high throughput thanks to the strong development of the fabrication technologies. Indeed, Moore's law is still valid, with the integration of more than 23 billion of transistors on the Graphcore G12C processor [1]. However, these extraordinary integration capabilities are nowadays mainly affected by the parasitic effects provided by the metallic interconnections between the devices, in particular those regarding heat (and hence power) dissipation, the signal attenuation and, above all, the bottleneck to higher data rate constituted by the length of such interconnections [2]. To overcome these issues, one of the possible solutions is to use optical interconnections instead of electrical ones: photons are therefore preferred to the electrons to carry data between different chips or either within the same chip. Photons can travel at the velocity of light without interfering with the electromagnetic field, allowing the optical systems to achieve higher data rates and also better stability than electrical ones [3]. For these reasons, high efforts have been made to integrate both optical and electrical components on silicon chip with the use of the existing standard semiconductor fabrication technologies, which can guarantee low-cost and large-scale manufacturing capabilities. Moreover, silicon is optically transparent in the wavelength window between 1100 nm to 7000 nm, approximately, which makes its use very interesting even for applications below the near infrared (NIR) range of optical telecommunications (whose band lies into the wavelength window between 1300-1500 nm). This property, together with silicon large optical damage threshold and good thermal conductivity, makes silicon an excellent candidate for the photonic integration. Indeed, since the mid-1980's silicon photonics has been widely investigated [4], giving rise to remarkable results especially for the development of Si-based waveguide, switches and modulators [5, 6, 7]. Besides the results obtained so far in telecommunication and optical interconnection fields, silicon photonics is very attracting also for sensing applications [8], thanks to its potential to obtain, also in this case, low-cost and highly integrated devices suitable for point-of-care and home healthcare diagnostic applications.

In the following subsections, a short overview of the recent development of silicon

photonics will be presented to highlight the relevance of its applications to sensing, telecommunications and on chip interconnects.

1.1 Optical sensing

Optical sensing techniques allow high-sensitivity, non-contact and electromagnetic interference free measurements. In an optical sensor, the interaction between the sensing area and the local environment produces a variation of the intensity, or phase, or resonance wavelength, or polarization (or either a combination of these features) of the optical field. A processing unit is then used to elaborate the optical collected signal and extract the desired information.

Recently, silicon photonic biosensors have been the objective of an intensive research for their potential use in healthcare and basic biomedical research [9, 10]. New configurations rely on the near-infrared confinement of light within a nanometer-scale waveguide, often using optical resonant structures sensitive to the change of the local refractive index (RI). Part of the light travels also outside the waveguide as an evanescent wave; when a molecular interaction takes place on the waveguide surface, a change of the RI within the evanescent field occurs, resulting in a shift of the resonant wavelength that is proportional to the mass of the binding analyte. The principle of operation of a silicon photonic biosensor is show in Fig. 1.1 [11].

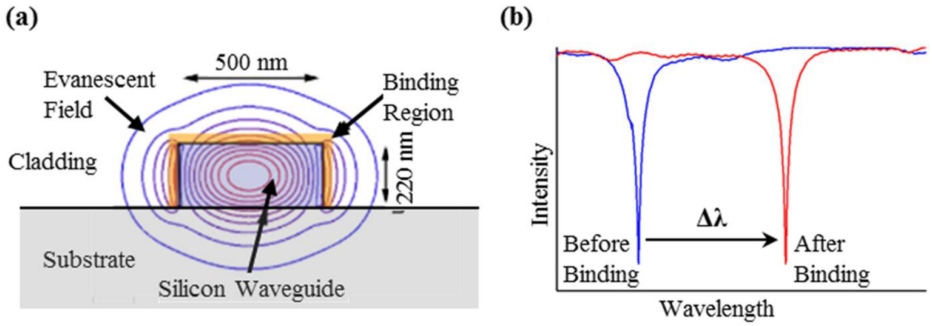


Figure 1.1. Schematization of the operation principle of a silicon photonic biosensor. a) shows the evanescent field traveling outside the waveguide within the binding region. b) shows the change of the resonance wavelength due to a binding event [11].

A large variety of optical structures have been developed for biosensing applications. Microring resonators (schematically shown in Fig. 1.2 [12]) have attracted wide interest for their use as biological sensors [13, 14]. They consist of an optical circular waveguide coupled with a straight waveguide; the resonant condition occurs when the optical length of the resonator is equal to a multiple of the wavelength. Waveguides sustaining transverse magnetic (TM) modes offers sensitivities three times higher than transverse electric (TE) ones due to the higher evanescent field component traveling outside the waveguide [15]. However, using thinner waveguides it is possible to obtain lower confinement of TE modes, leading to a deeper penetration of the evanescent field into the waveguide cladding and hence an enhanced sensitivity [11].

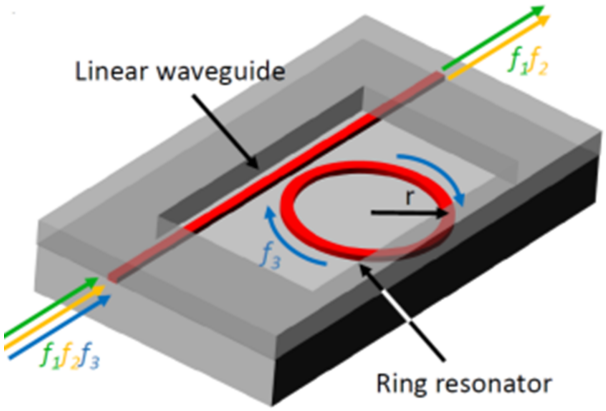


Figure 1.2. Schematic view of a microring resonator [12].

A similar approach is followed by the micro disk resonating structures (schematically shown in Fig. 1.3 [12]), where a circular disk is used as a resonant cavity instead of a single-mode circular waveguide [16]. Differently from microring resonators, the field here is confined along the disk perimeter, being therefore in contact with only one sidewall offering higher sensitivity and quality (Q-) factor, due to the lower scattering losses [17]. Both TE and TM modes can be sustained by the waveguide depending on its geometry; however, bending scattering losses are higher for TM modes which therefore require higher disk radii increasing the generally small footprint offered by this configuration.

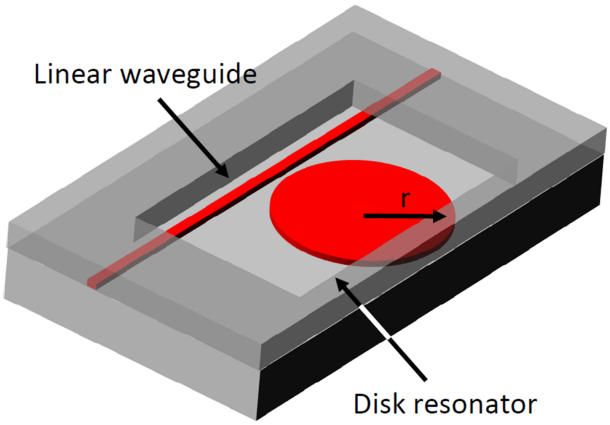


Figure 1.3. Schematization of a micro disk resonator structure [12].

A different configuration is represented by a Bragg grating structure (schematically shown in Fig. 1.4 [12])[18]. The RI modulation (generated with a periodical variation of the waveguide dimensions or materials) creates reflections at each boundary; the periodicity of the structure multiplies these reflections creating a stop band for the transmitted light at a precise wavelength. By adding a phase shift at the center of the structure, a narrow transmission peak appears into the stop band that can be used for RI variation monitoring.

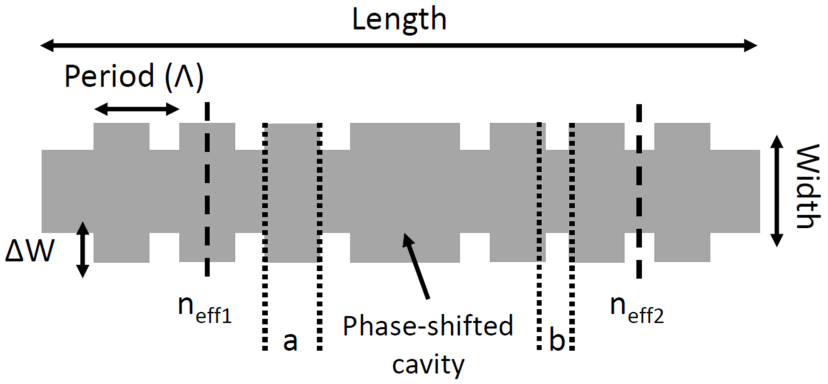


Figure 1.4. Schematization of a Bragg grating resonating structure [12].

Another interesting structure for silicon photonic biosensing is the sub-wavelength grating (SWG, schematically shown in Fig. 1.5 [12]), whose core is periodically structured with a period that does not match the resonance condition but is much lower than the wavelength [19]. By interposing silicon blocks with a lower refractive index material, the resulting effective refractive index is reduced, and this in turn leads to a weaker confinement and hence to a higher RI sensitivity [20].

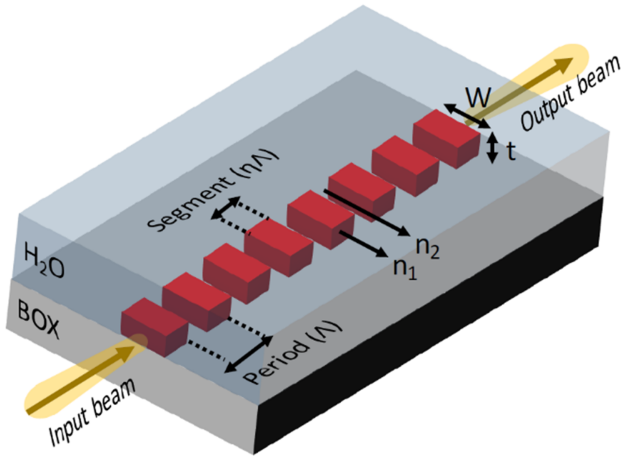


Figure 1.5. Schematization of a SWG sensing platform [12].

In addition to resonant structures, interferometric-based biosensors constitute a large part of integrated-optic approaches for sensing applications [21]. Young and Mach-Zehnder configurations (schematically shown in Fig. 1.6 [12]) are the most common formats [22]: both interferometers split source light into two single-mode waveguides, one acting as a sensing arm while the other acting as a reference. The evanescent field in the sensing arm is sensitive to the RI changes occurring at its interface. This generates a phase shift of the wave traveling into the sensing arm respect to that traveling into the reference one. However, in Mach-Zehnder based interferometers the output light is recombined through another Y-junction, while in Young interferometers the output light is usually projected onto a charge-coupled device (CCD) or CMOS camera, producing an interference pattern.

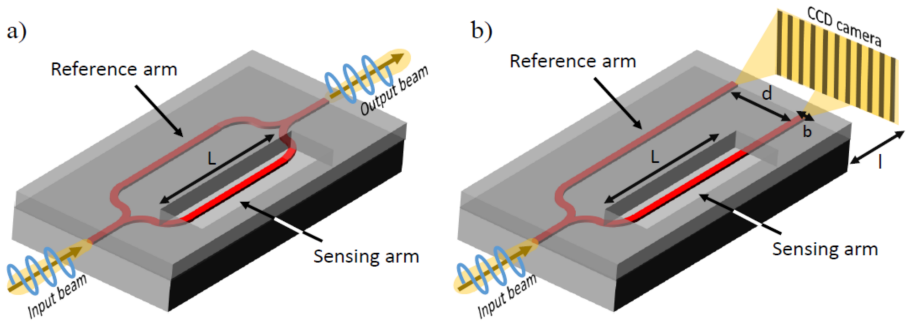


Figure 1.6. Schematization of interferometric sensors. a) shows a typical Mach-Zehnder interferometer. b) shows a Young interferometer [12].

In addition, photonic crystal (PhC) biosensors (schematically shown in Fig. 1.7 [12]) have been widely investigated as a promising sensing platform [23, 24]. A PhC waveguide consists of a periodical arrangement of dielectric structures producing a modulation of the effective refractive index which, in turn, causes a stop band for the transmission or reflection spectrum for certain wavelengths. The periodicity can be one-dimensional (1D), bi-dimensional (2D) or either three-dimensional (3D); the most common configurations, however, are 1D and 2D ones due to their lower manufacturing complexity.

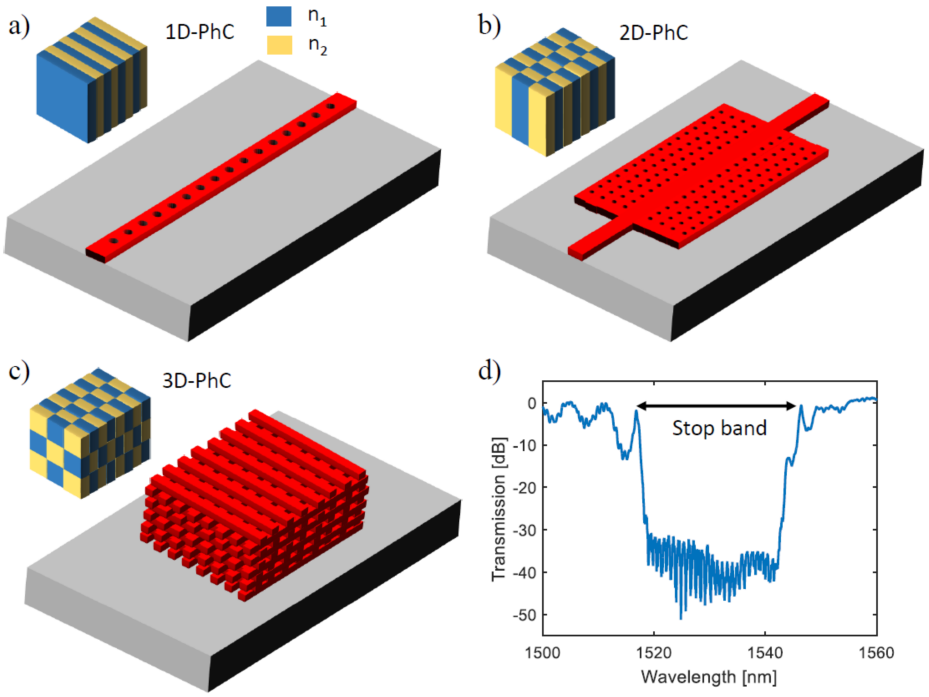


Figure 1.7. Schematization of a) 1D PC sensing platform, b) 2D PC sensing platform, c) 3D PC sensing platform. d) shows a typical transmission spectrum [12].

Compared to other sensing platform, PCs show lower sensitivities; on the other hand, they can be easily integrated on chips with high throughput, allowing the detection of small amounts of analytes, or even a multi-analyte detection [25].

Finally, the interaction of light with subwavelength metallic nanostructures is raising higher interest due to their capability to control the flow of light and to confine it well below the limit of diffraction [26]. Indeed, in noble metal nanoparticles, an incident electrical field induces the oscillation of the metal free electrons, the so-called Localized Surface Plasmon Resonance (LSPR). Such resonance depends on nanoparticle's size, geometry and composition, and leads to highly localized fields that are several orders of magnitude higher than the incident one. These nanostructures can be also disposed in 2D (metasurface) or 3D (metamaterial) periodical arrangements that allow to arbitrarily tailor their optical response. The integration of plasmonic elements on silicon chips therefore can introduce enormous benefits, for example thanks to the ultra-high degree of miniaturization offered by these nanostructures and thanks to their giant nonlinearities [27]. Moreover, LSPRs are particularly indicated for biosensing, since plasmonic resonance is highly sensitive to environmental RI changes, as it is schematically shown in Fig. 1.8 [28].

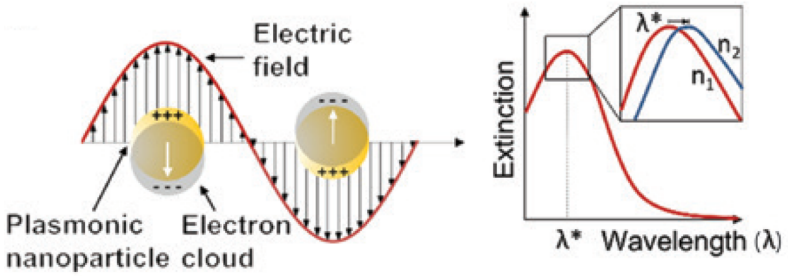


Figure 1.8. LSPR working principle [28].

As it will be better explained in Chapter 3, part of this thesis work has been devoted to the development of a new photonic sensing configuration, named Surface Enhanced InfraRed Absorption (SEIRA) spectroscopy, where an array of plasmonic nanoantennas supporting LSPRs has been integrated on a Si substrate for sensing purposes.

1.2 Telecommunication applications

In the field of telecommunication, devices able to perform photonic signaling and processing are strongly required.

One of the most challenging issue is the development of an on-chip laser source since, unfortunately, the silicon is an indirect bandgap semiconductor with poor emitting efficiency [29]. One of the first technology implemented for the development of silicon photonic laser has been the stimulated Raman-based lasers [30]; however, due to the intrinsic optical pumping mechanism of stimulated Raman scattering (SRS) at the base of these devices, silicon Raman lasers do not fulfill the requirements needed for practical applications. Another technology for laser applications is rare-earth silicon doping, typically using erbium doped silicon materials or erbium

compounds [31, 32]. However, erbium shows low emitting efficiency too, causing erbium-based lasers to be not practical for real applications. On the contrary, a more realistic chip laser can be obtained by using germanium-on-silicon (Ge-on-Si) lasers [33]: indeed, although Ge is an indirect bandgap semiconductor too, its band can be engineered giving rise to a fast development of Ge-on-Si lasers integrable with CMOS process [34]. Anyway, the most practical laser source is constituted by III-V semiconductor-based lasers, owing to their direct bandgap structure [35]. The main disadvantage of this kind of lasers lies into the integration approaches, that would be affected by submicron precision alignment mismatch between the lasers and silicon waveguides for direct mounting integration, or high costs for high-quality bonding. Until now, the most efficient integration approach for III-V semiconductor lasers is hetero-epitaxial growth [36, 37], which allowed the fabrication of InAs/GaAs quantum dots (QDs) lasers with an output power larger than 100 mW and high temperature stability. In Fig. 1.9 [37], a schematization of the laser device developed by Liu et al. is shown, together with its photoluminescence spectrum.

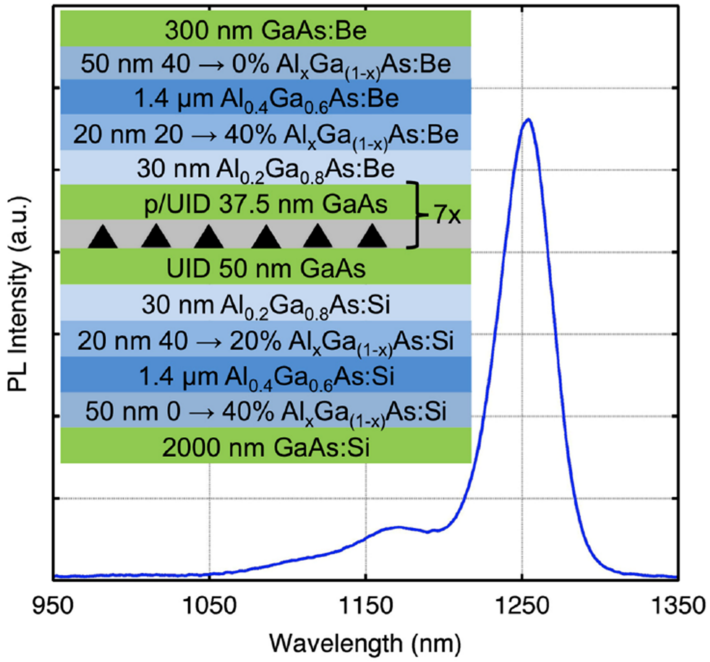


Figure 1.9. Schematization of III-V quantum dots Ge-on-Si laser device with its room temperature photoluminescence spectrum [37].

Another very important device for the signal processing is the optical switch, which can route signals from multiple inputs toward multiple outputs. Generally, silicon photonic switches can be divided into thermo-optic (TO) and electro-optic (EO) switches, where the former show low crosstalk and low insertion loss, while the latter have fast reconfigurability responses. The first researches on optical switches were focused on thermo-optic devices, based on cascaded Mach-Zehnder interferometers [38]; recently a 64 x 64 thermo-optic switch has been demonstrated with a 180-nm CMOS process showing very low crosstalk and insertion loss [39]. Regarding electro-optical switches, the first developed device shown a switching time

of 4 ns [40]; actually, 32 x 32 electro-optic switches with 1.2 ns switching time have been developed [41]. In Fig. 1.10 [39], pictures of these optical switches are shown.

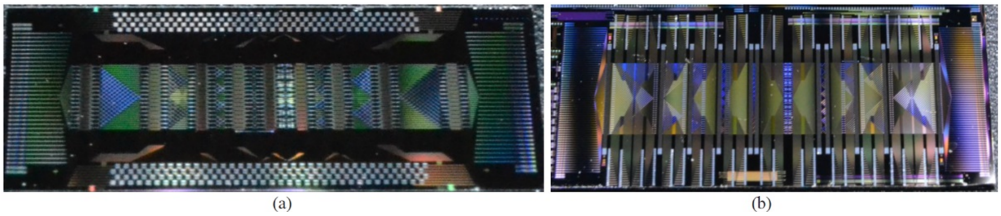


Figure 1.10. Picture of a) 32 x 32 EO switch and b) 64 x 64 TO switch integrated on silicon substrate [39].

Very recently, microelectromechanical systems (MEMS)-actuated 64 x 64 silicon photonic matrix of switches has been demonstrated [42], but the performances of this kind of switches must be enhanced in terms of switching time and insertion losses. Due to the relevance of this application, an all-optical switch constituted by a dielectric metasurface integrated on a silicon-on-insulator (SOI) substrate has been developed during this thesis, as it can be seen in Chapter 3.

Another key element in telecommunication applications is the optical filter, due to its potential application in noise reduction [43], signal quality improvement or on-chip networking [44]. The most common types of optical filters are based on resonant structures, like arrayed waveguide gratings (AWG) [45], Fabry-Perot cavities [46], ring resonators [47], photonic crystal microcavities [48], or multimodal interference (MMI) devices [49]. Recently, a silicon photonic comb filter has been demonstrated with both wavelength and bandwidth tunable by adjusting the phase shifters of the Fabry-Perot cavity structure on which it is based [50]. In Fig. 1.11 (from [51]) a picture of a microring resonator optical filter is shown as an example of a resonating structure employed for optical filtering.

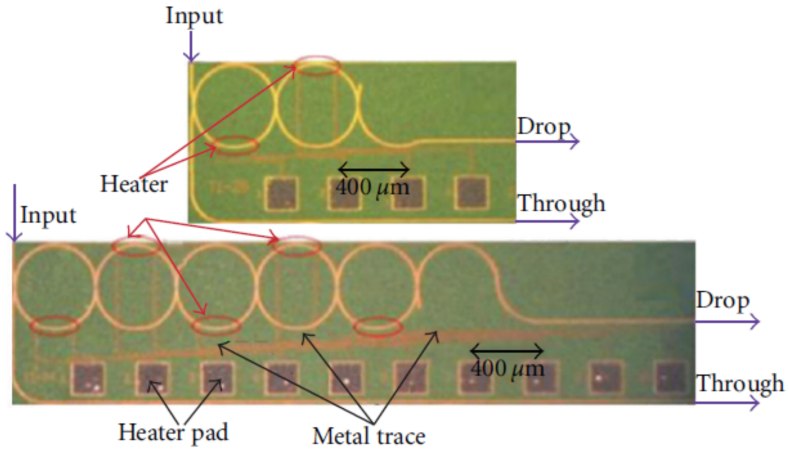


Figure 1.11. Picture of a 2^{nd} order (on top) and 5^{th} order ring resonator optical filter [51].

In telecommunication applications, detectors are fundamental elements for the conversion of optical signals into electrical ones in order to perform further signal processing. Since silicon is transparent in telecommunication range (1300-

1500 nm), other approaches have to be considered for the photon detection. Generally, these approaches can be divided in three different categories: Schottky structures, III-V heterogeneous detectors and Ge-on-Si detectors. Schottky metal-silicon (MS) structures have been the first developed devices for integrated detection, and several methods have been implemented to improve their quantum efficiency: the use of resonant cavities [52], the merging with dielectric waveguides [53], the use of transparent electrodes [54], or through surface plasmon polaritons [55], with a responsivity of ~ 0.1 A/W.

Another solution for the development of optical detectors is based on the use of III-V semiconductors. Previously, the most III-V detectors were fabricated on GaAs substrates, which however is not compatible with CMOS manufacturing, but recently InGaAs detectors have been successfully built on silicon-on-insulator (SOI) substrates with CMOS technology, showing a responsivity of more than 1 A/W [56]. Ge-on-Si detectors are the most studied devices for optical detection due to the excellent optoelectronic properties of Ge [57]; the first developed devices were all normal-incidence detectors, were light was launched into the detector through fiber or free-space coupling [58]. To achieve higher integration, waveguide-integrated Ge-on-Si detectors have been developed, which offer also high-speed operation and high quantum efficiency. In particular, three different coupling schemes have been proposed: in the first one, silicon waveguides lie on Ge detector, and the light coupling occurs through the evanescent wave [59]; in the second one, that shows the highest coupling efficiency, Si waveguides are butt-coupled to Ge-detector [60]; in the third one, the most employed configuration due to CMOS process compatibility, silicon waveguides lie under the Ge detector [61]. This kind of detector is able to achieve simultaneously high responsivity (~ 1 A/W) and high bandwidth (~ 70 GHz). A schematic view of this configuration is shown in Fig.1.12 [62].

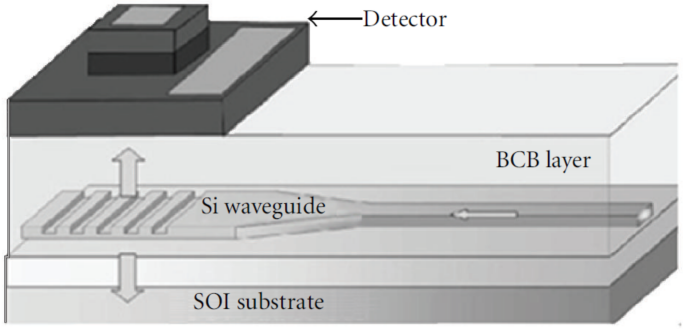


Figure 1.12. Schematization of a waveguide-integrated Ge-on-Si detector[62].

1.3 Intra- and inter-chip interconnections

Copper-based electrical interconnects have dominated the short-range communication links in the last four decades; however, they are actually constituting a bottleneck due to the very high data rate demand raised over the last decade. For this reason, silicon photonic optics interconnections are attracting a lot of atten-

tion as a potential solution to the high data rates beyond the Terabit per second threshold [63].

Obviously, for interconnection applications, waveguides are the basic elements to be realized to carry signals from one side of the chip to another. Some of the most utilized waveguide configurations are:

- silicon strip waveguides [64], typically used for compact optical routing;
- rib waveguides [65], that allow to realize electrical connections on the side of the waveguide;
- slot waveguides [66], that introduce a supplementary degree of freedom in waveguide cross section respect to strip and rib waveguide which allow to tailor their non-linearity;
- photonic crystal waveguides [67], where light/matter interaction is enhanced due to the slowdown of light occurring in these structures;
- subwavelength gratings (SWG) waveguides [68], where it is possible to customize the guided mode in z-direction;
- SWG slot waveguides [69], that show a lower non-linearity respect to SWG waveguides;
- surface plasmon polariton waveguides [70], that allow an even stronger light confinement.

All of these configurations are summarized in Fig. 1.13 [63]:

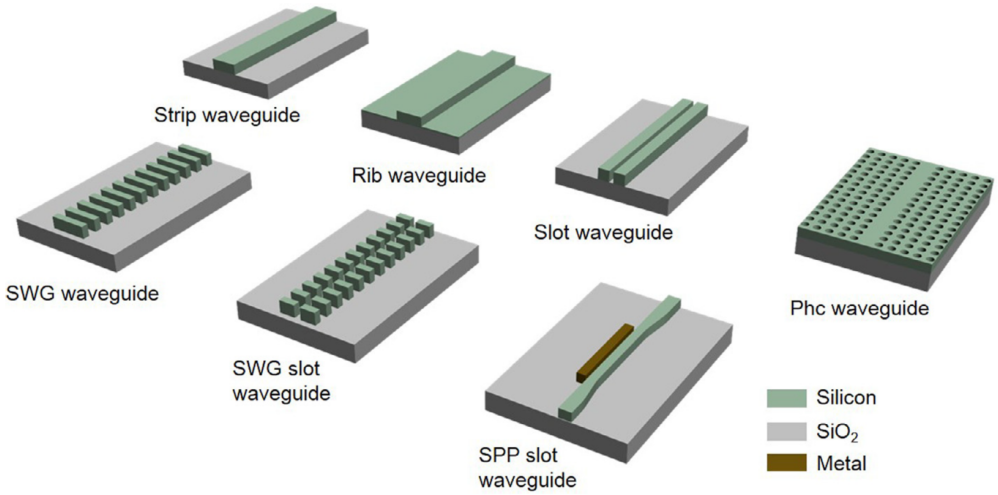


Figure 1.13. Schematic view of several silicon photonics waveguides configurations [63].

Another fundamental device for optical interconnections is the optical modulator, that allows to change the fundamental parameters of an optical beam traveling in free space or in an optical waveguide [71]. Since silicon's linear electro-optic coefficient is weak, the suitable methods to achieve modulation in silicon are thermo-optic effect

and plasma dispersion. Indeed, owing to the large thermo-optic coefficient of silicon, it is possible to develop tunable thermo-optic silicon modulators [72], but their modulation speed is not high as required by telecommunication applications. Plasma dispersion is therefore the most employed method to achieve optical modulation in silicon, due to the dependence of both real and imaginary part of silicon refractive index on the concentration of free carriers. There are two ways for converting a RI change into an intensity modulation: with a Mach-Zehnder interferometer, where the relative phase of two travelling waves is shifted by changing the RI of one or either both waveguide arms [73], or by using a cavity enhancement with resonant structures [71].

Carrier injection is the most sophisticated technology to vary free carrier concentration of p-i-n structures; silicon optical modulators based on this effect show a uniform index modulation, but limited operation speeds (up to 10 Gb/s) and high power consumption [74]. The first silicon optical modulator with a bandwidth up to GHz has been fabricated by Intel [73] in 2004; it was based on carrier accumulation in a MOS structure. The performances of this device have been optimized and recently a modulator with modulation speed up to 25 Gb/s has been demonstrated [75].

Actually, the most popular technique for manipulating free-carrier density is carrier depletion, obtained by applying a negative bias voltage to a p-n or p-i-n structure. These devices offer modulation speed up to 60 Gb/s, but with lower modulation efficiency respect to the other configurations[76]. In Fig. 1.14 [71] a schematization of the three methods described so far is shown.

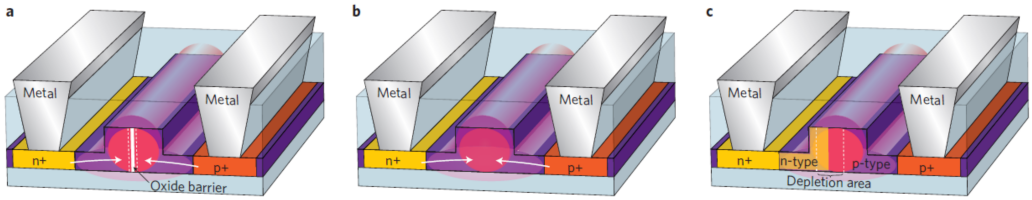


Figure 1.14. Schematization of the typical device structures implementing: a) carrier accumulation; b) carrier injection; c) carrier depletion mechanism for the modulation of free-carrier density in silicon optical modulators [71].

In addition to plasma dispersion-based modulators, a new approach for the implementation of ultra-compact optical modulator is based on the slow-light effect achievable in photonic crystal devices. Indeed, modulation speed up to 40 Gb/s can be achieved in 90 µm long PC devices [77], and modulation speed up to 100 Gb/s can be achieved by combining slow light SOI structures with organic polymer in silicon-organic hybrid (SOH) structures [78], that are very competitive structures for silicon photonics modulating devices.

A device of relevant importance is the power divider, which distributes signals to different chip area. Different configurations have been implemented so far, like Y-junctions [79], adiabatic 3 dB couplers [80], MMI-based structures [81]; such configurations are schematically shown in Fig. 1.15 [63]. Due to their compact size, low losses, large bandwidth and higher fabrication errors tolerance, adiabatic couplers and MMI-based devices are the most employed configurations.

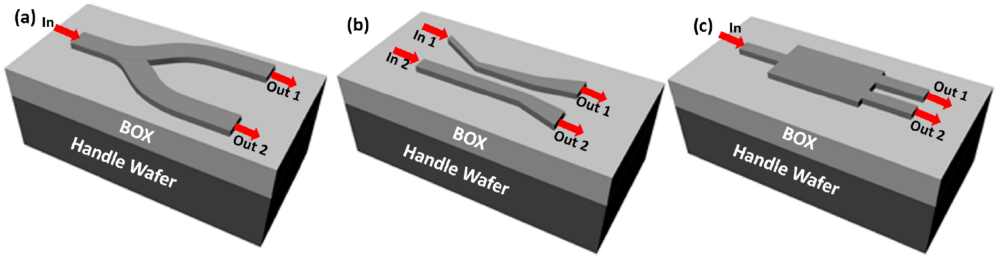


Figure 1.15. Schematization of: a) a Y-junction power splitter; b) a 3-dB adiabatic coupler; c) a MMI-based power splitter [63].

In addition, integrated polarization beam splitters are other key elements that allow to split the orthogonal polarization components of an input beam in two separate output beams [82]. Grating-based polarization beam splitters allow the simultaneous coupling of light and polarization splitting [83]; when a separate polarizing splitter is needed, instead, the most employed structure is a MMI based on self-imaging principles, that allow also high-density integration and more fabrication tolerances [84]. Indeed, in these kind of polarization splitters dimensions lower than 10 µm are required, unlike the long coupling length (> 100 µm) required from a directional coupler [85]. In Fig. 1.16 [63] a schematization of the two structures described so far is shown.

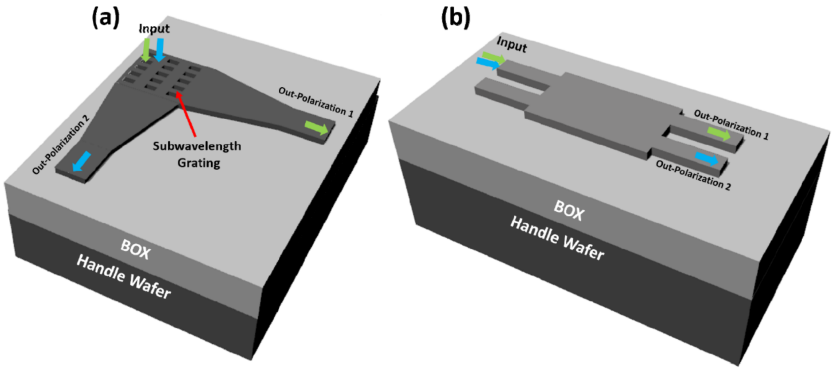


Figure 1.16. Schematization of: a) a grating-based polarization beam splitter; b) an MMI-based polarization beam splitter [63].

Even more important than power dividers are the beam steering devices to effectively address the light on a chip. Few proposals are reported in literature, mostly based on mechanical systems [86] or liquid crystal devices [87]. In this thesis, a new approach based on a silicon carbide (SiC) photonic crystal integrated on a Si chip is proposed. Details about device simulation and fabrication are reported in Chapter 3.

The integration of all the devices seen so far has been made possible thanks to the extraordinary advance of technological fabrication capabilities. Indeed, several sophisticated lithographic methods have been developed, together with thin film deposition techniques and etching processes that allowed powerful miniaturization capabilities, high reproducibility and, at the same time, acted as a technological driver

for further researches and technological improvements. In the following chapter, a short overview of the most employed micro- and nanofabrication techniques will be shown, with a particular attention to the methods employed for the fabrication of the nanodevices proposed in this thesis.

Chapter 2

Nanofabrication technologies

Nanotechnology deals with materials and systems at nanometer scale, by controlling and creating materials, devices and structures around this size. Generally, top-down nanofabrication techniques allow to transfer a pattern to a substrate, with at least one dimension less than 100 nm [88]. A typical top-down fabrication process consists of four successive steps:

- the coating of a substrate with an irradiation-sensitive polymer layer (the resist);
- the exposure of the resist with light or a charged beam;
- the development of the resist with a proper chemical solution;
- the transfer of the pattern from the resist layer to the substrate through additive techniques or subtractive techniques.

In this chapter, an overview of several fabrication processes will be presented, starting from the lithographic processes, which allow to transfer the design of the nanostructure to a sacrificial resist layer. The pattern obtained into the resist can then be transferred to the substrate through additive methods, which require the deposition of thin films on the substrate, or through subtractive methods, which instead require a selective etching of the substrate material. This chapter is not an exhaustive overview, but it is aimed to introduce the main fabrication processes employed for the fabrication of the devices developed in this work of thesis.

2.1 Lithography

The lithography process is the step used to transfer the device design to a sacrificial layer before transferring it to the substrate or, for some lithographic approaches, to transfer the device design directly to the substrate. Several lithographic techniques have been developed so far; they however can be divided in two main categories: optical lithography and charged-beam lithography. In both lithographic techniques, a thin polymeric resin film (the resist) is impressed by an impinging beam (light for photolithography or charged particles for charged-beam lithography); the absorption of light or the scattering of the charged particles will modify the chemical properties

of the polymeric film by changing its solubility in a developer solution. In particular, two different kinds of resist exist: the positive resists, that become soluble after the lithographic process due to the scission of their polymeric chains caused by the energy deposition provided by the source, or the negative resists that, on the contrary, become insoluble after the lithographic process due to the cross-linking of the polymeric chains. The resolution capabilities of the different lithographic processes will therefore depend not only on the performed process, but also on the resist intrinsic properties, especially for the charged-beam lithography.

In the following subsections, the basic principles of these lithographic processes will be presented, together with the correlated advantages and disadvantages.

2.1.1 Optical lithography

The optical lithography, called also photolithography, uses photons to transfer a geometrical pattern to a light-sensitive polymer, the photoresist. In order to selectively expose the resist, a mask with opaque and transparent areas (made, as example, of chromium on a glass substrate) is needed; for positive photoresists the mask will be transparent only in the areas where the resist must be removed, while for negative resists the mask must be opaque where the resist must be soluble. Depending from the size of the pattern to be realized, different wavelengths for the impinging photons must be considered, as it can be seen in Fig. 2.1 [89]:

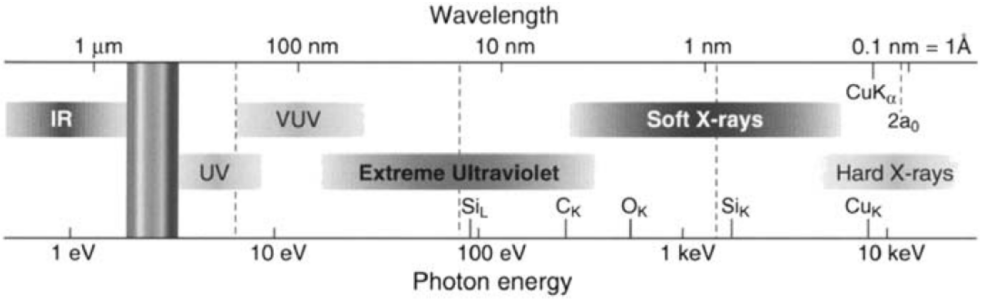


Figure 2.1. Schematization of the photon wavelength spectrum [89].

Indeed, when the device dimensions and the required spatial resolution are of the order of a micron, photolithography is performed with the visible light; when instead the device dimensions start to be shrunk, also the wavelength of light sources has to become smaller, up to the X-ray lithography working at a wavelength of ~ 1 nm.

In the following subsections, the basic principles of optical lithography will be presented, together with its limits and the possible solutions to overcome them.

2.1.1.1 Optical lithography working principles

The first photolithographic processes were performed with contact or proximity optical lithography [90], where the mask is in direct contact with (or separated by a little gap from) the photoresist, so that the pattern on the mask is replicated onto the resist with a 1:1 ratio. Contact lithography, however, is subjected to contamination and mask damage due to its contact with the photoresist, while for proximity lithography there are some diffraction effects that will limit the resolution and the

accuracy of the pattern transfer. For these reasons, both contact and proximity optical lithography were soon substituted by projection optical lithography, where the mask is placed at a certain distance from the substrate, allowing to project a de-magnified image onto the photoresist with a 5:1 or 10:1 ratio. A schematization of these concepts is shown in Fig. 2.2 [91].

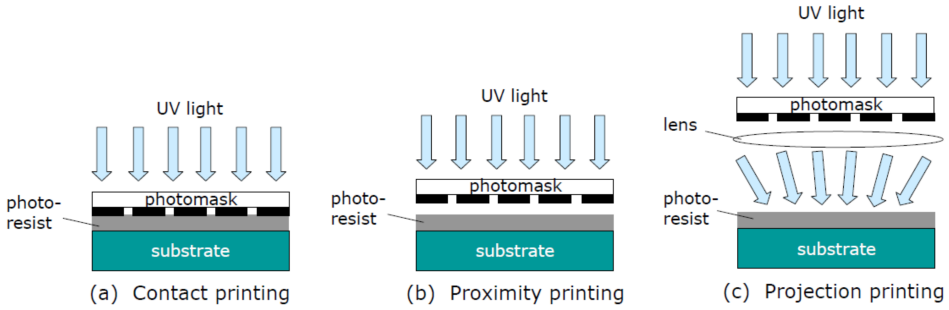


Figure 2.2. Schematization of: a) contact lithography; b) proximity lithography; c) projection optical lithography [91].

The mask features can be treated as slits where the light is diffracted according to Young's principle of interference. These diffracted waves interfere each other causing minimum and maximum of the transmitted light intensity according to the following relation:

$$sin\,\varphi = m \cdot \frac{\lambda}{a} \tag{2.1}$$

where m=1,2,3..., φ is the diffraction angle, λ is the wavelength of light and a is the slit width.

As it is clear from Eq. 2.1, smaller slits cause a larger spread of light, while waves with shorter wavelength have narrower distribution of the diffracted beam. Because of the spread of light due to the slit width, if two slits are too much close together, the resulting images can merge making them irresolvable. In addition, light coming out from a mask opening must be focused onto the substrate through a lens system, whose diameter determines how much diffracted light will pass through the lens. The range of angles allowed to enter this system are quantified by the numerical aperture (NA) of the lens, defined as:

$$NA = n \cdot sin\,\theta \tag{2.2}$$

where n is the refractive index (RI) of the medium between the lens and the imaging plane, while θ is the half-angle of the maximum cone of light entering or exiting the lens. Considering this kind of optical projection system, its resolution limit can be defined according to Rayleigh's criterion, which determines the minimum resolvable details of an imaging system [92]:

$$R = k_1 \cdot \frac{\lambda}{NA} \tag{2.3}$$

where k_1 is a factor (smaller than unit) depending from the specific imaging process.

It is therefore clear that, at fixed NA, shorter wavelengths produce lower light diffraction, while, at fixed wavelength, bigger NA admits more diffracted light on the substrate resulting in more details of the mask feature and, therefore, higher resolution.

Another important parameter to consider is the depth of focus (DOF), that can be considered as the distance over which the plane image can be placed in order to have a focus imaging [93]. It can be defined as:

$$DOF = k_2 \cdot \frac{\lambda}{NA^2} \tag{2.4}$$

By comparing Eq. 2.3 and Eq. 2.4 it is possible to note that a large NA provides better resolution capabilities, but very small DOF. For this reason, even if sophisticated mask illumination techniques can be used, reducing the exposure wavelengths is still the main method to improve optical lithography technique.

2.1.1.2 Deep UV lithography

In the early stage of optical lithography, mercury lamps emitting at 436 nm (G-line) and 365 nm (I-line) were the first used light sources for optical lithography. Since these lamps are appropriate for minimum features size down to 0.25 µm [94], when the demand for smaller features size raised, mercury lamps were substituted by excimer lasers, which can provide higher photon energies and shorter emission wavelengths. These sources are pulsed gas discharge lasers with light output in ultraviolet (UV) region of the spectrum. With the introduction of this kind of sources, the deep UV (DUV) optical lithography begun with a krypton fluoride (KrF) laser source emitting at 248 nm; this source has been soon followed by an argon fluoride (ArF) excimer laser whose emitting wavelength is 193 nm. The 193-nm wavelength lithography gives excellent results especially in immersion lithography technique, where the standard lithographic resolution is highly enhanced by substituting the air gap between the final lens and the substrate with a liquid with higher refractive index [95], as it is schematically shown in Fig. 2.3 [96].

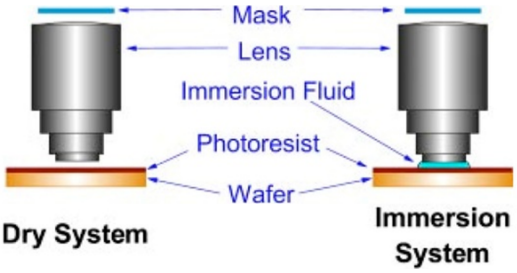


Figure 2.3. Comparison between dry (on the left) and immersion (on the right) project optical lithography [96].

With immersion nanolithography and highly purified water as immersion fluid, the minimum achievable feature size is 35 nm [97], but several mask-source optimization have been performed and are the objective of several researches to extend the immersion lithography technique below the 20 nm node [98].

In addition, optical lithography has considered also molecular fluorine (F_2) excimer lasers emitting at 157 nm and Ar_2 excimer lasers emitting at 126 nm, which allow to perform lithography down to the 32 nm node. However, at these wavelengths, the quartz masks are no more transparent; they have therefore been substituted by calcium fluorine (CaF_2) masks. However, CaF_2 is a crystalline material, which creates a birefringence effect that, in turn, causes a different refraction for the two polarization components and the accumulation of a different phase for these components. This affects the maximum achievable resolution due to the blurring of the image caused by these effects; for this reason, the growth of CaF_2 crystal must be as isotropic as possible in order to reduce the birefringence as low as possible, which is a considerable issue to be considered. Moreover, the high absorption taking place at 157 nm hampers the use of the pellicles typically used to prevent the photomasks contamination and hence the distortion of the image realized into the photoresists. These ones, in addition, are too absorptive at 157 nm, therefore new resist materials should be developed. For these reasons, together with the development of the immersion lithography described above, 157-nm lithography became no more competitive and the following step in optical lithography jumped directly to 13-nm lithography, with the extreme UV (EUV) lithography process.

2.1.1.3 Extreme UV lithography

Extreme UV lithography (EUV) at 13-nm can be considered no more an optical lithography, but rather a soft X-ray lithography. In Fig. 2.4 [88] a schematization of a EUV lithography system is shown.

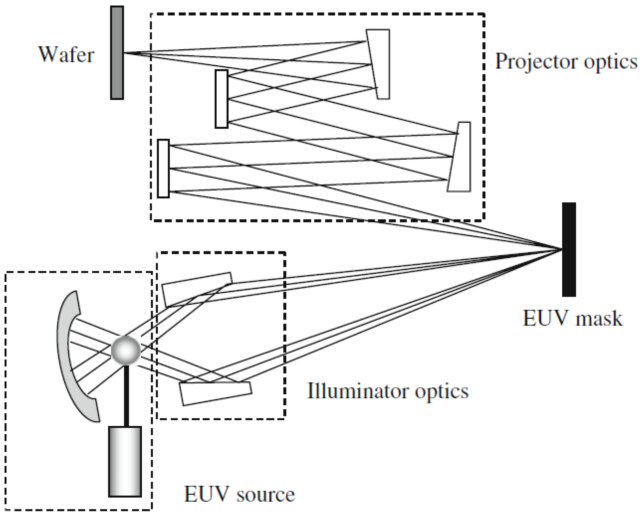


Figure 2.4. Schematization of a EUV lithography system [88].

It consists of a EUV source (typically based on plasma-generated radiation) which irradiates a reflective mask through a couple of mirrors (acting as a condenser) and of a projecting system (constituted by a mirror system that provide constructive interference toward the reflected projections) that focus the reflected radiation onto the substrate. For some aspects, it is quite similar to a projection optical lithography; however, there is a fundamental difference due to the strong absorption occurring in

every material at this wavelength, which makes the classic refractive optic's laws no longer valid. The key component of such system is indeed the projection optics, constituted by a multilayer reflective mirror. Since the reflectivity of any material at this wavelength is quite low, the mirror surface must be coated with many alternating layers with dissimilar optical constant constituting a distributed Bragg reflector, whose reflectivity has a resonance value when the alternating layer period is $\sim \lambda/2$. The most employed multilayer mirror is constituted by molybdenum and silicon layers [99], since they have the highest reflectivity at ~ 13 nm, even if this reflectivity can be lowered by the presence of impurities in the deposited layers or scattering due to the layers surface roughness. For the same reason, also the reflecting mask must be as flat as possible in order to avoid phase errors (due to bumps or hole into the substrate) or amplitude errors (due to flaws of the multilayer). Due to the lower power offered by EUV sources respect to DUV ones, the use of chemically amplified (CA) resists is required in order to enhance the throughput of this lithographic technique. Moreover, the EUV lithography shows a very high line edge roughness, which is defined as the variation of the width of a resist feature occurring along its length [100]; anyway, these issues can be overcome with the improvement of the resist properties, that allowed the EUV lithography to achieve sub 14 nm pitch resolution [101]. On the contrary, the outgassing of resist during EUV lithography process remains a serious trouble, since it degrades the optics reducing their lifetime. This aspect, together with the high-cost equipment required for EUV systems, makes this lithographic technique not competitive with immersion lithography.

2.1.2 X-ray lithography

For the X-ray lithography, the radiation wavelength lies into the range from 0.1 nm to 1 nm. X-rays can penetrate almost any material, except those having a high atomic number. Moreover, X-ray cannot be focused because the refractive index of any material at sub-nanometric wavelengths is almost equal to 1, therefore there will always be a 1:1 image produced by this lithography technique. In Fig. 2.5 [88], a schematization of an X-ray lithography system is shown.

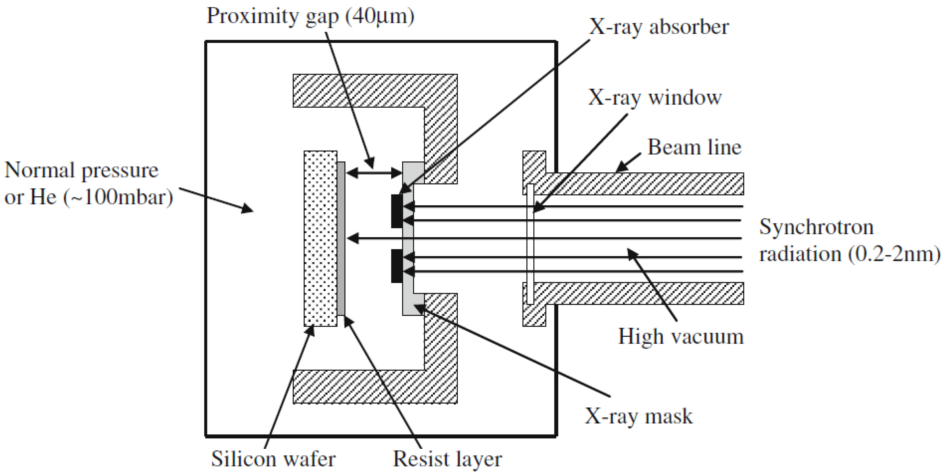


Figure 2.5. Schematization of an X-ray lithography system [88].

The X-ray mask is constituted by a membrane (whose thickness is about 1-2 µm) of low-atomic number materials, that allows the X-ray to pass, with a high-atomic number materials pattern that act as absorber for the X-rays. The gap between the mask and the substrate, of the order of 5-50 µm [102], is required due to the fragility of the thin membrane of the mask, which can't be placed in contact with the exposure surface.

Despite the promising application of X-ray lithography, it never replaced classical optical lithography due to the high difficulties in the mask fabrication, since the 1:1 pattern transfer ratio requires the absorber feature sizes to be equal to the resist ones. Moreover, a very accurate control of the mask-substrate gap is required, because variation of this gap will cause variation in the resolution. Finally, it is quite difficult to reach sub-50 nm resolution due to the Auger electrons generated into the resist after X-ray irradiation and due to X-ray diffraction. Indeed, the Auger electrons generated by high-energy X-rays will acquire energy and travel within the resist layer, causing the expansion of the exposure pattern and hence a reduction in resolution capabilities. The diffraction effects can be reduced by reducing the gap between the mask and the substrate, but the gap cannot be lower than 5 µm, with a best resolution achieved of $\sim$ 30 nm [92]. For these reasons, together with the high-cost equipment, X-ray lithography has never replaced the classical optical approach.

2.1.3 Charged beam lithography

Nanofabrication techniques employing charged beams are for some aspects similar to optical ones: here, indeed, electrons or ions release their energy into an energy-sensitive material to perform structuring or to remove material, with the further advantage that charged beams can be focused in extremely small spots thanks to sophisticated lens systems.

Charged beam lithography can be divided essentially in two different types: electron-beam lithography (EBL) and focused ion beam (FIB) lithography. Electron beam lithography evolved from scanning electron microscope (SEM) thanks to the discovery of an electron-sensitive polymer, the polymethylmethacrylate (PMMA), whose exposure is very similar to the exposure of a photoresist by photons. Thanks to PMMA, patterning of structures with feature size below 60 nm was possible already in the early 1970s [103]. Nowadays, thanks to EBL processes, it is possible to achieve resolution lower than 10 nm [104].

Ions, instead, differ from electrons due to their heavy mass, which make them suitable for nanofabrication by a direct structuring of the material, rather than by the exposure of a polymer resist. Ion beam lithography was not performed until the introduction of liquid metal ion sources due to the difficulty to achieve fine ion beam spots, that now can be focused up to 5 nm. This very fine beam size allows to remove material directly from a surface and also to deposit material, with the assistance of proper gases.

The fundamental problem of charged beam lithography relies into the low throughput caused by its serial scanning mode of operation. Anyway, a proper choice of the exposure parameters, especially in case of EBL, can optimize the working times making it the most widely employed lithographic technique in micro- and nanofabri-

cation thanks to its high resolution and high reliability in fabrication processes and pattern replications.

In the following subsections, a more detailed analysis of FIB and EBL systems will be presented, with a particular attention to the EBL system used for the development of the devices proposed during this work thesis.

2.1.3.1 Focused Ion Beam lithography

FIB lithography is a very powerful tool for nanofabrication, since it allows not only to create patterns in a resist [105], but also to locally mill atoms from a surface [106] or to deposit material on it [107] with sub-10 nm resolution, to locally implant ions [108] and direct material modifications [109]. Moreover, due to the high energy of the ions, a faster exposure of the resist is required and, therefore, lower process times. Anyway, the principal advantage of FIB lithography is the possibility to perform very high resolution lithography without a resist: indeed, resists cannot be applied on non-planar substrates and, where a resist layer can be deposited, it is possible to perform high resolution lithography only on homogeneous resist layers whose thickness is lower than 100 nm. Therefore, the possibility to perform patterning without a resist layer is an attractive perspective in order to further enhance resolution capabilities. In the following subsections, the basic principles of ion-solid interaction will be presented, together with the description of a typical FIB equipment and its lithographic capabilities.

2.1.3.2 Ion-solid interactions

Ion interactions with matter can be divided into elastic/inelastic scattering collisions (during which an energy transfer occur between the impinging ions and the substrate atoms) and in electronic interactions.

The elastic collisions between the impinging ions and the atoms of the substrate (or the resist) causes the broadening of the beam due to scattering events, the amorphization of the target sample and the physical sputtering of the substrate atoms, if the momentum transfer between the impinging atoms and the surface atoms overcomes the surface binding energy. In addition, the ions impinging on the substrate cause an atomic mixing which, together with the amorphization of the substrate, may cause the intermixing of resist and the substrate atoms and also the implantation of the primary ions.

On the other hand, inelastic collisions involve an energy transfer either to the electrons than to other atoms of the substrate. Almost all of the impinging energy is transformed into kinetic energy of the secondary electrons, whose energy corresponds to the energy required for the breaking of molecular bonds (1-50 eV) and that is responsible of the resist exposure.

These interactions are responsible of the patterning performed by a FIB system, whose typical equipment is descripted in the following subsections together with the possible lithographic processes that can be performed with this system, that are schematically shown in Fig. 2.6 [110].

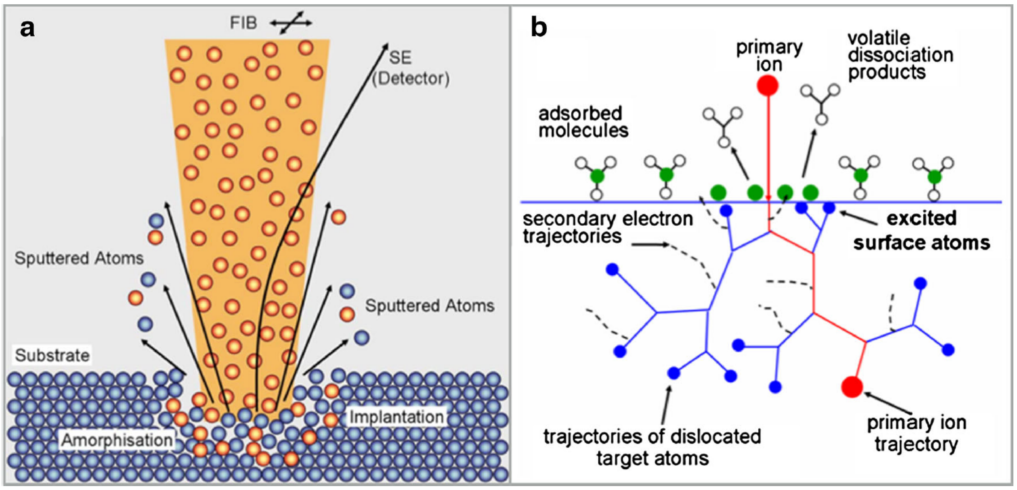


Figure 2.6. Schematization of ions-solid interactions [110].

2.1.3.3 FIB equipment

In order to perform lithography with a FIB system, a point source is needed to produce a very focused beam. Indeed, several ion sources existed well below the development of FIB systems; in particular, electron bombardment ion sources were successfully employed in mass spectroscopy but provide too low ion current to be used for ion lithography [111]. Gas discharge ion sources, instead, can produce higher ion currents, but are not point-sources, therefore they are not suitable as FIB sources. Only with the advent of the liquid metal ion sources (LMIS) FIB became really feasible for lithography applications [112]. These sources operate by desorption of atoms from a source metal tip that has been heated up to the liquid state; a Taylor cone (shown in Fig. 2.7 [113]) is formed under a strong applied electric field, which get this cone to be much sharper until ions are produced by field evaporation.

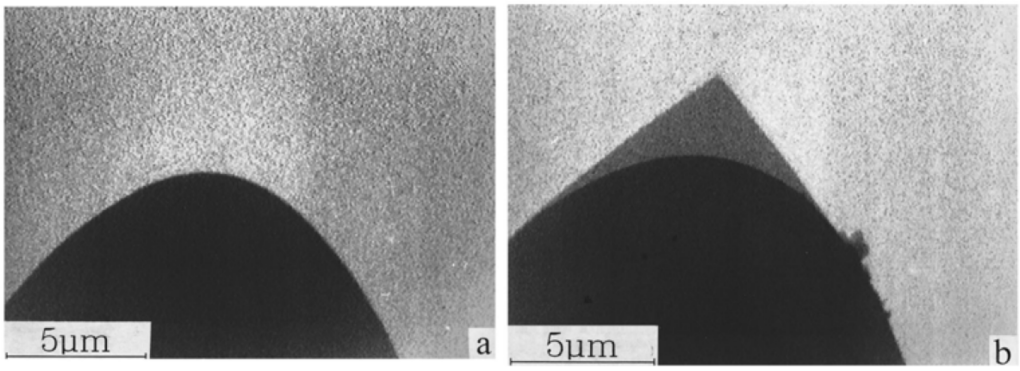


Figure 2.7. Shape of the LMIS emitter tip a) without the Taylor cone and b) with the Taylor cone [113].

These sources allowed to focus an ion beam to a spot size dimension up to 5 nm.

Nowadays, FIB systems using liquid sources for gallium (Ga) ions are the state-of-art tools, with a tungsten (W) wire forming the sharp tip induced by an electric field exceeding a threshold value of 20 kV [109]. However, the heavy Ga^+ ions may cause a substrate damage due to an induced Ga^+ ions implantation or the substrate atoms displacement. For this reason, a helium (He) ion source may constitute a good alternative. He^+ ions are indeed lighter than Ga^+ ones, but three times heavier than electrons, allowing sub-35 nm lithography with commercial FIB systems [107].

Another interesting ion source is constituted by neon (Ne) ions, that offer high brightness source technology [114], but that must be further developed to achieve better resolutions, especially in milling field, where heavier ion species are required.

2.1.3.4 Resist-based FIB lithography

The pattern definition of a resist through FIB is performed by a variation of the solubility properties of a resist after the ion irradiation. The resist material behavior, however, depends on the deposited energy: ions with a low mass to energy ratio will deposit their energy through electronic effects mainly, while ions with high mass to energy ratio will deposit their energy through nuclear stopping [115].

For electronic energy deposition, the energy dissipated into the resist layer will damage the bonds between its polymeric chains causing a variation in its solubility. For nuclear stopping deposition, instead, the resist behavior will change completely: it has been shown that, for low energy Ga^+ ions, positive resists act as a negative resist when irradiated with a high flux ion beam due to the crosslinking of the radicals liberated by the impinging ions [115]. Moreover, at sufficiently high ion doses, the ion implantation can be employed to perform positive and negative patterning in one exposure step by just varying ion energy, since a sufficiently high ion implantation into the resist can avoid its development/etching [116].

Unfortunately, during ion bombardment, part of the impinging ions can be implanted into the substrate, and this is an issue where the substrate is sensitive to such doping. However, this issue can be easily overcome by introducing an absorbing layer between the resist and the substrate.

2.1.3.5 FIB patterning by ion implantation

The ion implantation into the substrate occurring during the exposure can be employed to perform 3D nanopatterning: indeed, if the depth at which the ions stop their penetration into the substrate (depending from the applied ion dose) is sufficiently fine and the number of ions is sufficiently high, a thin layer of a doped material is formed, with a local variation of its chemical properties. If this implantation is selectively performed and then is followed by an etching process like reactive ion etching (described in Section 2.3.2), this process results to be a suitable way to perform 3D lithography, since the performed implantation can acts as an etching mask, as it can be seen in Fig. 2.8 [109].

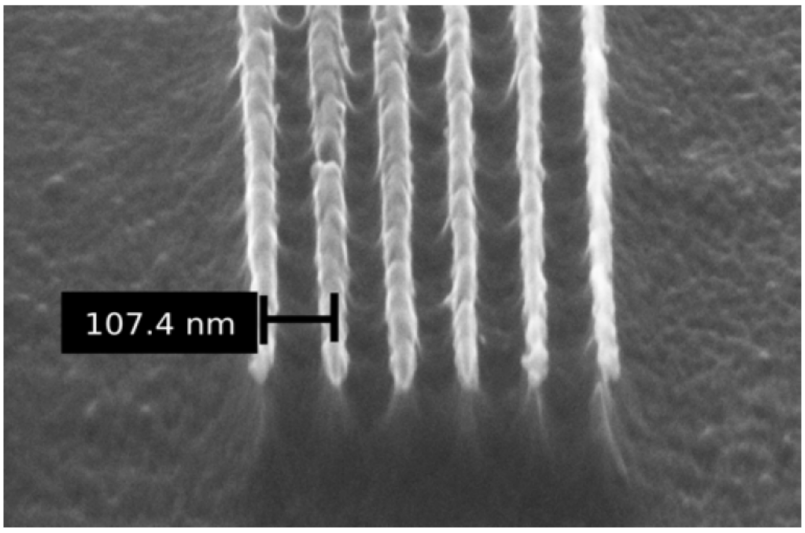


Figure 2.8. SEM image of an implanted and etched line space pattern with 50 nm half-pitch [109].

2.1.3.6 FIB milling and gas-assisted processing

Among the possible applications of FIB lithography, the most prominent are the FIB milling and the gas-assisted processing. These processes are possible due to the elastic scattering events that occur during ion bombardment. As said before, due to these scattering events an energy transfer from the ion to the target atoms occurs, which, in turn, causes the displacement of the target atoms. This displacement starts a cascade process where the kinetic energy is transferred between neighbor atoms by further elastic scattering processes. When this avalanche process reaches the target substrate surface, some of the surface atoms can reach enough energy to leave the surface and enter the surrounding vacuum, where they can be re-deposited or pumped away by the chamber pumps system. When this last process occurs, there is a material removal from the surface called *milling*. The number of the removed atoms depends on the target material, the ion species, their energy and the incidence angle. This process is usually employed for the sample preparation for transmission electron microscope (TEM) [117], but, due to the high ion dose required, only small areas patterning is usually performed in order to have reasonable processing times.

The energy transfer from the impinging ions may occur also to molecules adsorbed on target surface by some precursor gas introduced into the chamber, causing a chemical reaction like the decomposition of the adsorbed molecules and their reaction with the target atoms. By a proper choose of such adsorbed substances it is possible to induce a local deposition of specific materials, in a process called *gas-assisted deposition* (GAD), which can be used, as example, to correct the defects present on photomask [118]. Moreover, the energy transfer to the target surface may cause also a reaction of the gas precursors with the target material atoms. If the resulting product is volatile, this process causes a local etching of the target, in a process called *gas-assisted etching* (GAE), usually employed in selective etching of material in photomask repair [119].

For these reasons, FIB lithography is mainly used for a direct transfer of the pattern onto the substrate without using a resist, while, when a patterning of the resist is required, together with ultrahigh resolution capabilities, the EBL lithography is preferred.

2.1.3.7 Electron beam lithography

Electron Beam Lithography (EBL) is a well-established high-resolution patterning technique. EBL technology consists of the irradiation of a surface covered with an electron-sensitive polymer (the electroresist) with a focused electron beam. This beam carries energy, which will be released into the resist layer to perform structuring by its selective exposure. This technology uses a direct writing system, which does not require the use of physical masks because the pattern generated from a Computer-Aided Design (CAD) is directly transferred into the resist layer through the deflection of an electron beam, avoiding the diffraction effects typical of conventional photolithography [120]. In the following subsections, the basic principles of EBL will be presented, together with the required resist material and the equipment employed for the devices developed during this work thesis.

2.1.3.8 EBL working principles

To have a nanoscale lithography with an electron beam, the particles have to interact with a polymer electroresist, whose chemical properties will vary after the energy transfer from the electrons to the substrate material due to the scattering phenomena. In particular, two different kind of scattering events may occur: elastic and inelastic scatter, that are schematically shown in Fig. 2.9 [121].

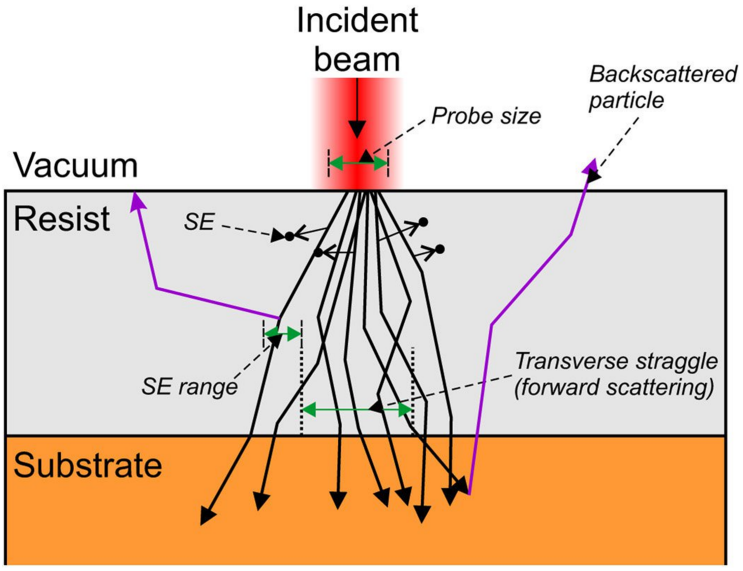


Figure 2.9. Schematization of the scattering events occurring when an electron beam impinges on a substrate [121].

When the electron beam enters the resist, a large number of inelastic events occurs (generating a phenomenon called *forward scattering*), during which the impinging electrons release their energy to the electrons of the resist without varying their direction, except for small angle deviations. In a positive tone resist, the exposure to an electron beam causes a scission of the polymeric chains of resist, making it soluble when it is immersed into the developing solution; on the other hand, in a negative resist, the exposure to an electron beam causes a crosslinking of the polymeric chains, which makes the resist insoluble into its developer. In addition to inelastic scattering events, also elastic collisions between the impinging electron beam and the resist/substrate atoms occur, generating a phenomenon called *backscattering*. In this case, the electrons change their direction at large angle without losing their energy; for this reason, the electron may return back into the resist layer causing an unwanted exposure. Due to the scattering events described so far, the adsorbed dose (the amount of energy deposited per unit area) is not confined to the zone whereby the electron beam has been driven. This results in the so-called *proximity effect*, which may cause dimensional distortion and design mismatch into the final pattern [122].

There are three principal reasons that can strongly influence the electron scattering:

1. *Beam energy*: higher energy of the primary electrons will cause smaller scattering angles, leading in turn to a small broadening of the impinging beam.

2. *Density of substrate material*: there will be a higher backscattering from the substrate if the substrate material is of higher density. This, in turn, will limit the resolution capabilities of e-beam lithography on high-density substrate.

3. Resist thickness: electrons scatter widely when they go deeper; therefore, for a high-resolution patterning, a thinner resist is preferred.

These factors must be taken carefully into account when considering the patterning of an electroresist. Indeed, because the deposited energy can extend to adjacent areas, dense patterns will undergo to overexposure effects, while an isolated pattern will undergo to underexposure effects, generating the so-called intershape and intrashape proximity effect, respectively. Therefore, proximity effect corrections are necessary, especially for dense pattern lithography. A proper choice of the exposure parameters can minimize such effects, for example by using thin resist layer or choosing appropriate beam energies. Moreover, it is possible to properly correct proximity effects; in particular, two methods are mainly used for this purpose:

- *Dose correction.* This correction method, often referred to as a physic-based correction method, is the most widely used correction technique. Its working principle consists in the adjustment of the exposure dose at different parts of the pattern in such a way that all the pattern receives the same energy. In Fig. 2.10 an example of this correction technique is shown. The isolated pattern elements will receive a higher exposure dose (represented as red dots into Fig. 2.10), while the highly dense pattern elements will receive a lighter exposure dose (represented as light green dots). As it can be seen from the

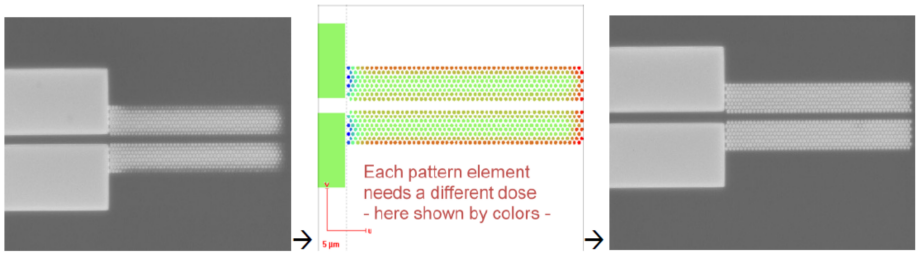


Figure 2.10. Dose correction for proximity effect.

comparison between left-side and right-side of Fig. 2.10, with the proposed dose correction all the elements of the pattern can be resolved. For very complicated pattern designs, it is possible to carry out intense reiterative computations which will redistribute dose energies of different parts of the pattern in order to improve the uniformity of the energy distribution. However, due to the high computational cost required from this optimization method, it is often carried out only on the pattern zone where the scattering effect is significant.

- *Pattern biasing.* Differently from the correction method described so far, the pattern biasing method is a faster (but relatively coarser) proximity correction technique based on the resizing of the geometrical features of the pattern elements. This method is particularly suited for simple and highly repeated patterns; it consists in a reduction of the element dimensions (negative biasing) in dense geometries in order to compensate the higher energy contribution from neighbor elements, or in an increase of the element dimensions (positive biasing) to compensate the lower energy contribution given from scattering effects. Moreover, it is possible to add further elements in underexposed areas for the same reason. An example of this correction method is shown in Fig. 2.11.

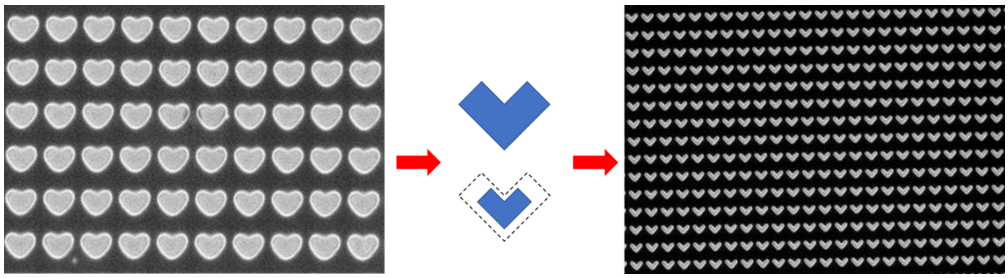


Figure 2.11. Negative pattern biasing correction.

Although the greatest contribution to the proximity effect comes from the scattering of the primary electrons, the secondary electrons have the fundamental role in resist exposure. Indeed, secondary electrons are electrons removed from the atoms of the substrate material by high-energy primary electrons. While traveling through the resist, primary electrons collide with the electrons of the surrounding material, transferring their energy and generating secondary electrons with an

acquired energy up to keV. These secondary electrons become mobile and can travel for short distances, scattering at the same way of primary electrons and leaving their energy along the path of scattering. These low energy electrons are the true responsible of resist exposure, because they leave almost all of their energy into the resist layer; moreover, the majority of the polymer chain-scission or cross-linking events occurs during the interaction with electrons of below 100-eV energy.

2.1.3.9 Low-energy EBL

Although, as mentioned before, a high-energy e-beam lithography is favored for high-resolution lithography since it results in narrower forward scattering and lower backscattering [123], its principal drawbacks, due to the inefficient use of energy and requirement of high exposure dose, have led to the development of low-energy lithography [124]. Indeed, at high beam energy, there will be more electrons penetrating the substrate rather than those contributing to the resist exposure, requiring higher exposure dose in an inefficient manner. Moreover, at high energies two problems can arise: the heating of the substrate and its charging. The latter problem can be resolved, especially for non-conductive substrates, by using a thin metal layer between the substrate and the resist layer [125]. The substrate heating causes, especially in substrates with poor thermal conductivity, a change in resist sensitivity and serious proximity effects, but this problem can't be overcome. Low-energy lithography offers several advantages: first of all, it is helpful in defining the vertical profile of the exposed resist. Indeed, the lower is the beam energy, the higher will be the undercut of the exposed resist profile, as it can be seen from Monte Carlo simulation of electron trajectories performed at low and high beam energy shown in Fig. 2.12 [88].

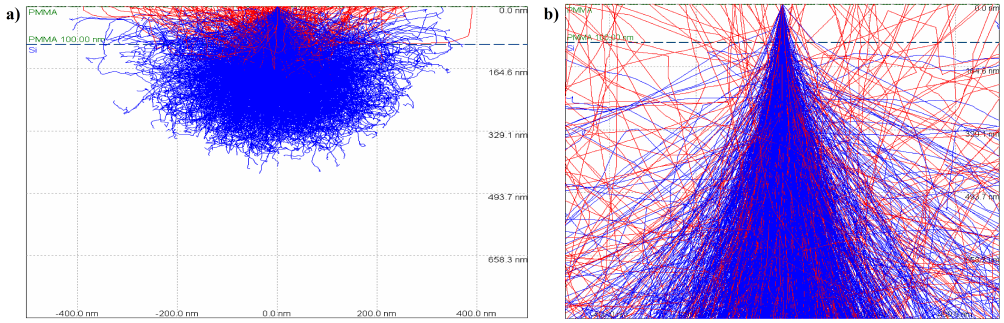


Figure 2.12. Monte Carlo simulation of the electron trajectories at a) 5 keV and b) 30 keV [88].

This effect must be avoided when a vertical resist profile is needed; on the other hand, a non-vertical profile can be helpful if it must act as a shadow mask for the pattern transfer process subsequent to resist exposure, especially for the lift-off process, which will be better explained in Chapter 3.

In addition, at low energy there will be an increase of the resist sensitivity (defined as the exposure dose at which the resist has been fully developed) due to the lower range of the forward scattered electrons. This effect causes a higher concentration of energy deposition in the resist layer instead of the underlying substrate, which, in

turn, allows the resist exposure with a lower number of electrons. On the other hand, one of the main drawbacks of the low-energy lithography relies in the difficulty to obtain a fine beam size, owing to the severe chromatic aberration and space charge effects that arise at low energy due to the energy spread of electrons [88].

All of these aspects have to be taken carefully into account when defining the exposure parameters for a lithographic process; every choice will be the result of several considerations and trade-offs in order to obtain the best exposure parameter set for the fulfillment of the project specifications.

2.1.3.10 EBL column

To realize a high-resolution patterning, the electron beam size must be as smaller as possible. This is possible thanks to a complex SEM column, schematically shown in Fig. 2.13 [104].

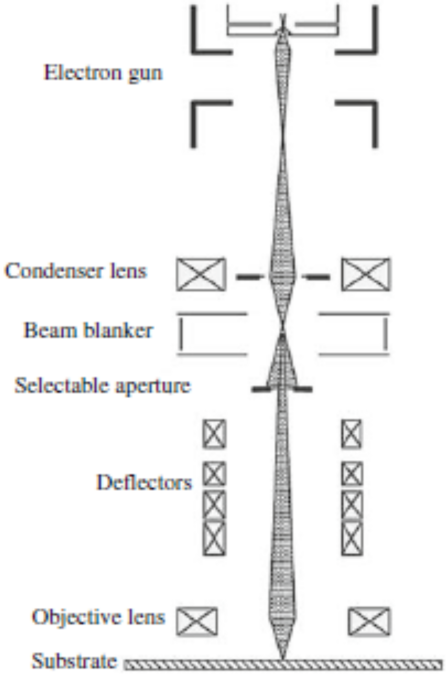


Figure 2.13. Schematization of a typical SEM column [104].

The electron gun, constituted by the source and the lenses for the focusing of the beam, is on the top of the column, and it is followed by a condenser which further focuses the beam. The beam blanker allows the beam to be turned on/off, while the apertures allow different quantity of electrons to enter the final lens system. Finally, the deflectors will scan the beam into the horizontal plane to perform the required lithography on the substrate.

To obtain a very small beam size, the electron source has to be small. Before the advent of field emission (FE) electron sources, the typical sources were constituted by tungsten or lanthanum hexaboride (LaB_6) compounds thermal cathodes, that have as a high drawback their large emission area. To reduce the source size, it is possible

to use a strong lens in front of the cathode which will focus the emitted electrons into a small cross-over, acting as a virtual source for the downstream lens system. However, the cross-over size is limited by the Coulomb repulsion arising from the high electron concentration at the cross-over. With the field emission (FE) sources these issues have been overcome, because the electron emission occurs directly from the material surface by a very high electrical field (higher than 10^8 V/m). A FE source is a fine needle with a sharp end where a high electrical field is generated with low voltage. The electrons are emitted only at the points where the electric field exceeds the threshold voltage, leading to an emission area controlled and small.

Regarding the lens systems, both electrostatic than magnetic lenses are used in a typical Gemini SEM column, schematically shown in Fig. 2.14 [126].

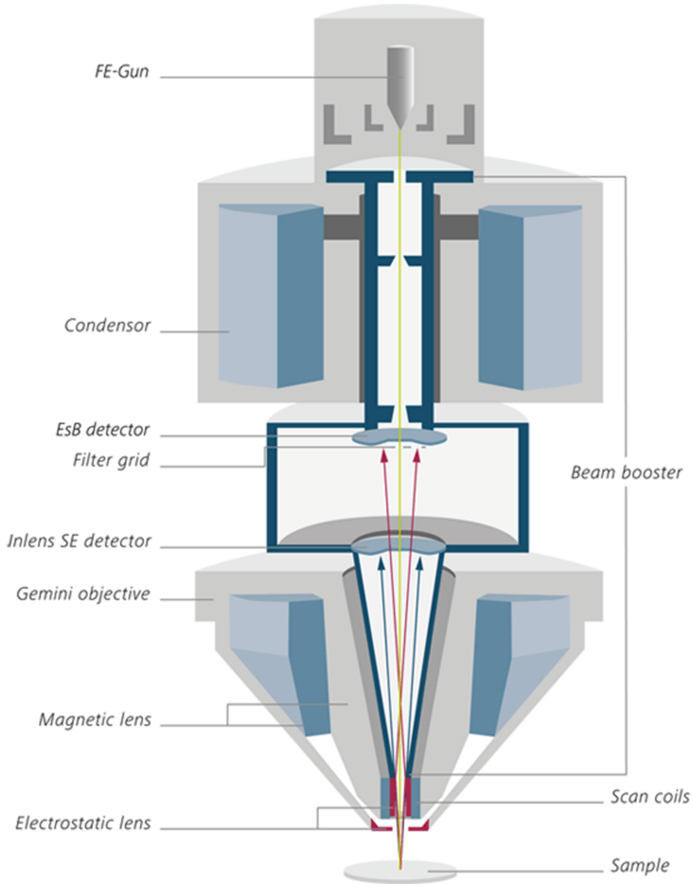


Figure 2.14. Schematization of the magnetic and electrostatic lenses used to focus and accelerate electrons [126].

Electrostatic lenses force an electron to converge in a point of the optical axes; this is accomplished by three plates provided with a central aperture, where the central plate has a variable potential applied on it, while the first and the third plate are connected to the ground. The focusing power of an electrostatic lens is limited because it depends on the voltage applied to the lens and in the gap between two lenses, which must be as narrower as possible. This, in turn, could cause an electrical breakdown if the applied voltage is too high. For this reason, electrostatic

lenses are usually used into an EBL system to accelerate the electrons, while the focusing operation is carried out by the magnetic lenses, which can generate high magnetic fields by high currents passing through coils. These high currents will produce great heat, which can be cooled by a forced circulation of water supplied by an external chiller.

Every EBL system is equipped with a series of different sized apertures, that prevent the wide-angle electron to enter the objective lens, which focuses the beam coming out from the selected aperture onto the substrate. One of them must be selected depending on the beam current and resolution requirements: bigger apertures lead to higher beam currents but lower resolution capabilities; for this reason, to obtain high resolution lithography, the smallest aperture should be selected.

A detailed description of the system employed for the development of the proposed devices will be presented in the following subsection.

2.1.3.11 EBL equipment

The Nanofabrication laboratory at Institute for Microelectronics and Microsystem (IMM – CNR Unit of Naples), where the nanofabrication of the proposed devices has been carried out, is equipped with a Raith 150 system (shown in Fig. 2.15) located into a Clean Room (Class 1000) at 24 °C temperature.

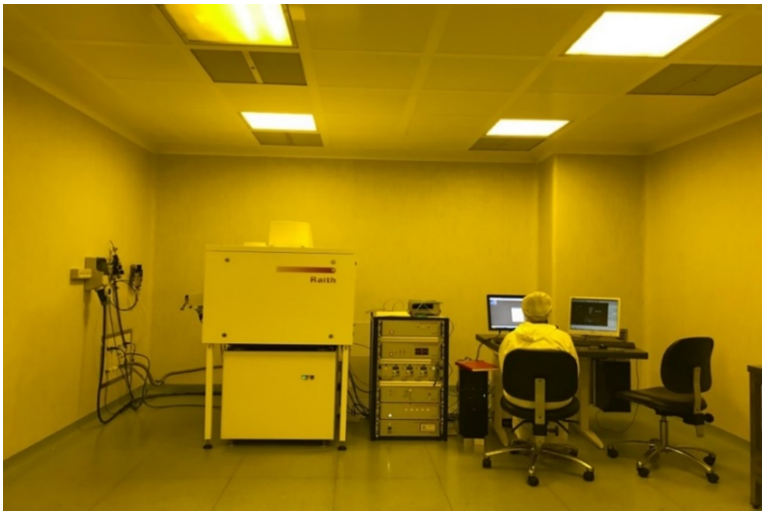


Figure 2.15. EBL Raith 150 system.

This system is based on a Schottky thermal field emitter ZrO/W filament, a beam energy ranging from 0.2 to 30 keV, and a beam current ranging from 5 pA to 5 nA. There are six apertures available, whose diameters are 7.5, 10, 20, 30, 60 and 120 µm, and two detectors for secondary scattered electrons: InLens and SE2, in lateral position. The produced beam is a Gaussian type which is steered in XY plane with a fast vector scan technique. Differently from the raster scan technique, where the beam is driven all over the working area and the shape is controlled by switching on and off the beam, the vector scan mode is more time efficient, because the beam is only scanned into the areas that should be patterned. A schematization of such scanning techniques is shown in Fig. 2.16.

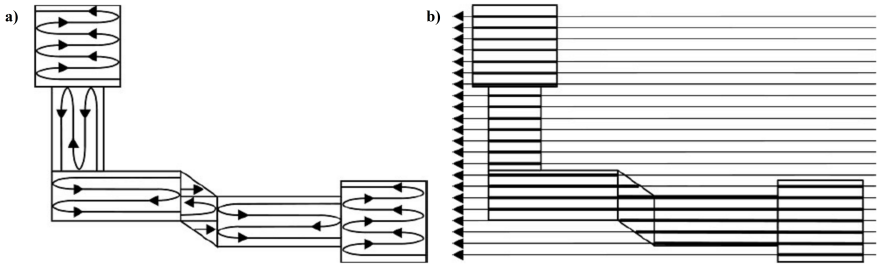


Figure 2.16. Schematization of a) vector scan mode and b) raster scan mode.

In particular, the pattern design is fragmented into sub-elements that will be continuously exposed by a beam of Gaussian intensity profile. At the end of the sub-element exposure, the beam is switched off and it is directly driven to the next position. This technique is implemented by using two Digital-to-Analog converters (DAC): the first is used to conduct the deflectors into the corner of the element to expose, while the second drives the beam within the element. If the area of the design is bigger than the write field (that is the largest area exposed without moving the stage; the typical write field area used within this thesis is 100 µm x 100 µm), another fragmentation must be done; moreover, careful alignment procedures have to be performed in order to prevent the stitching between adjacent write fields. For these reasons, the system has been equipped by a motorized support and positioning supplied by an interferometric stage that optimize the stitching precision. Moreover, the support is isolated from mechanical vibrations, which would dramatically affect the beam resolution. In addition to this, it is very important to work in high vacuum conditions inside the column, because the beam performances and resolution are strongly conditioned by the vacuum conditions. Since the high vacuum level required for this system (lower than 10^{-9} Torr inside the column, 10^{-6} Torr inside the chamber), the column includes a valve that can isolate it when the sample must be load/unload inside the chamber. During these operations a turbomolecular pump vents a load lock until its vacuum level is equal to the chamber vacuum level; only when this condition is met the valve opens and a robot arm can enter the chamber and carry the sample holder in/out the whole system. A picture of the load lock and the sample holder is shown in Fig. 2.17.

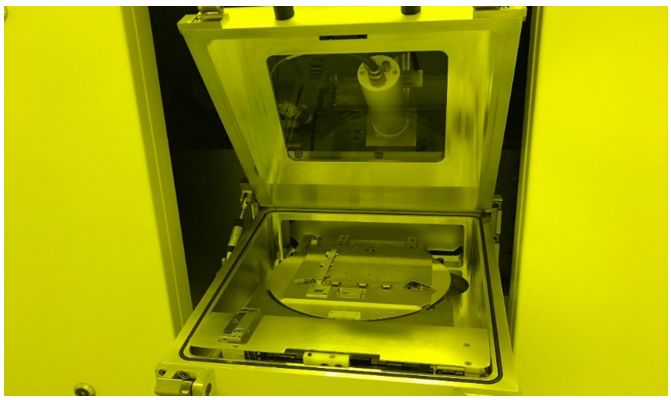


Figure 2.17. Load lock and sample holder of the EBL Raith 150 system.

Two computers provide the control of the SEM column and of the Raith writing system since the operation of direct write relies on the release of a proper dose to the electron-sensitive resist according to the desired design. The Raith processor determines the order, geometry and size of irradiation accordingly to the fragmentation of the pattern. As a consequence, this computer is responsible of design, exposure rhythm (the beam deflection speed), stage positioning and adjustment of the exposure fields (alignment and size). The design file can be developed through its graphical CAD software, where basic structures can be easily drawn (such rectangles, circles, polygons, etc.) and organized in several layers for multilevel exposures. In addition, several mathematic functions allow a reorganization of such basic structures in order to obtain more complex designs. This CAD files are compatible with GDSII, DFX, CIF and ASCII formats, allowing therefore the importation of external files, which will be anyway converted to the internal GDSII that include the information about exposure parameters, some of which are calculated directly from Raith software. The lithography is performed by scanning the desired pattern, write field by write field, with an electron beam of circular section; through the user-determined step size value (the distance between two adjacent beam spots, which depends on the pattern minimum feature size since it must be lower than 1/5 of the smallest design feature) and the exposure dose (the amount of energy that the resist must receive, that depends on resist characteristics and pattern density too), the beam speed can be determined. During irradiation, the dose is adjusted by calculating the beam dwell time (the time that the beam remains in each pixel), which is automatically calculated once the area dose, the step size and the beam current are known, which in turn depends on the chosen aperture and voltage and can be measured through the Faraday cup present on holder. An example of typical exposure parameters is shown in Fig. 2.18.

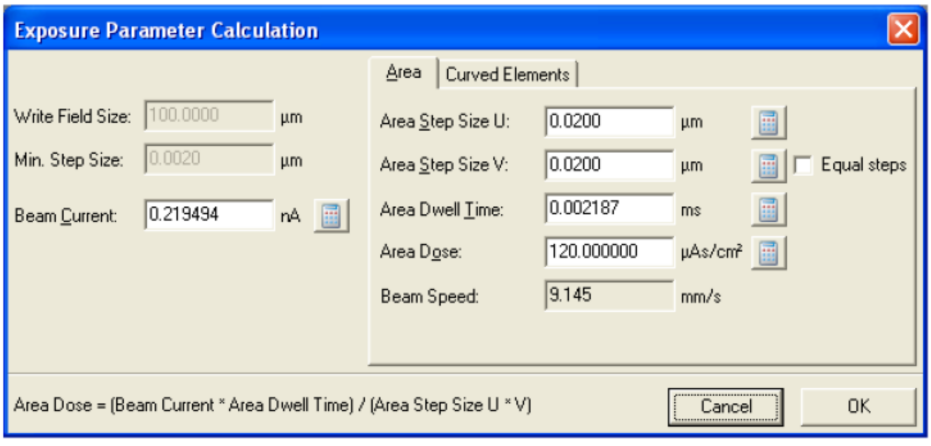


Figure 2.18. Raith software for exposure parameters settings.

Before proceeding with the exposure, the user must establish a local coordinate system and its origin, usually located to a substrate's corner, in order to locate the exposure into the desired area of the substrate, given in term of the above defined local coordinates. Moreover, a careful alignment procedure must be performed to avoid stitching errors; in addition, astigmatism and aperture alignment procedures

must be carried out, together with focus adjustments, in order to reduce beam aberrations and distortions. Only when all of these optimization procedures have been completed, the exposure can start: the beam moves toward the desired area and starts to expose the pattern with the set parameters. Once the resist exposure has been performed, the pattern is transferred to the resist layer through the development process, consisting into the substrate immersion into a proper developing solution for a time depending on the solution chemical composition and on the resist thickness. This patterning must then be transferred to the substrate through other fabrication steps, as it will be better explained hereafter.

2.2 Thin film deposition techniques

The thin film deposition techniques allow to deposit on a substrate a layer of material whose thickness can be of few nm up to few µm. Several deposition techniques have been developed so far [127]; they however can be classified depending on the phase of the material to be deposited, that can be in the liquid phase or in a vapor phase. In the following subsections, the most employed techniques will be described.

2.2.1 Liquid-phase deposition techniques

The liquid-phase deposition techniques are typically employed when the coating of a substrate with a polymer is required [128], for example for the coating of the substrate with the resist needed for the lithography process. The most employed coating techniques are here presented.

2.2.1.1 Casting coating

The drop casting coating is one of the simplest deposition techniques, since the only requirement is a very flat surface on which to place the substrate to be coated. Indeed, the deposition process consists into the casting of a solution onto a substrate and its drying in air [129], as it schematically shown in Fig. 2.19.

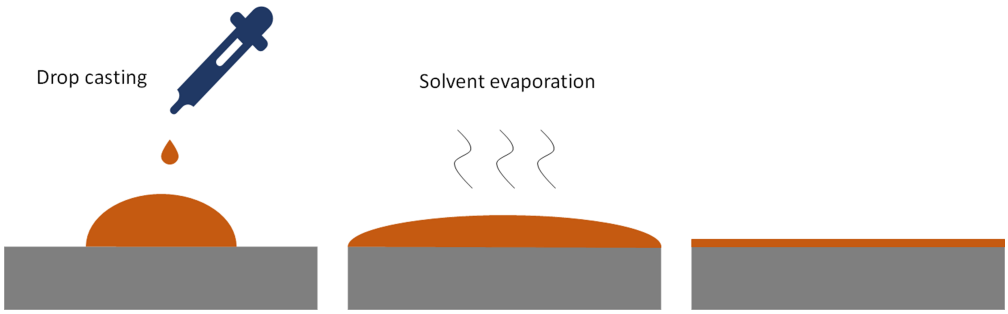


Figure 2.19. Schematization of drop casting technique.

This deposition technique suffers of a low control of the final film thickness and, sometimes, of the presence of some precipitates on the substrate during the drying process. For these reasons, other techniques are preferred when a higher control on the film properties is required.

2.2.1.2 Dip coating technique

Another process employed for thin film deposition is the dip coating technique. In this case, the substrate to be coated is vertically immersed into the precursor solution at a constant speed, where it remains for a certain dwell time in order to let the surface to be completely wetted by the solution. Then the substrate is lifted at a constant velocity from the solution: a thin film is deposited onto the substrate, while the excess liquid will drip from the surface. Finally, the solvent will evaporate from the surface, with a procedure that can be promoted with thermal treatments. In Fig. 2.20 a schematization of the dip coating technique is shown [130].

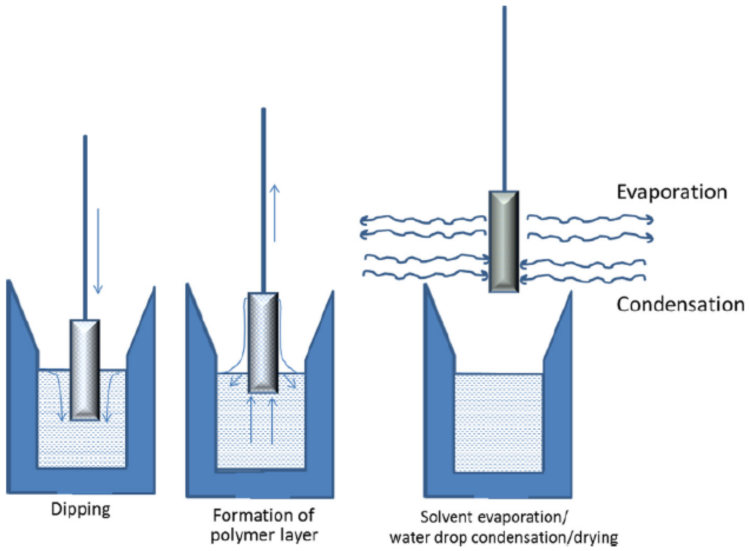


Figure 2.20. Schematization of the dip coating technique [130].

The final film thickness h_0 will therefore depend on the solution viscosity, the withdrawal speed and the liquid-vapor surface tension, according to the Landau-Levich relationship [131]:

$$h_0 = c \frac{\eta {U_0}^{2/3}}{\gamma_{LV}^{1/6} (\rho g)^{1/2}} \tag{2.5}$$

where c is a constant depending on the fluid properties, U_0 is the withdraw velocity, η is the liquid viscosity, γ_{LV} is the liquid-vapor surface tension, ρ is the fluid density and g is the gravity acceleration. This relation is particularly valid when U_0 is in the range of 1-10 mm/s, typical for the sol-gel deposition [132].

This deposition technique allows to deposit good quality films, but the dependence on the immersion/withdraw velocity may cause some troubles on the reproducibility of the final film thickness.

2.2.1.3 Spin coating technique

The widely employed technique for the deposition of thin film of liquid solutions onto a substrate is the spin coating, since it allows to obtain a highly uniform film

with a very good control and reproducibility of its thickness [133]. The film formation occurs by applying a drop of the liquid solution onto the substrate followed by its acceleration with a chosen rotational speed that will depend on the thickness to obtain. During this process, most of the liquid is ejected due to the centrifugal force until the desired thickness is reached, while most of the solvent is evaporated. After the spin coating process, a thermal treatment is performed in order to remove the residual solvent. In Fig. 2.21 [133] a schematization of such process is shown.

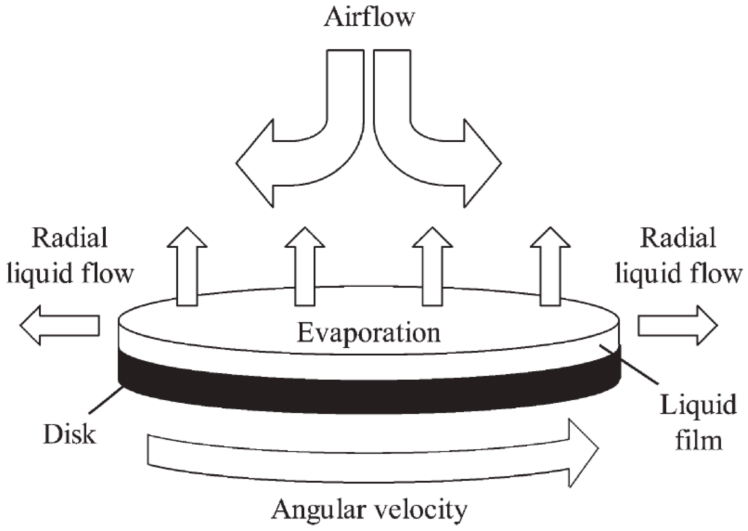


Figure 2.21. Schematization of spin coating process [133].

The final film thickness h can be expressed as [134]:

$$h = K \frac{c^{\beta} \eta^{\gamma}}{\omega^{\alpha}} \tag{2.6}$$

where c is the fluid concentration, η is its viscosity, ω is the rotation speed, while K, α, β and γ are calibration constants that depend on the fluid to be deposited.

Due to the high thickness control capabilities and its high reproducibility, spin coating technique has been chosen to deposit the electroresist layer employed for the EBL patterning. In particular, the resist used in this work is PMMA, that has been the first polymer tested as resist for EBL and that remains the most employed to achieve high resolution patterning. PMMA has been purchased from MicroChem Corp. [135] in liquid solution, using anisole as casting solvent. In particular, there are different PMMA types depending on the average molecular weight (MW) of its polymeric chains. The most used are 950k and 450k MW; the difference between these types lies into the different achievable resolution: it is considered, indeed, that higher molecular weights lead to higher resolution, because in high MW polymer the scission process produces smaller chain size and, as a consequence, higher resolution into the resist removal after its development. Among these types, 950k MW PMMA has been chosen for the lithographic processes carried out for the fabrication of the proposed devices. In Fig. 2.22, a picture of the deposition of PMMA on a Si substrate mounted on the spin coater is shown.

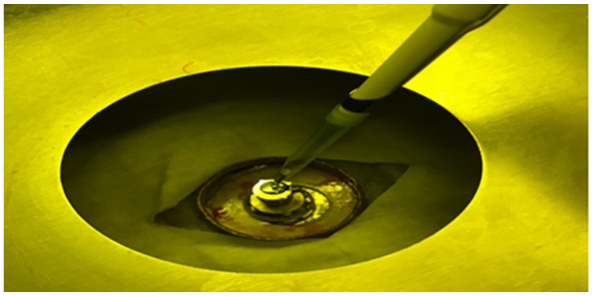


Figure 2.22. Deposition of PMMA on 1 cm x 1 cm Si substrate.

2.2.2 Vacuum deposition technique

Vacuum deposition technique is used to deposit layers of material atom-by-atom or molecule-by-molecule on a solid surface. These processes operate at pressures well below atmospheric pressure. These deposition techniques can be further classified in physical vapor deposition (PVD), where the material to be deposited change its phase from the solid to the vapor one and then is condensed on the substrate, and chemical vapor deposition (CVD), where the material deposition occurs through chemical reactions from some gas precursors and the target substrate atoms. Hereafter, the most employed techniques will be presented.

2.2.2.1 Thermal evaporation

The thermal evaporation is the simplest PVD method for thin film deposition. Indeed, a source constituted by the material to be deposited is heated until it reaches the evaporation state. Once this happens, the material vapor particles reach the substrate and here condense to form a thin film [136]. In order to avoid interactions between the vapor material and the chamber atmosphere, pressure below 10^{-4} Torr are used in these systems, so that the mean free path of the vapor atoms is comparable with the chamber dimensions and they can travel straight from the source to the substrate. The film formation occurs through several steps: the arrival of atoms onto the substrate, the adsorption on its surface and the diffusion on it, the nucleation and finally the film growth. Such process is schematically shown in Fig. 2.23, while a schematization of a typical thermal evaporation system is shown in Fig. 2.24 [137].

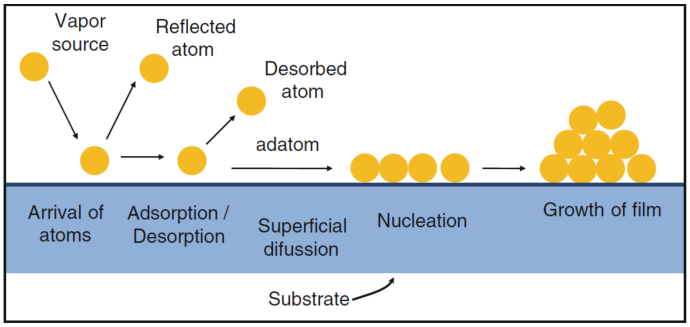


Figure 2.23. Schematization of the film growth by thermal evaporation [137].

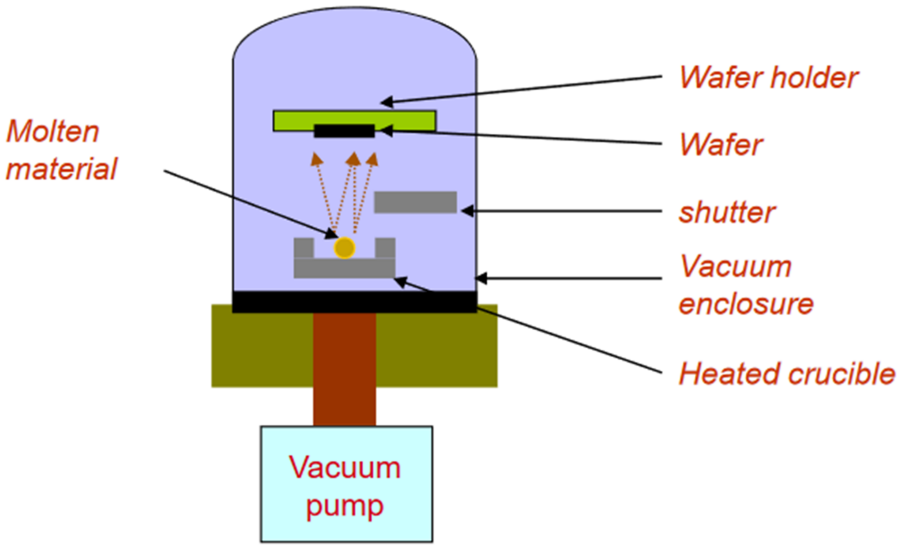


Figure 2.24. Schematization of a thermal evaporation system [137].

Different methods can be employed to heat the source, for example by a resistance heating or by the bombarding of the source through a high energy electron beam. Regarding the resistance heating method, the most used elements are spiral-shaped or V-shaped conductor filaments, like tungsten or molybdenum wires, if the material to evaporate forms a wire that can be directly melted increasing the current flowing through it. For materials forming powders, instead, metal boats or ceramic crucibles surrounded by a heated filament are used. The evaporation rate depends on the vapor pressure of the material to be deposited; moreover, the final film quality will depend on the substrate surface, being therefore low if such surface is rough or if the evaporation is performed in poor vacuum conditions. In addition, when the e-beam evaporation is performed, the high energy electron beam can induce x-ray damage to the substrate.

2.2.2.2 Sputtering deposition

Sputtering deposition is a widely and useful PVD technique for thin film deposition. In the basic sputtering process, a target plate (the cathode) constituted by the material to be deposited is bombarded with energetic ions generated in a glow discharge plasma (an ionized gas composed by an almost equal number of positive and negative charges and some un-ionized molecules) situated in front of the target. The plasma is needed to make the gas conductive and generate ions that can be accelerated toward the target to strike it. This bombardment process causes the removal, or sputtering, of target atoms, which then condense on a substrate as thin film [138].

Sputtering process can be run in direct current (DC, typical condition for conductive material deposition) or in radiofrequency (RF, for the deposition of insulating materials) mode. For a DC sputter deposition, a schematic diagram of the sputtering equipment is shown in Fig. 2.25 [138].

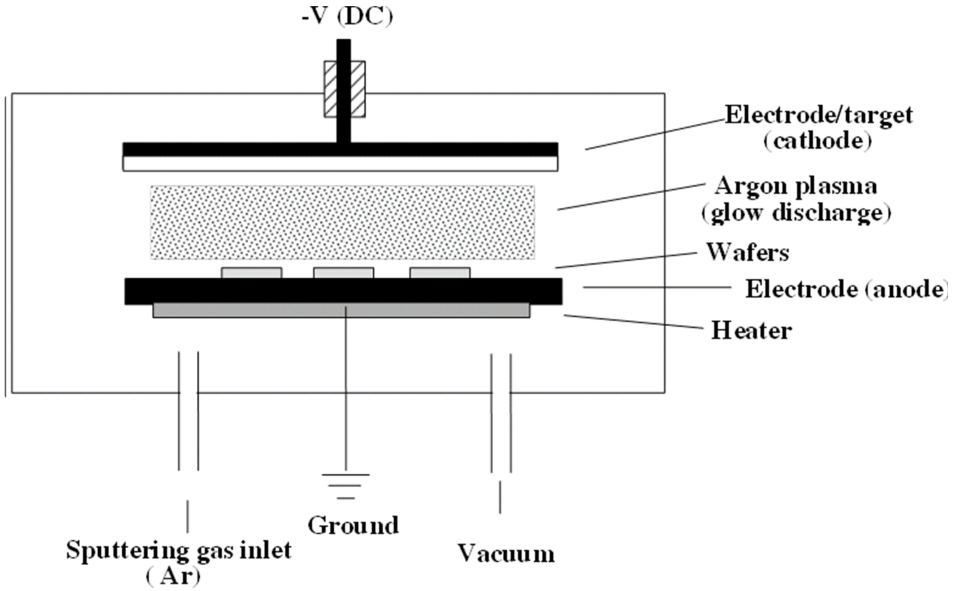


Figure 2.25. Schematization of a DC sputtering system [138].

Both the target than the substrate are placed in a vacuum chamber ($\sim 10^{-6}$ Torr); the plasma is created by ionizing a sputtering gas, which is typically a chemically inert heavy gas, like Argon. Ions are generated by the collision of neutral atoms with high energy electrons; the ionization process starts when a sufficiently high potential difference is applied between the electrodes. This potential accelerates the electrons toward the anode and make them collide with gas atoms, converting these ones into positively charged ions. The positive ions are accelerated toward the cathode, where the collisions will release other electrons by ion-induced secondary electron emission, which will, in turn, produce new ions and electrons in an avalanche process. In this way, the glow discharge becomes a self-sustaining plasma. This plasma is highly conductive due to the electrons, which move very fast toward the electrode; for this reason, the plasma is always positively biased relative to any electrode. This positive bias V_p accelerates Ar^+ ions toward both the electrodes; however, the bias voltage near the anode is small ($\sim$ 10 V), therefore there is no significant sputtering of the substrate (but there is however the possibility to damage it). On the other hand, the total bias on the target (V_p plus the applied voltage) is very high, leading to the sputtering of the target atoms. The principal parameters involved into this process are the gas pressure (P) and the distance between target and substrate (d). In particular, plasma can be turned on only if the following condition is fulfilled [139]:

$$P \cdot d > 0.5\, cm \cdot Torr \tag{2.7}$$

Indeed, very large P·d product leads to too many collisions that prevent electron energy buildup, while very small P·d product leads to very few collisions without ionizing atoms and very few ions to bombard and generate secondary electrons. When instead P·d product reaches a good value, which will depend on target material, the collision ionizations will produce secondary electrons which, in turn, will increase the number of electrons available for ionization.

This deposition technique allows to form a wide variety of films onto the substrate, such as metals, insulators, alloys or composites. The target material is sufficient for many depositions and the possibility to use large area target leads to the deposition of uniform films even on large substrates. Moreover, sputtering produces films with a better quality and coverage than evaporation and even the deposition control results to be more reproducible and easier through the deposition time. On the other hand, substrate damage can occur due to ion bombardment or the UV irradiation generated by plasma. The thin film deposition laboratory at Institute for Microelectronics and Microsystem (IMM – CNR Unit of Naples) is equipped with a BAL-TEC SCD 500 sputter coater, shown in Fig. 2.26.



Figure 2.26. BAL-TEC SDC 500 sputter coater.

This system allows the deposition of several metals (gold, silver, nickel, chromium, tungsten, titanium, molybdenum, copper, platinum, iron, cobalt) on substrates with a diameter up to six inches. For each of these metals exists a calibration curve with the corresponding operating current which ensures a good deposition rate at a working pressure of about 10^{-5} Torr.

2.2.2.3 Chemical Vapor Deposition

The chemical vapor deposition (CVD) technique allows depositing thin films of target materials by chemical reactions occurring onto a heated substrate. In particular, source gases are introduced into a reaction chamber where chemical reactions can occur due to heat, RF power or other techniques which result in the decomposition of the source gas and reaction of the resulting radicals on the substrate to form the film [140]. Indeed, within the reaction chamber, some phase reaction can occur between the precursor molecules, creating intermediate gas species that can be adsorbed onto the substrate. Here surface reactions occur which further decompose precursor molecules, starting to form the desired film together with volatile compounds that, instead, are desorbed from the surface and are pumped out from the system by the inert carrier gas or the vacuum system, depending on

the CVD system configuration. In the initial stage of this process, the atoms of the film are only weakly bounded to the substrate surface, therefore they can diffuse on it. Thanks to the heating of the substrate (> 200 °C), these weak interactions between the substrate and the deposited material become stronger and the growth of the film starts. A schematization of this process is shown in Fig. 2.27 [141].

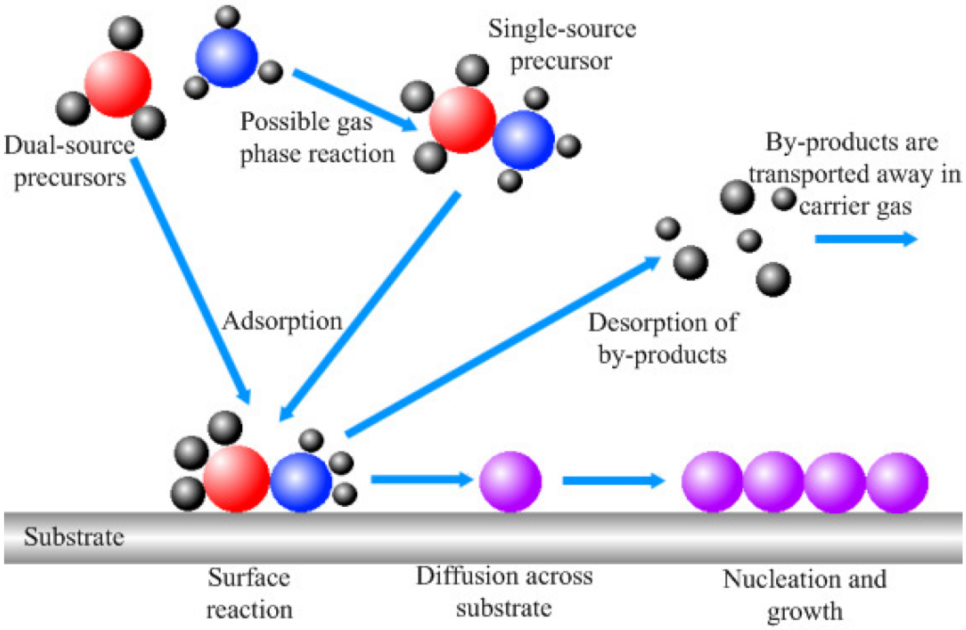


Figure 2.27. Schematization of a CVD process [141].

CVD deposition technique has several advantages respect to other deposition techniques: deposited films have an excellent adhesion, uniformity and deposition reproducibility; moreover, it is possible to easily control the crystal structure, surface morphology and the final stoichiometry of the deposited film due to the large number of optimizable process parameters, which have led to a great class of deposition techniques that can be classified into the CVD techniques family.

As an example, one class of the CVD techniques is the Low Pressure Chemical Vapor Deposition (LPCVD), where the reactions inside the chamber are performed at 1-10^{-3} Torr instead of atmospheric pressure. This reduction of the chamber pressure causes a reduction of the velocity of reaction, that, in turn, will produce final films with better uniformity, high reproducibility, and high homogeneity [142]. Unfortunately, temperatures usually above 600 °C are required for this process, limiting the possible substrates on which is possible to deposit thin films through LPCVD. A possible solution to reduce the substrate temperature is the Plasma Enhanced Chemical Vapor Deposition (PECVD), where the gas precursor reactions occur after the generation of a plasma within the reaction chamber, usually generated by a radiofrequency (RF) discharge between two electrodes [143]. The plasma, indeed, will bombard the reactive gas causing their dissociation; this allows to perform thin film deposition at lower temperatures (below 400 °C, down to 100 °C), but with at the cost of a higher stress for the substrate due to the plasma bombardment.

2.3 Etching processes

A fundamental step of a device fabrication is the etching process, which allow to transfer the pattern obtained into a sacrificial layer to the substrate through a mechanism of material removal, where the sacrificial layer act as an etching mask, usually. There are two main etching types:

- *Wet etching*, when the patterned substrate is immersed into a liquid etchant solution which can selectively remove material from the substrate;
- *Dry etching*, when the material removal happens without any solvent.

In the following subsections, a more detailed description of these etching processes will be presented, with a higher attention to the processes employed for the development of the proposed devices.

2.3.1 Wet etching processes

In the wet etching process, the substrate is immersed into the etchant solution where a chemical reaction between the substrate surface and the etchant occurs, as shown in Fig. 2.28 [144].

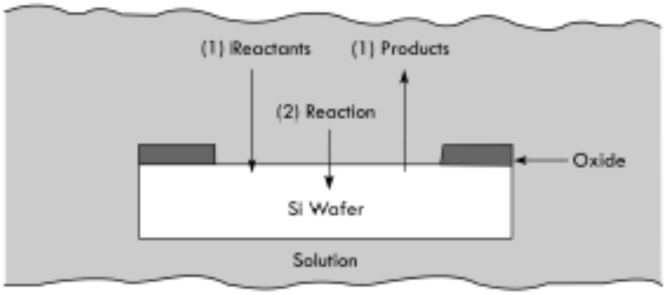


Figure 2.28. Schematization of the wet etching process [144].

The etching rate is controlled through the temperature and through the immersion time, which will depend on the type and quantity of material to be removed. After etching, substrate is rinsed, usually in de-ionized (DI) water, to remove etchant residual and then dried with nitrogen gas. Due to the high etching rates and the high isotropy of this process, the resulting vertical profile is sloped rather than straight. Moreover, the subsequent rinse and drying steps increase the possibility of impurity contaminations which will produce fabrication defects. In addition, if the etching time exceeds the required time, there would be the removal of material even under the masking layer, according to a phenomenon called *over etching* which will cause an undercut vertical profile, as schematically shown in Fig. 2.29.

Referring to Fig. 2.29, if h_f is the thickness of the material to be removed and l is the under etch length, the anisotropy degree (A_f) can be defined as [144]:

$$A_f = 1 - \frac{l}{h_f} = 1 - \frac{R_l t}{R_v t} = 1 - \frac{R_l}{R_v} \tag{2.8}$$

where R_l and R_v are the lateral and vertical etching rate, while t is the etching time.

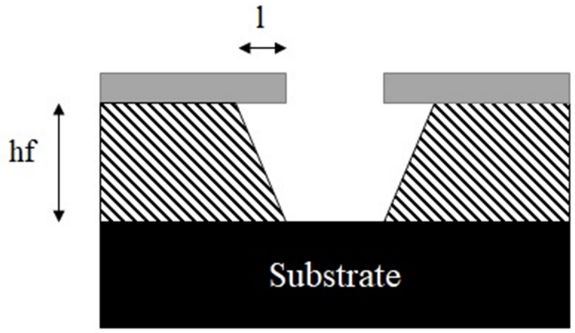


Figure 2.29. Schematization of an undercut profile due to the over etching.

The undercutting of the layer under the mask results in a loss of lithography resolution. For these reasons, wet etching process is usually preferred only when large areas have to be etched; when the etching area is instead small and, above all, a higher etching resolution is required, the dry etching process is preferred, even if its etching rate is much smaller than wet etching one.

2.3.2 Dry etching process

In contrast with wet etching process, dry etching causes material removal without any solvent. This process deals with plasma-assisted etching, in which a film is removed by chemical, physical or both reactions between the etchant species generated into the plasma and the surface atoms of the layer to remove. A schematization of such process is shown in Fig. 2.30 [144].

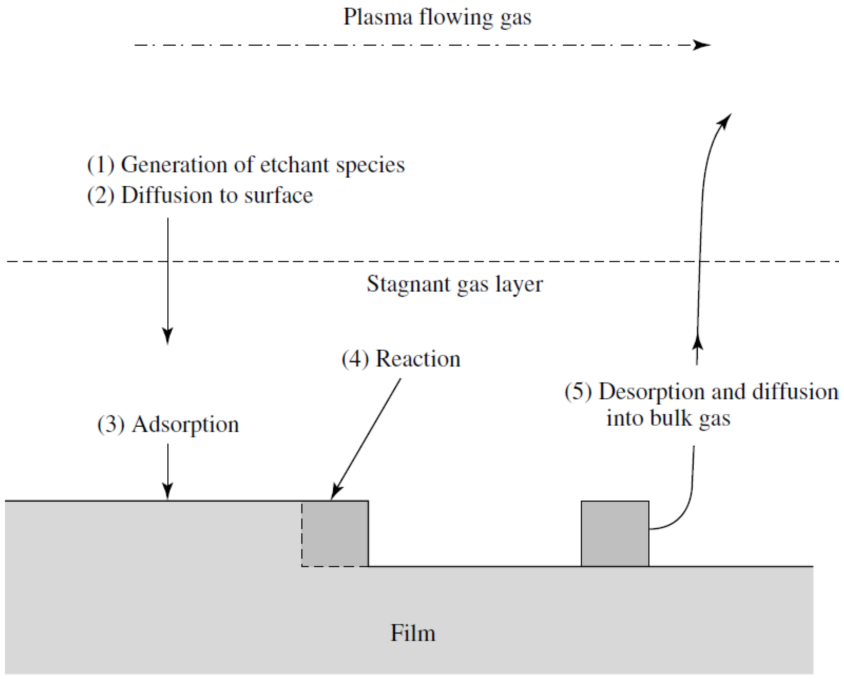


Figure 2.30. Schematization of dry etching plasma mechanisms [144].

First, the etchant species are generated into the plasma and are then transported by diffusion to the surface; then the reactant is adsorbed on the surface where a chemical reaction, along with physical effects such as ion bombardment, occurs to form volatile compounds that are desorbed from the surface and pumped out by the vacuum system.

For dry etching, therefore, two different etching mechanisms can occur: physical etching and chemical etching. For physical etching, positive ions generated into the plasma bombard the surface at high speed and high energy, removing atoms from the unmasked region of the layer to etch. In chemical etching, instead, neutral reactive species generated by the plasma interact with the material surface and form volatile products. The characteristics of such mechanisms are different; in particular, chemical etching shows a high etch rate, good selectivity (the ratio of etching rate for different materials) and low ion-bombarding damages, but isotropic profiles. On the other hand, physical etching exhibits isotropic profiles, but it is associated with low etch selectivity and high bombardment damages. When both etching mechanisms are combined, like in reactive-ion etching (RIE), it is possible to etch materials with a good anisotropy degree, a good selectivity (depending on the mixture of the employed gas and the material to etch) and moderate bombardment-induced damages. For these reasons, RIE has been widely used in manufacturing and research for microelectronic fabrication [145]. In Fig. 2.31, a schematization of a typical RIE system is shown [144].

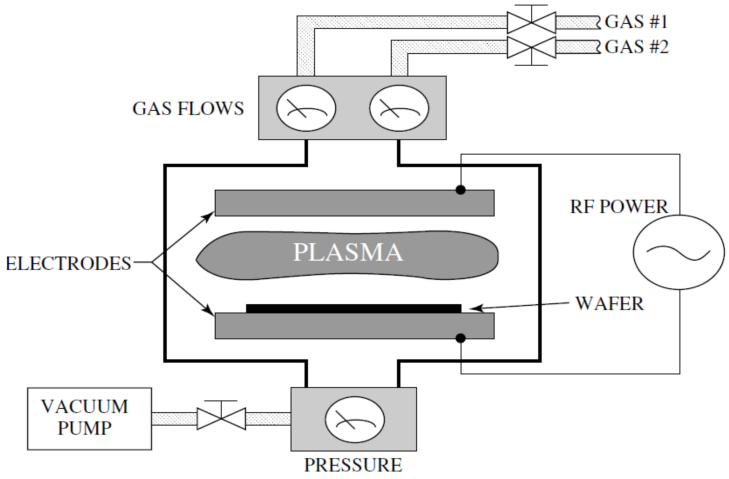


Figure 2.31. Schematization of a typical RIE system [144].

In a parallel plate system, a RF capacitively coupled electrode holds the wafer. The grounded electrode is constituted be the whole chamber, ensuring therefore a large area electrode which, combined with the low operating pressure (< 500 mTorr) causes the substrate to be subjected to heavy high energetic ions bombardment. Plasma is generated by applying a strong RF electromagnetic field to the wafer plate; the typical used frequency is 13.56 MHz at a power of few hundred watts. At every field cycle, electrons are accelerated up and down into the chamber due to their low mass which allow them to follow the field oscillations. On the other hand, ions are much heavier, therefore they are not able to follow field oscillations. When

the electrons strike the chamber walls, they are fed out to ground without altering the charging status of the system; when they are deposited onto the substrate plate, since it is connected to a blocking capacitor, a charge buildup occurs on this plate, which is therefore negatively biased (the bias voltage). Simultaneously, the plasma develops a slightly positive charge due to the higher ions concentration respect to free electrons. Due to the high potential difference, the positive ions tend to migrate toward the lower electrode, where they collide with the sample to etch and, if the kinetic energy transfer is sufficiently high, some material can be sputtered from the sample surface; moreover, they react chemically with the materials on the surface generating volatile products that are desorbed from the surface and exhausted from the chamber.

Even if the major advantage associated with RIE is the ability to obtain an almost anisotropic etching, other advantages can be obtained as well. Indeed, only relatively small amounts of gas are used, which implies both cost and environmental advantages relative to wet etching process, where large volume of corrosive and sometimes hazardous liquids are used. Moreover, the fact that plasma etching is carried out in vacuum conditions implies an almost impurity-absent process, but at the cost of high capital equipment.

In most microelectronic fabrications processes, fluorine-based gases are used, because F atoms each silicon (Si) even without any ion bombardment (but with a low process rate) [146], while silicon dioxide (SiO_2) is etched by F atoms more slowly [147]. When F atoms are incident on Si substrate in absence of particle bombardment, a stable layer of fluorinated silicon is formed [148]. To remove this layer, a chemical reaction between this layer and F incident atoms must occur. When there is the ion-enhanced etching, this fluorinated-silicon layer is subjected to a gasification process through the formation of SiF_4 compounds: the fluorinated layer becomes volatile and the clean silicon is exposed again to the flux of F atoms, as it is schematically shown in Fig. 2.32 [149].

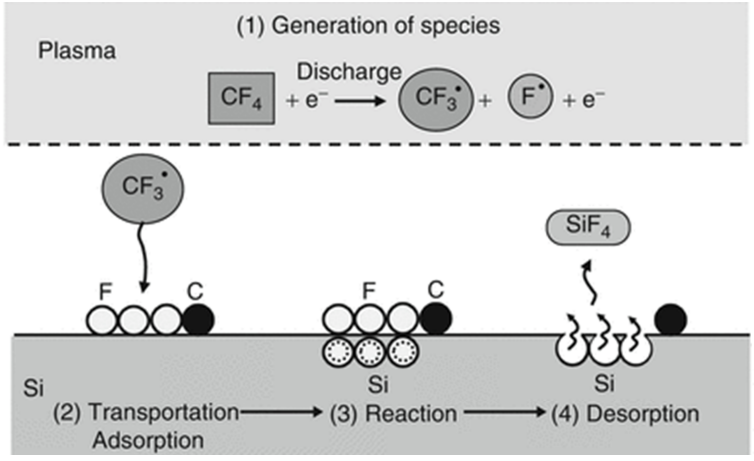


Figure 2.32. Schematization of the generation of SiF_4 volatile compounds during fluorinate gas etching of silicon [149].

The etching rate of F atoms on clean Si results to be much higher than on fluorinated silicon, provided that the flux of F atoms is large enough to keep the

average fluorine coverage of Si lower than the saturation value reached during F atoms exposure alone. This mechanism, however, is not limited to the silicon-fluorine systems, but is responsible for much of the ion-enhanced etching which has been observed with other chemical systems [150].

There has been a large number of etch gases combinations used in plasma etching, because different etching rates and selectivity can be obtained for each of these. As an example, one of the most used etching gas for Si is tetrafluoromethane (CF_4); this gas, however, shows equal selectivity when etching Si/SiO_2 stack layers. A higher SiO_2/Si selectivity can be obtained using fluorine-deficient discharge, for example by using CHF_3 as etching gas [150]. Indeed, the presence of the oxygen on the SiO_2 surface lattice causes its reaction with the carbon atoms to form CO, CO_2 or COF_2 volatile compounds. There is thus a lower consumption of fluorine for SiO_2 respect to the Si surface, therefore the deficiency of F atoms in CHF_3 respect to CF_4 affects the etch rate of Si more than the etch rate of SiO_2. On the other hand, when a high Si/SiO_2 selectivity must be obtained, it is preferable the use of etch gas with large fluorine atoms concentrations, like CF_4+O_2, SF_6, etc.

In the fluorocarbon plasma etching of Si, the addition of oxygen leads to the increase of the etching rate, because the oxidants reduce the rate of radical recombination. Indeed, when CF_4 is dissociated to form CF_3 and F, these molecules could maybe re-combine losing the active species; however, if CF_3 species recombines with oxygen atoms to form CO or COF_2, now F atoms are still available producing more fluorine atoms for etching. Anyway, this process relies on the probability of recombination between the radicals and the oxidant; moreover, these fluorine-based gases induce an almost isotropic etching; to obtain anisotropic etching the use of chlorine- or bromine-based etch gases must be preferred.

Another key parameter of plasma etching is the pressure of the plasma. At higher pressure, the plasma density increases, but at the same time there is a smaller mean free path of the electrons before colliding, therefore there is less directionality of the ion bombardment. Finally, an increase of the RF power produces an increase of both density and energy of free electrons, increasing the bias voltage of the plasma and, in turn, the etching rate. A schematization of the etching rate dependence on the plasma pressure and the RF power is schematically shown in the left side and the right side of Fig. 2.33, respectively [151].

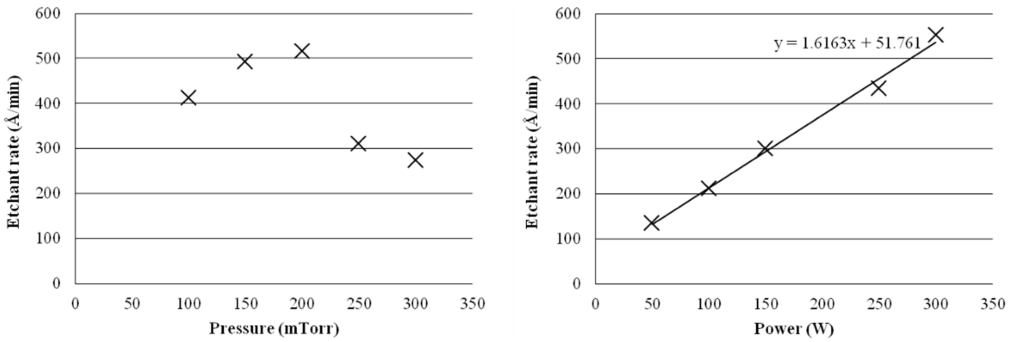


Figure 2.33. On the left, silicon etching rate trend as a function of the working pressure. On the right, silicon etching rate trend as a function of the RF power [151].

When a RIE process is going to be performed, all of these aspects must be taken into account in order to find the best parameters set which would lead to a device fabrication corresponding to the design specifications. In addition, also the mask material constitutes a very important choice, since the mask resistance to the etching process determines the RIE process success. Usually, resist resistance to etching process is quite low; for this reason, metallic masks are often preferred, especially for deep RIE process [152] where aluminum and nickel are the most employed metals.

2.3.2.1 RIE equipment

The Clean Room (Class 10000) at Institute for Microelectronics and Microsystem (IMM – CNR Unit of Naples) is equipped with an Oxford Plasmalab 80 Plus RIE system shown in Fig. 2.34.

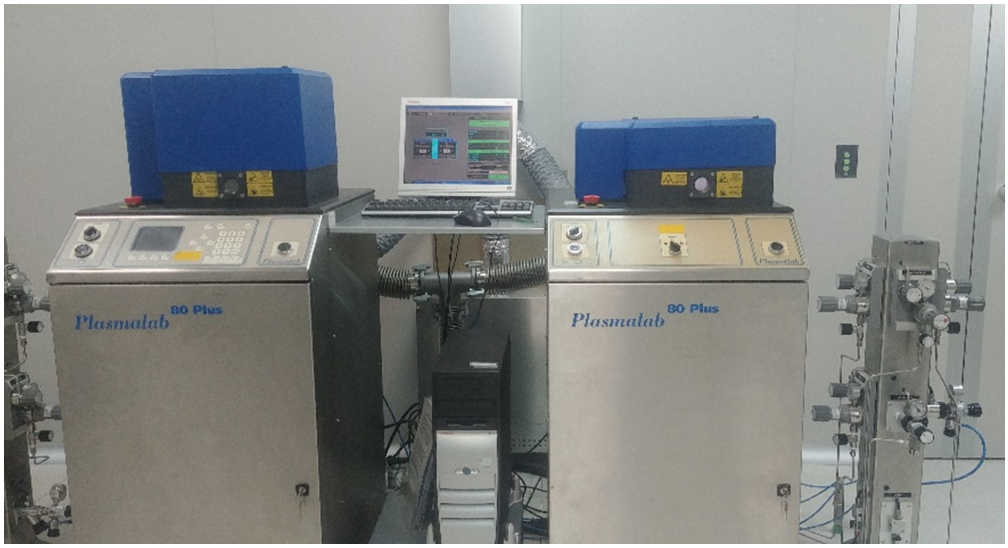


Figure 2.34. Oxford Plasmalab 80 Plus RIE system.

This RIE system is equipped with a RF generator with a power up to 500 W; the gas lines allow the introduction of CF_4, CHF_3 and O_2 whose flow rate can be controlled through a graphical interface which allows the control of all the etching parameters (RF power, gas flow rate, chamber pressure) settable from the user and the parameters deriving from the process (RF reflected power, bias voltage). This system, together with the EBL system described in Sect. 2.1.3 and the sputtering system described in Sect. 2.2.2, has been employed for the fabrication of the devices developed during this work thesis, which will be shown in the next Chapter.

Chapter 3

Integration of plasmonic and photonic devices on silicon substrate

The work of this thesis has been the development of three silicon-based devices: a plasmonic biochemical sensor, a silicon-based metasurface for all-optical switching application, and a silicon-based grating for interconnect applications. These devices fall within the three main application fields of silicon photonics highlighted into the short review presented in Chapter 1.

In the following subsections, a detailed description of the proposed devices, their possible applications and their fabrication processes will be shown.

3.1 Silicon-based plasmonic nanoantennas for biochemical sensing

One of the developed devices has been a silicon-based optical biosensor for infrared spectroscopy (IR) applications. IR spectroscopy can provide direct information on functional groups occurring in a molecule through their own characteristic absorption spectrum in a univocal, non-destructive and label-free way. In particular, there are two main areas for the analysis of an IR spectrum [153]:

- a high frequency region (between 3000 and 1300 cm^{-1}), called *region of functional groups*; if the IR spectroscopy reveals the absence of absorption in correspondence of the frequency ranges assigned to the various functional groups, this result can be used as the evidence for the absence of such groups in the analyzed molecule.
- an intermediate region of the spectrum (between 1300 and 900 cm^{-1}), usually called as *fingerprint region* since the absorption features into this region are unique for every molecule.

However, infrared spectroscopy is characterized by a very low molecular absorption cross-section of infrared vibrations ($\sigma_{abs} \approx 10 \div 20$ cm^2); as a consequence, a

large amount of material is necessary for accurate determinations. For this reason, the spectroscopic characterization of minute amounts of analytes, often required for sensing applications, is not practical, since extremely weak signals are expected on the basis of Beer's Law predictions [154]. This fundamental limitation, however, can be overcome by means of metallic nanoantennas (NAs) supporting localized surface plasmonic resonances (LSPRs). These metal NAs (that are generally deposited dielectric or semiconductor substrate) have sub-wavelength size and the symmetry properties of their shapes determine their response respect to the incident electromagnetic (EM) radiation [155]. Moreover, they can be arranged in a 2D-array geometry forming a metasurface, whose optical response can, in principle, be tailored in any region of the electromagnetic spectrum by varying the periodicity of the 2D-array as well as the shape, size and metal film thickness of each NA [156]. For spectroscopic and sensing applications in the infrared range, highly efficient sensing devices can be designed exploiting the significant enhancement of IR signal in well-defined infrared region [157]. In particular, it is possible to increase the sensitivity in the detection of chemical and biological substances when two dimensional 2D-array of plasmonic nanoantennas are used in the Surface Enhanced InfraRed Absorption (SEIRA) spectroscopy [158]. The condition needed by metasurfaces to probe the presence of chemical and biological substances adsorbed on their surface is the accordance between the plasmonic resonance of the functionalized NAs and the wavelength value at which the maximum absorption of the substance occurs [159]. When this condition is fulfilled, the narrow vibrational signature of interest appears like a modulation of the large plasmonic background, causing a variation of the value of the metasurface reflection coefficient and allowing the identification of the adsorbed species. The resonance wavelength scales linearly with antenna's length (L) and with the refractive index (RI) of the surrounding medium [160]; this dependence offers the possibility to tailor an optimized design of the NAs and, through nanofabrication technologies, to obtain metasurfaces with the desired resonance wavelength. Several theoretical and experimental investigations have focused the attention on understanding how variations of the shape and/or the geometrical parameters characterising both the NAs and the resulting 2D-array influence the SEIRA detection sensitivity. Several types of NAs, different in shape [161], size [162], geometrical parameters [163] and thickness [164] have been proposed in order to explore their influence on the metasurface detection sensitivity. Indeed, the variation of even just one of these parameters results in a shift of the peak wavelength λ_{res} of the metasurface reflection/transmission curve, in the change of the maximum achievable reflection coefficient and in the bandwidth measured at full width at half maximum.

The device proposed in this work thesis consists in a large-area coverage array of cross-shaped gold NAs developed for vibrational sensing in the mid-infrared range through commercial instruments like Fourier Transform Infrared (FTIR) spectrometers. Among all the possible plasmonic materials, gold has been chosen since it can be easily functionalized with a thiol-based chemistry [165]. The cross-shaped design makes NAs insensitive to the polarization of the electromagnetic radiation impinging the active area. This feature is very useful for their utilization as bio-molecular sensors, given the random orientation of the dipole moments of molecules. Moreover, cross-shaped NAs show an increase of about a factor two of the SEIRA sensitivity respect to what expected by employing rod shape NAs [166]. At

the same time, the array arrangement ensures a good near-field signal enhancement arising from the coupling between neighbour NAs. The combined collective and individual plasmonic responses of the 2D array of NAs play a crucial role to obtain signal enhancement factors of $10^4 \div 10^5$. In addition, this array has been fabricated on a silicon substrate instead of the typically used substrates for IR measurement, like calcium fluoride (CaF_2) [167]. These materials, indeed, are optically transparent at the IR wavelengths, and are therefore used for SEIRA spectroscopy measurement conducted in transmission geometry. However, they show poor adhesion with resists and metals, making their employment difficult for silicon technology and also for in-vivo applications [168]. Therefore, if the 2D NAs array is designed in order to have a maximum of the reflection coefficient in correspondence of the wavelength of interest, it can be fabricated on a silicon substrate in order to perform SEIRA measurements in reflection geometry.

Due to the high quality, precision and reproducibility of the Electron Beam Lithography technique in terms of arrangement of nanostructures, very homogeneous, robust and recyclable arrays of cross-shaped gold NAs have been fabricated on a float-zone silicon wafer. The NAs exhibit a LSPR which is very sensitive not only to refractive index changes in the surrounding medium, but also to the specific molecular vibration band emerging from surface adsorbed molecules. In particular, acting on the array geometrical parameters, two sets of NAs have been designed and fabricated, one able to detect molecules in the absorption region of the nitrile group, characterized by the stretching of the triple bond C≡N occurring at 2100 cm^{-1} (corresponding to a $\lambda = 4.76$ µm) and the second one capable of detecting molecules in the absorption region of the carbonyl group, characterized by the stretching of the double bond C=O (around 1700 cm^{-1}, corresponding to a $\lambda = 6.25$ µm). In the following subsections, the description of the numerical results, of the fabrication process of these two set of NAs and the experimental results will be shown.

3.1.1 Numerical simulations

Thanks to a collaboration with prof. Elia Palange (University of L'Aquila) and his research group, the spectral response of the metasurface has been evaluated through numerical simulations by using COMSOL Multiphysics virtual environment. This allowed to design optimised 2D-arrays of gold NAs and to fabricate high sensitivity SEIRA sensors for any fixed resonant wavelength [169]. In Fig. 3.1 a schematization of the array geometry is shown; in particular, for the numerical simulation, a unit cell of the 2D-array composed by a single NA has been considered.

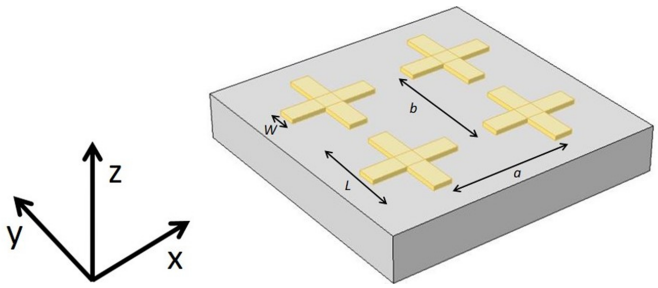


Figure 3.1. Schematization (truncated) of the simulated cross-shaped NAs array.

This unit cell is illuminated by an unpolarised EM plane wave propagating along the z-axis and impinging at normal incidence on the metasurface. Starting from the unit cell, the NAs 2D-array was obtained by using periodic boundary conditions along the x- and y-axes (i.e. the metasurface plane) and the scattering boundary conditions along the z-axis. In Fig. 3.1 L is the length of the cross arm, W the cross width and a = b the distance between two adjacent crosses that defines the 2D-array periodicity.

The NAs 2D-arrays are located on a float-zone silicon substrate that is optically transparent in the middle and far infrared regions of interest. In order to tune the metasurface response to the desired wavelength, the 2D-array periodicity has been fixed to be a = b = 2 µm, the cross width has been fixed to W = 0.2 µm and the NAs thickness has been fixed to t = 55 nm (resulting from 5 nm of chromium and 50 nm of gold, as it will be better explained in Sec. 3.1.2). By varying the only free parameter, i.e. the cross arm length L, the resonance peak of such NAs array has been tuned to the maximum absorption wavelength of the substances used for the SEIRA experiments. In particular, L = 850 nm was the value of the cross-length obtained from the simulations to have a metasurface resonance at the wavenumber equal to 2100 cm^{-1}, corresponding to the vibration band of nitrile group. Under these conditions, the resulting metasurface peak reflectivity is equal to about 46% (shown in Figure 3.2, red curve). The cross-length L = 1100 nm has been instead obtained to achieve the metasurface resonance centred at 1660 cm^{-1} to probe the vibrational band of the carbonyl group ranging between 1820 and 1620 cm^{-1}. In this case, the metasurface maximum reflectivity results to be equal to 56% (shown in Fig. 3.2, black curve). These values of the NAs 2D-array geometrical parameters have then been used to fabricate the metasurfaces, as it will be better explained in the next subsection.

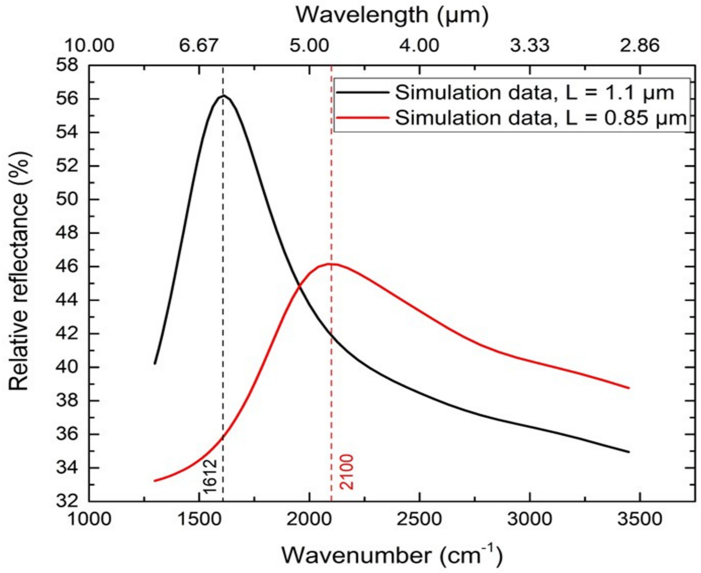


Figure 3.2. Simulated reflectivity response of the metasurfaces with NAs length L = 1100 nm (black curve) and L = 850 nm (red curve).

3.1.2 Fabrication process

Homogeneous NAs 2D-array have been fabricated on large areas as required for practical applications. The area coverage spun from 1 mm^2 to 25 mm^2, in order to be easily mounted on commercial FTIR instrument. The large area sample was fabricated by Electron Beam Lithography, by stitching up to 2500 writing field of size 100 x 100 μm^2. With this write field size the stitching error is estimated to be 7 nm, enabling the fabrication of gold NAs with well-defined geometrical parameters. The fabrication steps, summarized in Fig. 3.3, have been the following:

- deposition, via spin coating, of $\sim$ 280 nm-thick PMMA film;
- PMMA exposure by means of Electron Beam Lithography;
- PMMA development in 1:3 MIBK to IPA developer solution for $\sim$ 45 s;
- deposition, by DC sputtering, of 5 nm-thick chromium (Cr) buffer layer;
- deposition, by DC sputtering, of 50 nm-thick gold (Au) layer;
- lift-off process.

All of the fabrication steps have been performed into the laboratories of the Institute for Microelectronics and Microsystems - Naples Unit, of the National Council of Research (CNR – IMM, Unit of Naples).

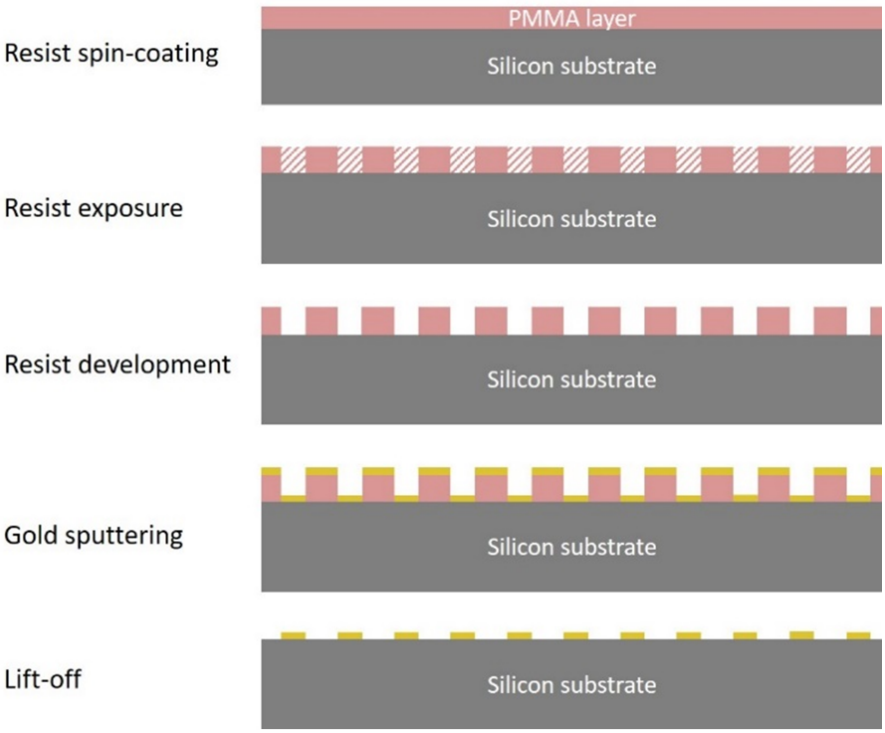


Figure 3.3. Fabrication flow chart for gold NAs fabrication.

The lift-off process allows to transfer a pattern to a substrate through an additive method. It requires the deposition of a thin film of the target material (in our case a gold film) onto a patterned resist layer; the substrate is then immersed into a resist remover solution which strips away the resist layer leaving on the substrate only the thin film whose adhesion occurred directly on the substrate. The lift-off process for the fabrication of the proposed devices has been carried out by immersing the substrate into a hot PG remover for $\sim$ 15 minutes, followed by an ultrasonic bath for $\sim$ 10 s and N_2 rinsing.

When a lift-off process is performed, some precautions must be taken. The first one regards the resist thickness: for this process to succeed, the resist thickness must be at least three times greater than the metal one. When this condition is not fulfilled, the metal particles could adhere to the resist vertical walls, being then removed during the ultrasonic bath. For the same reason, the walls of the resist should be not perfectly vertical, but an undercut profile is preferred for a masking of the underlying substrate during metal evaporation/sputtering. As a consequence, when considering a lift-off process, a low-energy lithography is preferable, since it will provide a better profile of the resist vertical walls for this kind of applications. Anyway, it is possible to perform a high-energy lithography even when the lift-off process is going to be carried out: in this case, the use of a co-polymer with higher sensitivity will provide the needed undercut profile, ensuring a good-quality lift-off.

For the fabrication of the proposed device, a low-energy lithography has been performed, with an acceleration voltage of 10 kV, a numerical aperture of 30 µm, a dose of 120 µC/cm^2 and a step size of 20 nm. With this exposure parameters set, only 26 hours were necessary to expose a 25 mm^2 area, showing that with a proper optimization of the exposure parameters the throughput achievable with EBL is not dramatically low as expected. The choice of a low acceleration voltage, together with the resist thickness related to the metal film thickness, ensured the lift-off process success; the Cr buffer layer was used to improve the gold adhesion on silicon substrate, in order to further enhance the device robustness. In Fig. 3.4a, a photograph of a 9 mm^2 active area placed on a 10 x 10 mm^2 silicon substrate is shown, while, in Fig. 3.4b, a micrograph of a 25 mm^2 area device is reported.

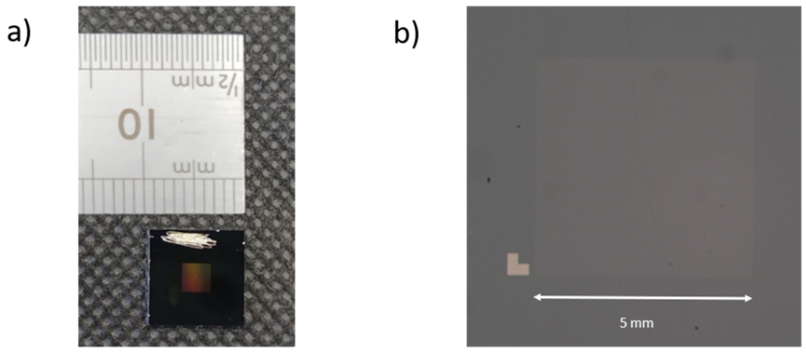


Figure 3.4. a) A photograph of a fabricated device with 9 mm^2 coverage area. b) A micrograph of a 25 mm^2 device.

In order to verify whether the fabricated cross-shaped NAs dimensions correspond to those assigned by the numerical results, a SEM analysis has been performed. In

particular, Fig. 3.5 shows the SEM analysis of the NAs array with the arm length L = 850 nm, while, in Fig. 3.6, the SEM analysis of the NAs array with the arm length L = 1100 nm is shown. For both set of NAs arrays an excellent agreement between the design parameters and the fabricated device has been obtained, with a fabrication tolerance lower than 5%. Moreover, in order to verify also the NAs thickness, an AFM analysis has been performed; it is shown in Fig. 3.7 for a L = 1100 nm cross.

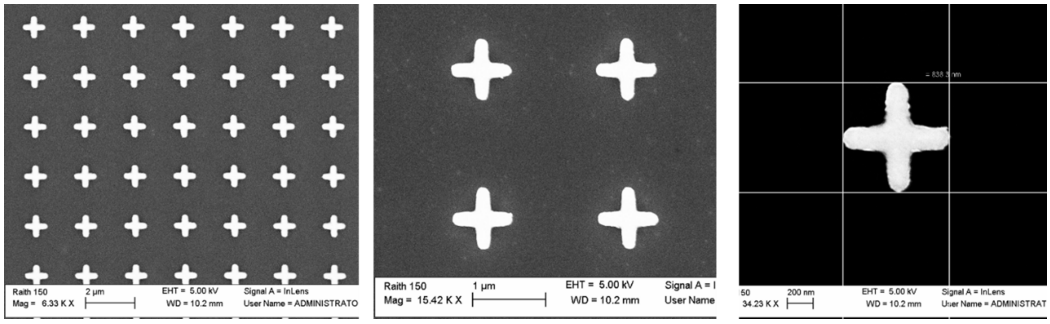


Figure 3.5. SEM images of the L = 850 nm NAs array.

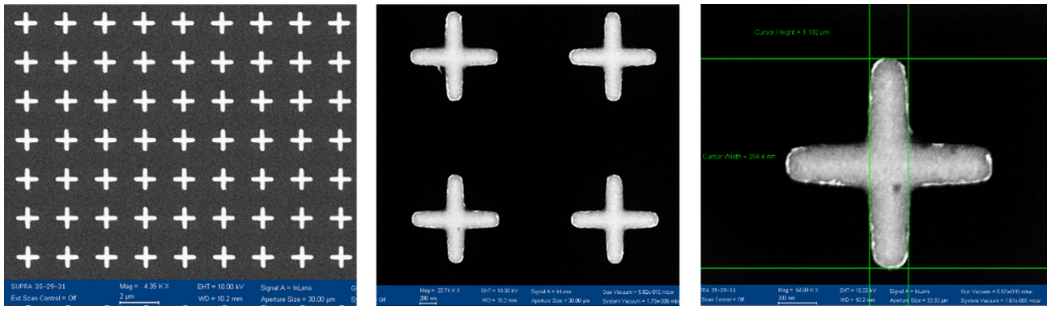


Figure 3.6. SEM images of the L = 1100 nm NAs array.

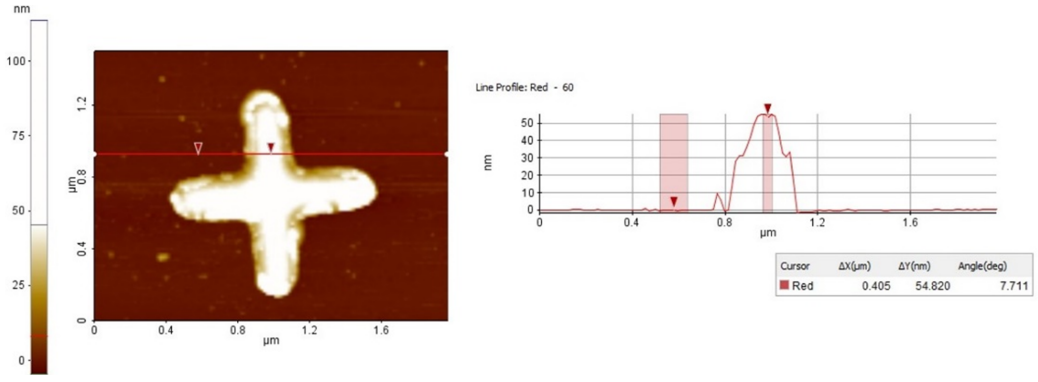


Figure 3.7. AFM analysis of NAs array.

The fabricated devices have then been tested in two different experiments in order to verify the device sensing capabilities, as it will be shown in the next subsection.

3.1.3 Device characterization

In order to demonstrate the SEIRA activity of the fabricated NAs, two distinct experiments have been performed, one aimed to the detection of small molecules and the other to the detection of large molecules.

In both experiments, two different regions of the infrared spectrum have been investigated: one at around 2100 cm^{-1} (where the stretching band of the triple bond C≡N of the nitrile group is normally detected) with the NAs array whose arm length was L = 850 nm; the second one occurring around 1700 cm^{-1} (where the stretching bands C=O of the carbonyl group resonates) with the NAs array whose arm length was L = 1100 nm. Both devices have been initially characterized before molecules adsorption in order to perform a comparison between measured and simulated reflection spectra of the NAs arrays. These spectra have been recorded at Università degli Studi della Campania "Luigi Vanvitelli", thanks to a collaboration with prof. Maria Lepore, with a Perkin Elmer Spectrum One Fourier Transform Infrared (FTIR) spectrometer equipped with a Perkin Elmer Multiscope infrared microscope and a mercury cadmium telluride (MCT) nitrogen cooled detector. The objective used for the measurements had a 10× optical or 15× infrared magnification. During the experiments, knife-edge apertures were set to form a 200 x 200 μm^2 measurement area. A background spectrum was measured with an aperture of the same size on a 50 nm thick gold film deposited on the same substrate as a reference. The measurements were made at room temperature by collecting the signal in the spectral region between 4000 and 600 cm^{-1} using 128 scans with a spectral resolution of 4 cm^{-1} and 5 s as acquisition time for each spectrum. As it is shown in Fig. 3.8a, a plasmonic resonance peaked at a wavenumber of 2099 cm^{-1} with a relative reflectance of 45% is present for NAs array with L = 850 nm. On the other hand, a plasmonic resonance peaked at a wavenumber of 1666 cm^{-1} with a relative reflectance of 56% is present for NAs array with L = 1100 nm. The positions of the peak resonances are well fitted with the simulated model discussed above, confirming the model as a useful guide for the design of NAs arrays with specific resonance peaks.

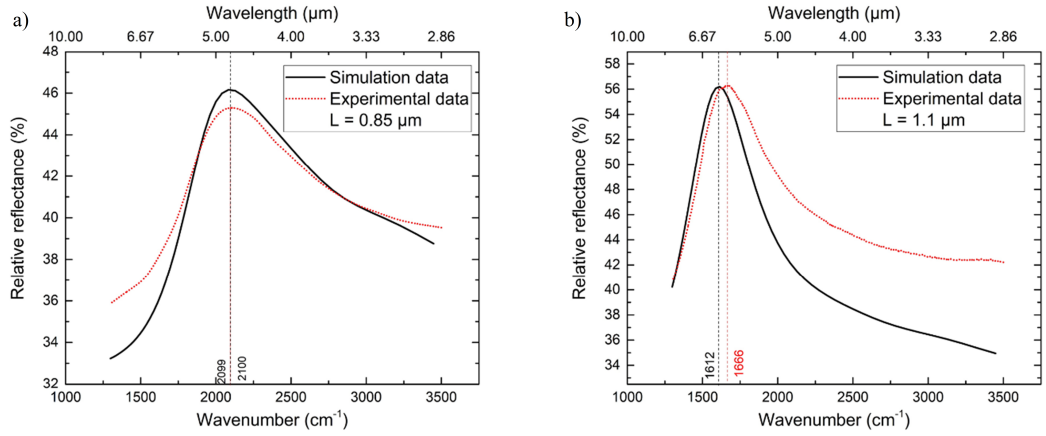


Figure 3.8. Comparison of simulated and experimental reflectance curve for naked NAs arrays (no compounds adsorbed), with a fixed period of 2 μm, NAs width of W = 200 nm and different NAs length: (a) L = 850 nm; (b) L = 1100 nm.

3.1.3.1 Small molecules sensing

The experiment performed for the detection of low molecular weight (MW) molecules has been carried out with the L = 850 nm NAs array. In particular, thanks to a collaboration with Dr. Menotti Ruvo (Institute of Biostructure and Bioimaging, National Council of Research) and his research group, a Pentynyl Cysteine-Amide (compound I) specimen has been designed and prepared. This compound contains on one end a thiol group for proper anchoring on the gold surface and on the other a nitrile group which resonates at about 2100 cm^{-1}. An azide-containing compound (compound II, acetyl-lysine(ε-azide)-amide) has also been designed and prepared; it has been used in a subsequent click chemistry reaction with the pentinyl moiety to transform the nitrile group into a triazolyl ring, thus removing the triple bond resonating at 2100 cm^{-1} and generating the compound III, which is 1-α-Acetyl-ε-lysinylamide-4-butylcarboxy-α-cysteinylamide triazole. This last compound has been generated because the SEIRA resonant effect did not show up with the compound I, as it can be seen in Fig. 3.9 (blue curve).

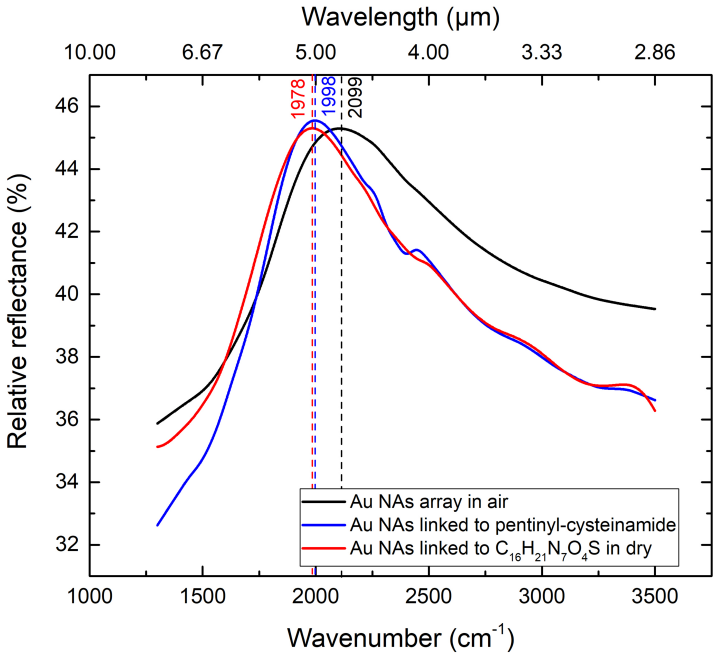


Figure 3.9. Reflectance curves of naked Au NAs (black curve), Au NAs linked to compound I (blue curve), Au NAs linked to compound III (red curve).

Indeed, SEIRA resonant effect may not appear even if the NAs have been properly designed and fabricated. This may be due to different reasons, like quantum effects [170] and/or damping and surface effects originating from impurities that hinder adsorption of the molecules of interest at the site of the plasmonic enhancement [171]. In the compound I case, the main reason can be attributed to the small molecular weight of the molecule, since it results to be 233 Da. However, the plasmonic resonance peak is red shifted of 100 cm^{-1}. This shift originates from the LSPR sensing of the RI change of the surrounding medium caused by the adsorbed compound. Although less performing than Surface Plasmon Polaritons

(SPP), LSPR-based sensors can perform well in some instances, particularly for the detection of small number of biomolecules with small molecular weight <500 Da. In this case, reported sensitivity for LSPR sensors are $\sim 2{\cdot}10^2$ nm/RIU [172]. Since the difference between the refractive index of the air and compound I is 0.42 [173], a sensitivity of 600 nm/RIU can be calculated for a concentration lower than 2 fmol, in accordance with the values reported for similar molecular systems.

In order to further probe the sensing capabilities of the L = 850 nm structure, the compound III has been linked to the NAs array through a click chemistry reaction with compound II. After the formation of the triazole moiety in compound III, a further 20 cm^{-1} red shift has been observed (Fig. 3.9, red curve) compared to the compound I resonance (Fig. 3.9, blue curve), showing the sensing capabilities of the fabricated devices for small molecules probing, since compound III has a molecular weight that is comparable to compound I. Moreover, the manufactured devices have shown an excellent reproducibility and an excellent robustness. Indeed, they have been recycled using a liquid-phase hydrogen peroxide-mediated UV photo oxidation process for regenerating the naked gold surface [174], ensuring that the devices performances suffer no degradation, as it has been shown in Fig. 3.10.

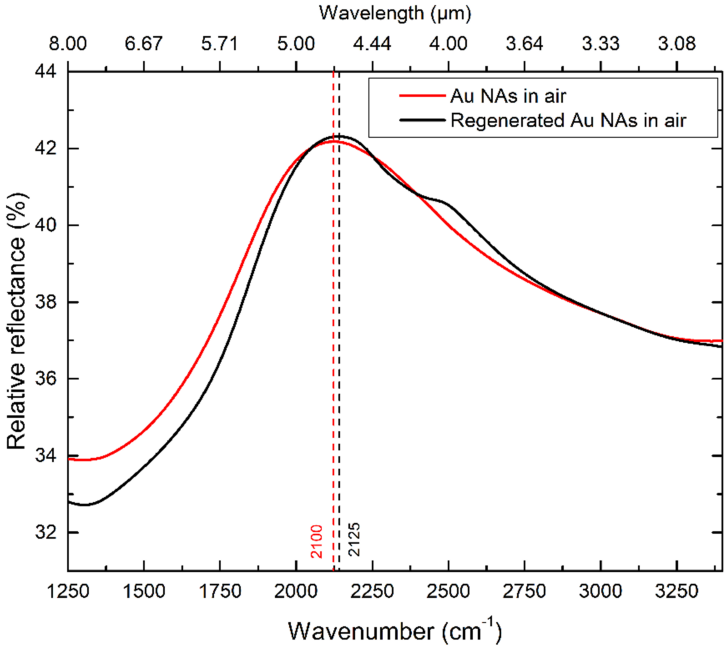


Figure 3.10. Reflection curves of the L = 850 nm device before the experiment described in Sec. 3.1.3 for the sensing of small molecules (red curve) and after the regeneration process described in [174].

3.1.3.2 Large molecules sensing

To test the SEIRA resonant effect at wavenumbers where the C=O groups are detected, a thin layer of high molecular weight PMMA (950 kDa) containing a high density of repeating C=O units has been deposited on the NAs array with arm length L = 1100 nm. A thickness value of 50 nm has been chosen to fully cover

the NA, since the device covering with too thick layers would hamper the SEIRA signal [175]. In Fig. 3.11, the SEIRA spectra recorded on a 25 mm^2 area of NAs arrays before and after the PMMA deposition are shown.

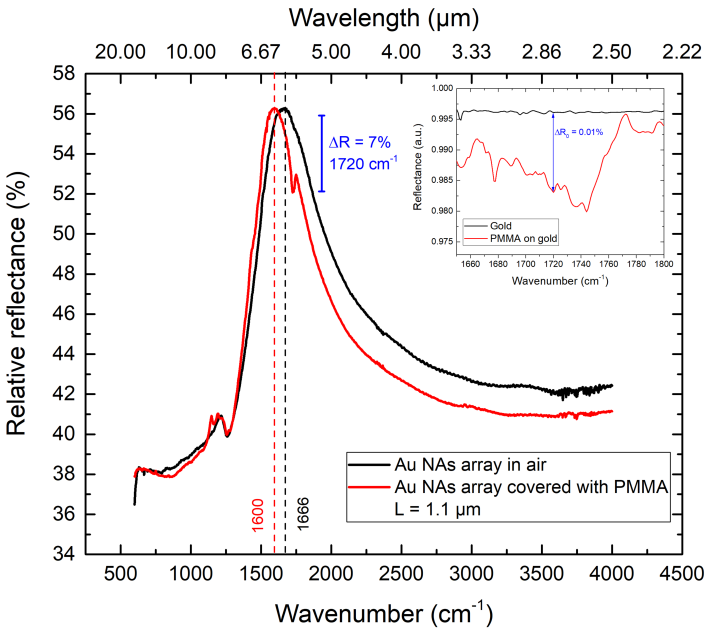


Figure 3.11. Reflectance curve of the gold NAs array in air (black curve) and of the gold NAs array covered with a 50 nm PMMA layer (red curve). In the inset, the reflectance curve of a bulk gold film deposited on the same substrate (black curve) and of the gold film covered with a 50 nm PMMA layer (red curve).

After PMMA deposition, the peak position of the plasmonic resonance is red-shifted by 66 cm^{-1}. Since the difference between refractive index of the air and PMMA is 0.49 [176], a sensitivity of 505 nm/RIU can be found for the developed device. Moreover, resonant coupling between the plasmonic NAs resonance and carbonyl C=O stretching vibration is found in the measured spectra at 1720 cm^{-1}, in good agreement with data reported for PMMA. The good match of the antenna's resonance with the C=O stretching vibration band is crucial for the appearance of the vibrational signal. The signal intensity, calculated as difference between maximum and minimum reflectance at the vibrational feature, reaches a value of about 2%.

An enhancement factor (EF) parameter has been defined and calculated to quantify the sensitivity of SEIRA resonant effect. This parameter correlates the enhanced signal strengths to the standard IR reflection measurements as follows [158, 177]:

$$EF = \frac{\Delta R}{\Delta R_0} \cdot \frac{A_0}{A_{SEIRA}} \tag{3.1}$$

where ΔR is the percentage variation between the reflectance curves of the NAs array with and without the PMMA layer evaluated in correspondence of the vibrational signature (where it results to be $\sim 7\%$) and ΔR_0 is the percentage variation between

the reflectance curves of a smooth gold surface deposited on a similar silicon substrate with and without the same PMMA layer (at the vibrational signature it results to be $\sim 0.01\%$, as shown into the inset of Fig. 3.11) [169]. This first term in Eq. 3.1 represents a gain factor due to the signal enhancement, while the second term represents a geometrical factor, where A_0 is the reference measurement area, while A_{SEIRA} is the active area filled with molecules. Specifically, the active area for the enhancement of SEIRA signal mainly originates from the molecules located in the antenna hot-spots, in our case the tip ends of the antenna, as it has been evaluated from the plots of the electric field intensity distribution on the NAs shown in Fig. 3.12.

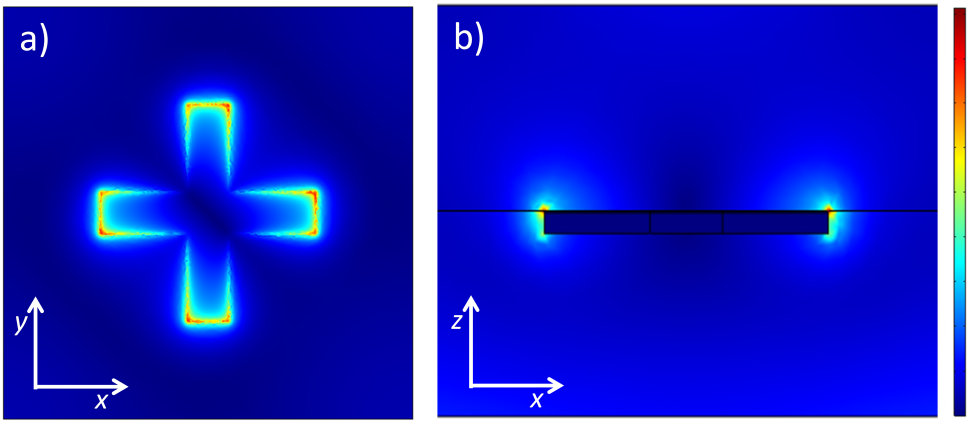


Figure 3.12. 2D plots of the electric field intensity distribution on the NA unit cell. (a) Electric field intensity distribution taken at 20 nm above the NA unit cell surface on the xy-plane perpendicular to the z-direction of the impinging EM radiation. (b) Electric field intensity distribution on the xz-plane corresponding to the NA unit cell cross section view. The cross dimensions are not in scale.

On the basis of this finding, a commonly used approximation for the active area is the surface of the tip ends [157], that has been approximated by excess to a semicircle whose radius is ≈ 100 nm. Considering that the reference measurement area is 200 µm x 200 µm and that 10^4 crosses fall into this area, a geometrical factor ≈ 64 multiplies a gain factor of ~ 700, leading to an EF ≈ 45000. Typical enhancement factors found in other studies range from 1000 to 100000 depending on the antenna shape, material, and arrangement [158]. The value found for the EF parameter confirms the goodness of the manufactured device and of the model used for its design; moreover, this device shows the capability to perform both refractive index sensing and surface-enhanced infrared absorption spectroscopy.

3.1.4 Conclusions and future perspective

In conclusion, high-density arrays of gold cross-shaped NAs are very suitable for both sensitive surface enhanced infrared absorption spectroscopy and refractive index sensing. In presence of a layer of PMMA that contains repeated carbonyl groups, the SEIRA enhancement has been found to be as high as 45000 relative to the absorption peak at 1720 cm^{-1}, arising from C=O stretching. For small

molecules with a size below 500 Da (compound I), a sensitivity of 600 nm/RIU has been found for amounts of immobilized compound as low as 2 fmol or less. By increasing the NA length and hence decreasing its resonance frequency, the plasmonic near-field intensity increases [178], therefore a higher SEIRA enhancement is expected, suggesting a huge potential for the use of plasmonic enhancement in THz spectroscopy. The SEIRA enhancement may be further improved by a careful design to reduce the radiative plasmonic losses provided by the specific NA shapes and arrangements [179] and the non-radiative plasmonic losses given by the NA materials [180], that can be chosen in order to be fully compatible with standard CMOS technology in order to implement the desirable integration of opto-plasmonic sensors on silicon substrates [28]. Such optimized NAs are likely to serve as substrates for surface-enhanced infrared spectroscopy with very high sensitivity, with the capability for label-free and non-destructive material identification and for monitoring at qualitative level chemical transformations occurring at the sensor surface. Moreover, combinations of resonant SEIRA with refractive index sensing and other field-enhanced techniques, can lead to the design of nanoscale sensing platforms providing complementary chemical information and quantitative assessment of known analytes following proper calibrations with suitable standards.

3.2 Silicon-based dielectric metasurface for all-optical switching

Another developed device has been a silicon-based dielectric metasurface for all-optical switching in telecommunication applications. In the last decades, the advances in nanotechnology enabled the development of metamaterials, that are engineered media, usually constituted of periodically arranged unit elements, whose optical properties can be designed in order to tune their interaction with the electromagnetic waves in the desired manner [181]. The initial researches proposed metamaterial based on plasmonic resonances due to their capability to tailor the flow of light at the nanoscale [182]; unfortunately, the performances of this kind of metamaterials are strongly limited by the high ohmic losses occurring in metals in the visible and near-IR spectrum. For this reason, great efforts have been made to obtain similar engineered responses by using high refractive index dielectric materials as building blocks able to engineer light propagation without the coupling with plasmons [183]; these material are indeed able to provide both electric and magnetic responses while having low losses and being almost completely transparent in optical communication range. At the same time, one of the main challenges in nowadays nanophotonics is the opportunity to actively tune the optical response of the device with very short response times. For example, by using liquid crystal active layers, it has been possible to control the light direction with switching time of $\sim$ 100 µs [184]. At present, however, the optical systems work with switching times of the order of ns, requiring therefore low-power and ultrafast optically controlled nanocomponents. A potential solution to this issue is the use of phase change materials (PCM), that possess at least two stable phases (an amorphous and one or even more crystal phase) with different physical properties, like electrical conductivity, optical reflectivity, or thermal conductivity [185]. The possibility to quickly switch between these phases

allows to change the optical properties of the structures put in contact with these materials in a non-volatile and at the same time reversible way. Among all the possible PCMs, the attention has been focused on the chalcogenide glasses, that are highly non-linear materials able to switch between crystalline and amorphous phase upon a heat stimulus, resulting therefore very useful for all-optical switching applications [186]. As an example, the most investigated and used PCM, $Ge_2Sb_2Te_5$ (GST), has been long used for phase change memory applications due to its fast recrystallization time (lower than 20 ns) and the stability of its phases at room temperature [187], whose switch can be activated by optical, thermal or electrical effects over a great number of cycles (10^6). Moreover, metamaterials could also improve the switching performance of PCM by lowering the power and shortening the time needed for the phase change to take place [188]. For this reason, the device proposed in this work thesis has been designed in order to bring together the advantages of using all-dielectric metamaterials, providing the resonant behaviour, with the tuning of their optical response by covering them with a thin layer of PCM. In particular, nanorod-based metamaterials supporting dipole-like collective resonances have been covered with a germanium telluride (GeTe) active layer. Switching of GeTe from amorphous to crystalline leads to a rather high, resonance-governed reflection contrast at 1.55 µm, which makes this device a promising perspective for all-optical switching applications.

3.2.1 Numerical simulations

Thanks to a collaboration with prof. Concita Sibilia (University of Rome "La Sapienza") and her research group, a metamaterial able to mimic the effect of electromagnetically-induced transparency (EIT) has been designed, where a narrow transparency window appears within a wide absorption spectrum [189]. Thanks to the coupling of bright modes (i.e. directly excited by the impinging light) and dark modes (i.e. not coupled to the incoming light) nanoresonators, a sharp transmission peak can appear at telecommunication wavelengths, as shown in Fig. 3.13 for a metamaterial constituted by silicon nanorods and nanosquares deposited on a Silicon-on-Insulator (SOI) substrate [190].

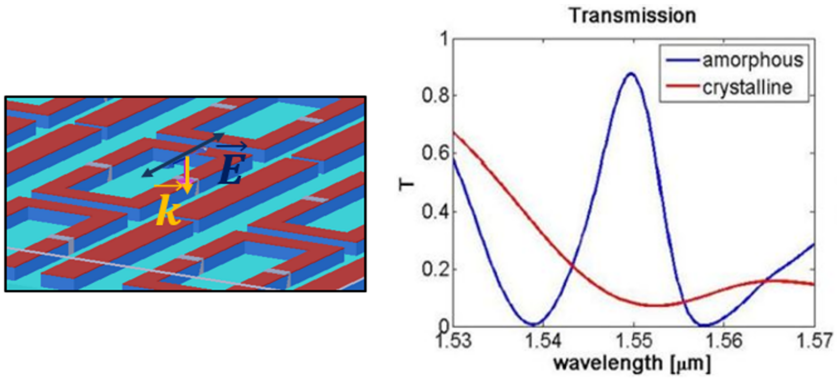


Figure 3.13. On the left, schematization of the designed metamaterial. On the right, the transmission spectrum changes between the amorphous (blue curve) and crystalline (red curve) states of the PMC layer [191].

The nanoresonators dimensions determine the spectral position of the transmission peak, while their coverage with a PCM can lead to a resonance shift that brings the transmission minimum at the position of the maximum of the previous phase. Due to its high adhesion to Si substrate and the tight control on its stoichiometry [192], GeTe has been chosen as the active layer for the design and fabrication of the proposed device [193]; indeed, its two phases (amorphous and crystalline) are stable at room temperature and allow to switch between them by ns optical pulses.

In order to explore the thermal stability and cyclability of these hybridized nanostructures, the experimental work has investigated a simpler configuration, i.e. a 2D periodical array of nanorods, where a dipole collective resonance can be excited. The numerical simulations have been carried out with Finite Difference Time Domain (FDTD) software Lumerical. The metamaterial is excited by a plane wave linearly polarized along the nanorod x direction, under normal incidence; periodic boundary conditions (PBC) have been applied in the metamaterial xy plane, while in the incident wavevector direction (z-direction) a perfectly matched layer (PML) condition has been considered. In particular, the nanoresonators geometrical parameters optimization procedure has been carried out in order to maximize the contrast ratio (CR) of the device, defined as the ratio between the transmitted power evaluated in the amorphous and in the crystalline state of the PCM layer. In particular, in Fig. 3.14, p is the metamaterial's period, W is the nanorod width, L is the nanorod length, t is the nanorod thickness, t_{GeTe} is the germanium telluride thickness and t_{SiO_2} is the buried oxide layer thickness.

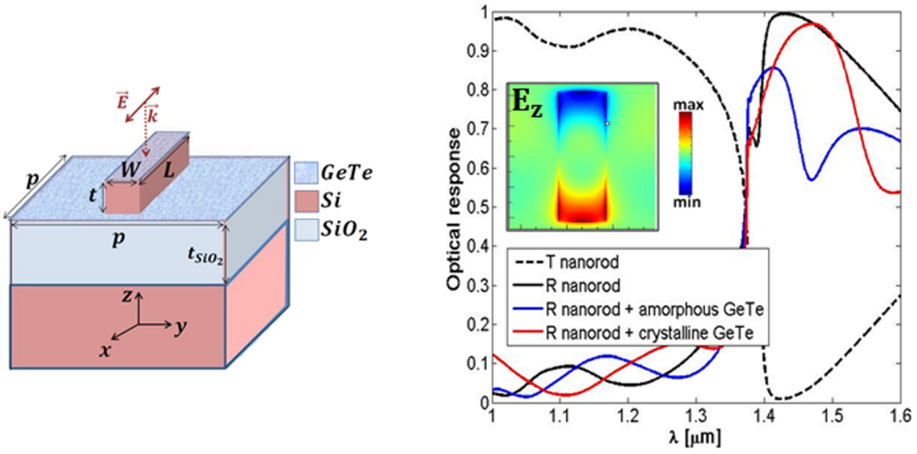


Figure 3.14. On the left, the schematization of the unit cell used for the numerical simulation. On the right, the optical response of the nanorod metamaterial with and without GeTe. Inset: z-component of the electric field at the dipole-like resonance.

The numerical results shown in the right side of Fig. 3.14 are referred to an optimized structure whose geometrical parameters are summarized in Table 3.1:

Table 3.1. Metamaterial geometrical parameters.

p	L	W	t	t_{SiO_2}	t_{GeTe}
950 nm	840 nm	300 nm	220 nm	3000 nm	30 nm

As it can be seen, the Si nanorod with previously mentioned dimensions provides a broad reflection peak in the near-infrared (black curve). The same nanorod, with 30 nm amorphous GeTe on the top, has slightly blue-shifted resonance (blue curve) and a lower reflection peak due to GeTe losses. Changing the GeTe phase from amorphous to crystalline produces a red-shift of the resonance and an increase of the reflectivity (red curve). This red shift is due to the notably higher refractive index of GeTe in the crystalline state, as it can be seen in Fig. 3.15, which can lead to high optical contrast ratio between the resonance in the amorphous state and the off-resonant behaviour in the crystalline state.

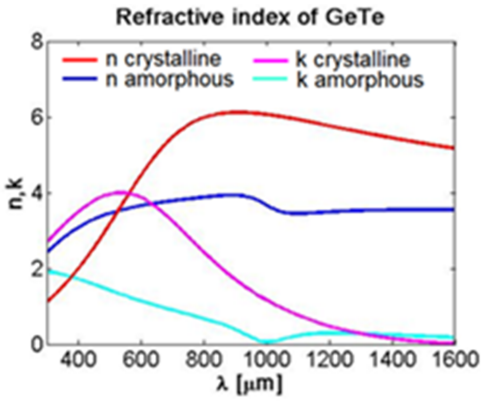


Figure 3.15. GeTe refractive index [193].

The designed device has been fabricated on SOI substrate by means of Electron Beam Lithography (EBL) and Reactive Ion Etching (RIE), as it will be better explained in the following subsection.

3.2.2 Fabrication process

A homogeneous 2D nanorod array has been fabricated on 100 µm x 100 µm area by Electron Beam Lithography in a single write field size, avoiding therefore the stitching errors that arise when multiple write fields are used. In Fig. 3.16 the fabrication flow chart is shown.

In detail, it consists of the following steps:

- deposition, via spin coating, of $\sim$ 90 nm thick PMMA film;
- PMMA exposure by means of Electron Beam Lithography;
- PMMA development in 1:3 MIBK to IPA developer solution for $\sim$ 30 s;
- deposition, by sputtering, of 20 nm-thick chromium (Cr) layer;
- lift-off process;
- RIE process;
- Cr mask residual wet etching in Cr 18 Etch solution;
- deposition, by RF sputtering, of 30 nm-thick GeTe film.

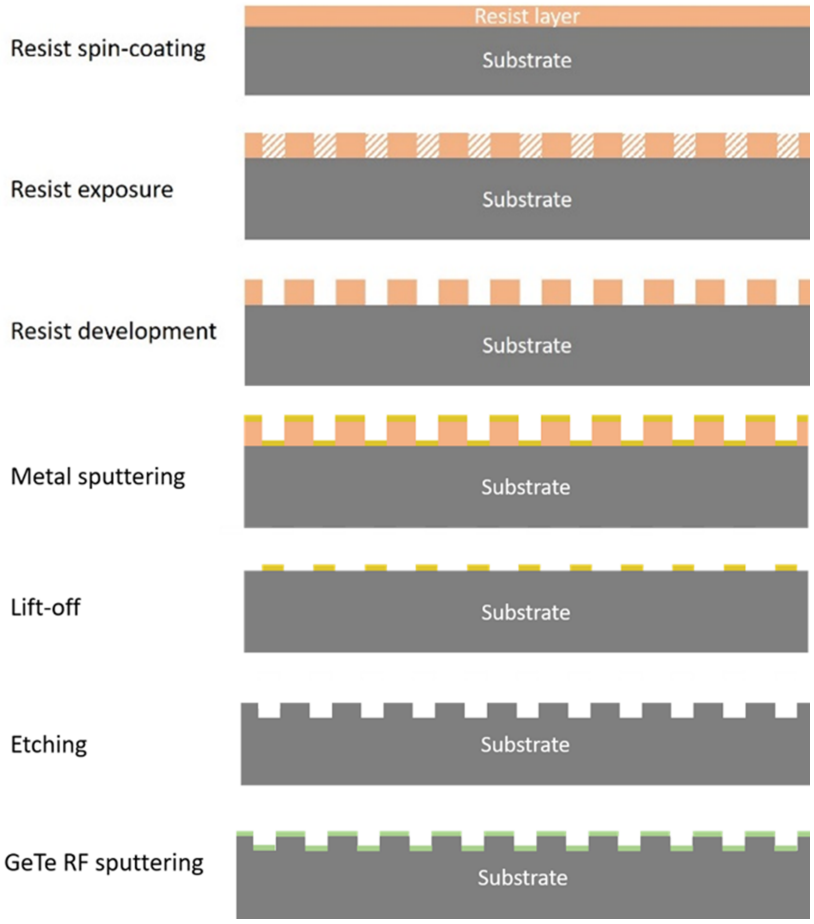


Figure 3.16. Nanorod fabrication flow chart.

All of the fabrication steps have been performed into the laboratories of the Unit of Naples of CNR - IMM, except for the GeTe RF sputtering deposition, which, instead, has been carried out into the laboratory of the Unit of Catania of CNR - IMM thanks to a collaboration with prof. Maria Miritello. The use of a metallic mask for RIE process is due to the poor PMMA resistance to etching processes [194]; since the etching rate of metals is very low respect to the silicon etching rate, a thin mask can sustain the whole etching process. In order to accomplish the lift-off process to obtain the 20 nm-thick Cr mask, a low-energy lithography has been performed on a thin PMMA layer with an acceleration voltage of 10 kV, a numerical aperture of 10 µm, a dose of 100 µC/cm^2 and a step size of 10 nm. After the resist development, the lift-off process has been carried out with the same procedure described in Sect. 3.1.2. A first metrology analysis of the device has been performed, since a proximity effect correction has been executed due to the high-density pattern impressed into the resist layer. In Fig. 3.17 the recorded SEM images are shown. In particular, despite a negative pattern biasing has been performed (with L = 780 nm and W = 200 nm dimensions imposed rather than 840 nm and 300 nm, respectively), the Cr mask dimensions are bigger than those presented in Table 3.1 due to the proximity effect.

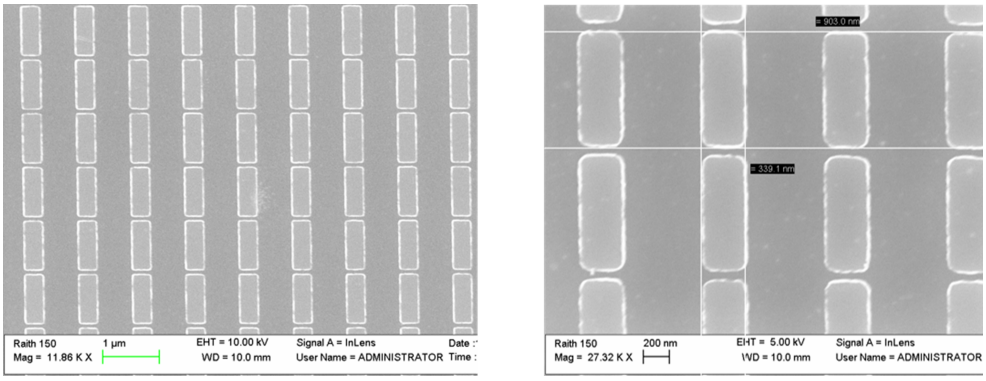


Figure 3.17. SEM images of the Cr mask before the RIE process.

However, the bigger mask dimensions (L = 900 nm, W = 340 nm) are helpful for the RIE process: due to its non-perfect anisotropy, indeed, a lateral etching occurs together with the vertical one, causing the shrinking of the nanorod dimensions. In order to limit such effect, an optimization of the RIE process parameters has been performed; such parameters are summarized in Table 3.2 for a process carried out in an Oxford Plasmalab 80 Plus RIE system with a CF_4+O_2 gas mixture.

Table 3.2. RIE process parameters for nanorods fabrication.

RF Power	Bias voltage	Working pressure	CF_4 flow rate	O_2 flow rate	Etching time
300 W	730 V	$1.0{\cdot}10^{-1}$ mbar	50 sccm	2 sccm	1:00 min

Using the parameters summarized in Table 3.2, a chromium etching rate of 0.14 nm/s has been found while, for silicon, the etching rate results to be 3.67 nm/s.

After the mask residual removal (through a wet etching in Cr Etch 18 solution for 5:00 minutes followed by the substrate rinsing in DI water and drying under N_2 flux), another SEM metrology analysis has been performed to verify the final device dimensions. In Fig. 3.18 the SEM images are shown; in particular, it is possible to note that the nanorod dimensions are slightly bigger than that reported in Table 3.1, but are still in the limit of 10% fabrication tolerance, that is considered a good fabrication result.

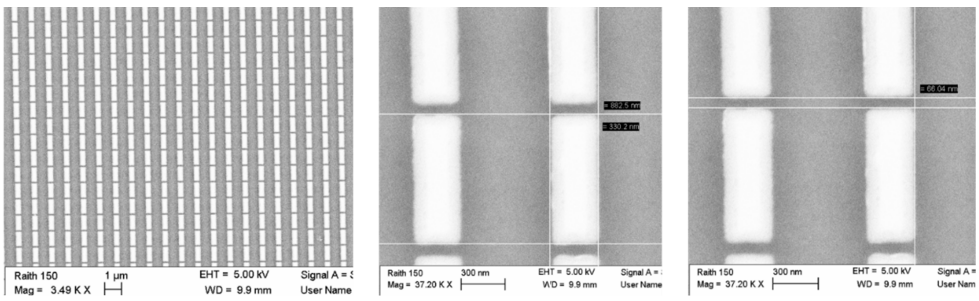


Figure 3.18. SEM images of the Si nanorod on SOI substrate after the RIE process. On the left, an overview of the patterned area. The central image shows the nanorod dimensions, while on the right the smallest gap between two adjacent nanorod has been measured.

The etching depth has been verified with an AFM analysis, whose results are shown in Fig. 3.19. Nanorods appear attached to each other, but this effect is due to the AFM tip dimension and to the small gap within two adjacent nanorod, which avoids the tip to enter. From Fig. 3.18 it is indeed possible to see that the nanorods are clearly separated by a 66 nm gap.

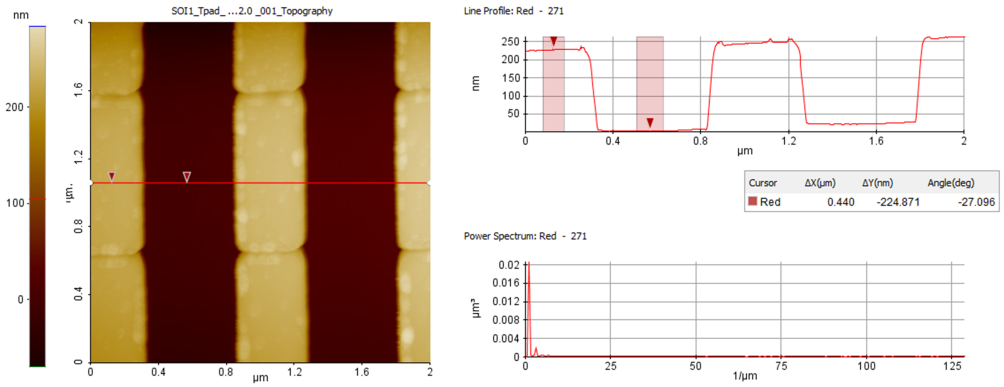


Figure 3.19. AFM analysis of the fabricated device before GeTe deposition. Due to the small gap between the nanorods and the tip dimensions, the nanorods appear attached to each other.

Once the nanorods have been defined into the SOI substrate, the device was sent to Unit of Catania of CNR – IMM for the RF sputtering of 30 nm amorphous GeTe layer [193], being then ready for the optical characterization, which will be detailed explained in the next subsection.

3.2.3 Device characterization

The fabricated metamaterial has been characterized in reflection geometry into the Nonlinear Photonics Laboratory of University of Rome "La Sapienza". In particular, reflection measurements have been carried out at two different wavelengths, i.e. 1.3 µm and 1.5 µm. First measurements were done by scanning the metamaterial covered by the GeTe layer in the amorphous phase. Then, the whole structure was slowly heated above the crystallization temperature (200 °C), and the reflection scan was repeated. A sketch of the measurement setup is shown in Fig. 3.20.

A Quartz Tungsten Halogen (QTH) lamp and microscope are used to position the laser in correspondence of the patterned area of the sample, observed by a Charge-Coupled Device (CCD) camera. The reflection signal is recorded with a Ge photo-diode (which replaces the QTH lamp) by exciting the resonant structure with a laser light polarized in x-direction, under normal incidence, with a spot size of $\sim$ 15 µm. In addition, the device is put on a movable stage which allows to scan the sample position with a scan step of 2 µm, in order to perform reflection measurements of both patterned and non-patterned areas of the device. In the non-patterned zones, at both wavelengths the thin crystalline layer is highly reflective, as expected. When entering the metamaterial zone (positioned at the centre of the grid shown in Fig. 3.21), the GeTe losses cause a lowering of the reflection coefficient in all cases, except for the amorphous GeTe at 1.5 µm, where an increase of this coefficient is reported. Moreover, as the laser position approaches the central zone

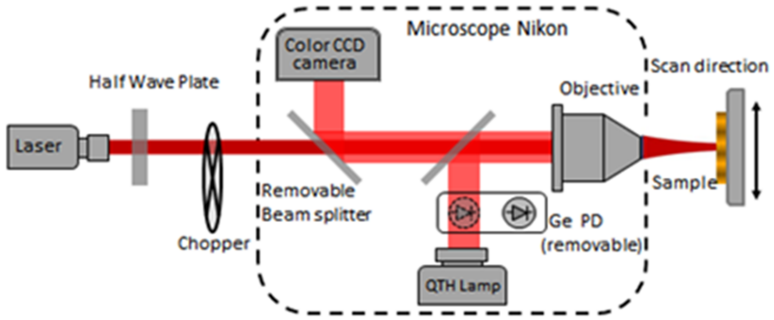


Figure 3.20. Sketch of the measurement setup of the reflection from SOI-GeTe hybrid metamaterial versus laser beam position.

of the metamaterial, there is a further increase of the reflection coefficient. This effect is due to the contribution of the collective resonant response, which reaches its maximum into the centre of the patterned area [195], thus leading to the noticeable reflection contrast between metamaterial covered by amorphous and crystalline GeTe at 1.5 µm. Indeed, a CR of 5 can be observed for the proposed structure, in accordance to the state-of-art works [196]. These results are shown in Fig. 3.21.

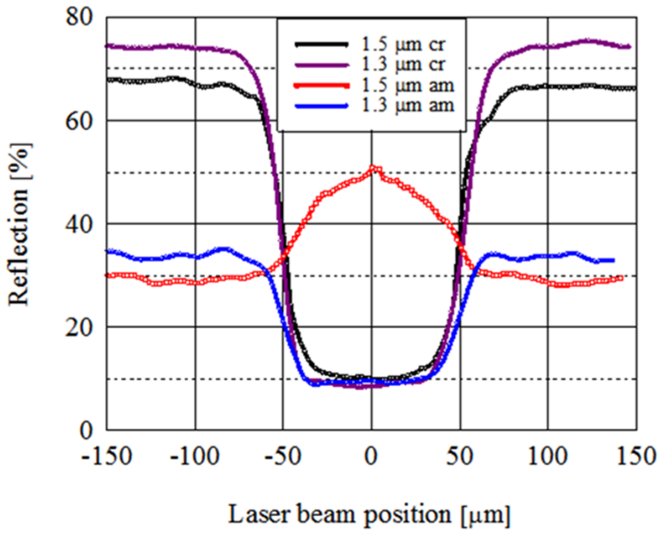


Figure 3.21. Reflection measurement of the GeTe/SOI hybrid structure in dependence of the laser position (the sample is positioned between –50 µm and +50 µm) conducted at 1.3 µm for the amorphous (blue curve) and crystalline state (purple curve) of the GeTe layer. The same measurements have been performed at 1.5 µm for the amorphous (red curve) and crystalline (black curve) of the GeTe layer.

The phase change of the GeTe layers on the patterned surface has been confirmed by micro-Raman confocal microscopy measurements performed at 632 nm in reflection geometry. First, the Raman response of unpatterned GeTe layers has been recorded in the non-patterned zones of the structure. The results are shown in Fig. 3.22a before (red curve), and after (blue curve) the heating, corresponding to the amorphous and

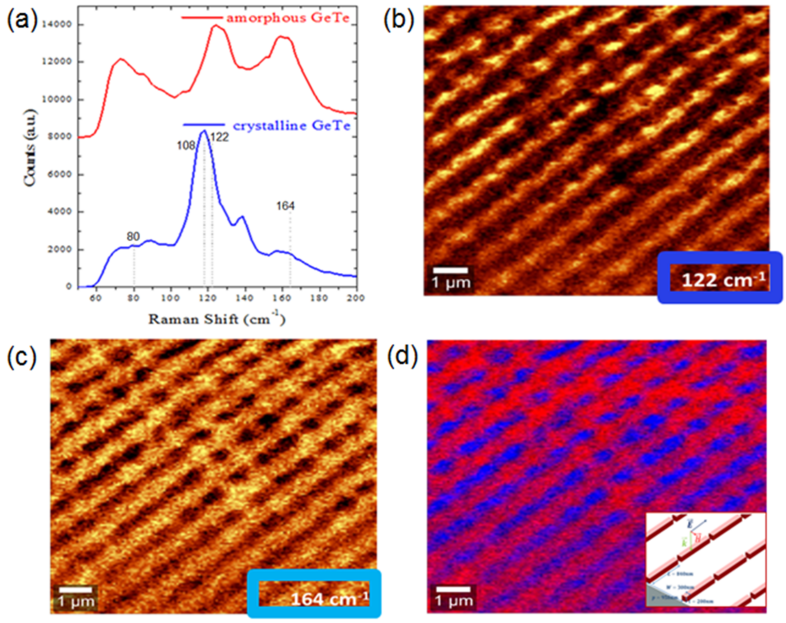


Figure 3.22. (a) Raman spectra for the amorphous and crystalline flat layers of GeTe upon SOI, in the non-patterned part of the structure. (b) Raman map from the hybrid metamaterial of the signal at 122 cm^{-1} and (c) at 164 cm^{-1}. (d) False-color combination image of the Raman maps from the hybrid metamaterial of the signals at 164 cm^{-1} (red), and at 122 cm^{-1} (blue).

crystalline phase, respectively.

In the range 50-200 cm^{-1} three bands can be distinguished, peaked respectively around 80 cm^{-1}, 122 cm^{-1} and 164 cm^{-1}, accordingly to what reported in literature [197]. In the amorphous phase, the 164 cm^{-1} peaked band appears more prominent with respect the crystalline phase, where the 122 cm^{-1} is the more intense. Moreover, all the bands appear blue-shifted in the amorphous case with respect to the crystalline phase. Then, the Raman response from the hybrid GeTe/SOI metamaterial have been recorded and reported as a color map, for 122 cm^{-1} and 164 cm^{-1} bands, in Fig. 3.22b and Fig. 3.22c respectively. The Raman signals are strongly dependent on the position: in particular, on the top of the nanorods the signal at 122 cm^{-1} reaches its maximum, while it has its minimum in the zones between the nanorods, where instead the maximum Raman signal at 164 cm^{-1} is maximized. This means that there is a prevalence of the signal relative to crystalline GeTe on the top of the nanorods and of the signal relative to the amorphous GeTe in the zone between the nanorods. The structure of the GeTe film above the nanorods and at the bottom is therefore different, with an amount of crystal at the bottom that is lower than that above the nanorods. Such a behavior can be ascribed to the different strain suffered by the film on top of the nanorods with respect to that at the bottom. These observations are confirmed in Fig. 3.22d, where the false-color combination image, obtained by Witec Project 4.0 software, is reported. This image combines the Raman maps of the signals at 122 cm^{-1} and at 164 cm^{-1}; in particular the red regions are referred to the prevalence of the amorphous GeTe (164 cm^{-1} signal) and the blue region refers to the prevalence of crystalline GeTe

(122 cm^{-1} signal).

These results suggest that designing metamaterials governed by the control of PCM only on the top of nanoresonator offers great promise for the low-power, optically induced phase change, where only a small volume of GeTe must be switched in order to change the overall metamaterial response. The next steps in developing this kind of device should be therefore the definition of a GeTe/SOI structure where the GeTe layer is deposited on the SOI substrate before its patterning, in order to achieve a final device where the GeTe layer lies only on top of the Si nanorods.

3.2.4 Conclusions and future perspectives

The deposition of PCM thin layers on Si nanoresonators allows to actively tune their optical response. A near-infrared reflection switching metamaterial, based on a hybrid PCM GeTe/SOI nanostructure, has been proposed. GeTe phases (amorphous and crystalline) indeed shows high refractive index contrast and low losses in the near-infrared region of the spectrum; moreover, its room temperature stable phases allow to switch between them by ns optical pulses over large number of cycles, making it a very suitable choice for switching application. The fabricated device, constituted by a 30 nm thin GeTe layer deposited on top of a metamaterial constituted by Si nanorods fabricated on SOI substrate, shows a high contrast ratio (~ 5) at 1.5 µm when a thermally induced phase change occurs in GeTe layer, being therefore of great interest for the tunable, all-dielectric nanophotonics, implementable in SOI technology.

The thermally induced phase change is the first step for the characterization of SOI-GeTe hybrid metamaterial approach; in the future, optical switching achieved by laser pumping could provide fast, non-volatile and reconfigurable reflection switches, while the patterning of the whole structure after the GeTe deposition (in order to switch only little amounts of GeTe) could lead to sharper resonances providing even higher contrast ratio. These novel approaches, indeed, could lead to noticeable advances in silicon-based nanophotonic applications, especially in the telecommunication field, where the optical switching would constitute a milestone for the development of fully integrated electrical and optical components on silicon chips.

3.3 Silicon based dielectric grating as interconnect device

Finally, the research work conducted during this thesis work has been aimed to the design and fabrication of a silicon based integrated device for an in-plane non-mechanical steering of light, given the increasing need of devices able to redirect the flow of light for the inter- and intra-chip interconnections.

For many years, the state-of-art beam steering devices has been based on mechanical approaches, where the deviation of light propagation was achieved by applying a force to an actuator to cause a displacement of the optical component, which, in turn, changes the beam direction. An example of this kind of beam steering devices is constituted by the Micro Electro-Mechanical System (MEMS) mirrors,

which consist of a mirror placed on an actuator: when an electric force is applied to the actuator, a displacement or a tilt of the mirror occur [86], enabling $\sim$ 200 µrad scanning range with 8 ms scanning time. However, the actuator vibrations limit the system's resolution and, in addition, continuous maintenance is required. An alternative to a MEMS mirror is the rotating Risley prism, where the mirror is replaced by a pair or even more prisms and the actuator is replaced by a rotatory motor [198]. For each prism is required a dedicated motor, since a change of the prism angle induces a change of the angular displacement of the beam, which in turn depends on the prism's refractive index, its angle and the angle of incidence. The main limitation of this kind of beam steering device is its inability to move a beam in a straight line due to the prism dispersion; in addition, they require high-cost and complex-control systems, and also a routine maintenance.

Since the mechanical beam steering systems require the movement of some components to steer the light, their fundamental limitation will always be the continuous maintenance required for the correct operation of the moving parts. For this reason, the research efforts have been moved toward the development of non-mechanical beam steering systems, since they result to be cheaper, lighter, more compact and with faster response time compared to their mechanical counterpart. Early stage researches were focused on the electro-optic effect offered by some materials, like lithium niobate [199], but they don't allow to steer light at large angle, as well as devices based on array of waveguides [200]. For this reason, most of the non-mechanical beam steering devices proposed so far have been based on liquid crystal (LC) technologies, since they show high birefringence that allow to steer light by creating a large difference of the light optical path by applying modest voltages [201]. A typical LC beam steering device is usually made of a LC phase array with a variable period approaching a sawtooth phase profile [202] or of polarization gratings (LCPGs) that can generate a phase shift of the beam by using a polarization rotation instead than a variation of the optical path [87].

In the last decades, the development of nanofabrication techniques has enabled the physical realization of photonic crystals (PhC). These advances allow to exploit the extraordinary capabilities of PhC in controlling the propagation of light; in particular, thanks to the superprism effect, a new concept of beam steering devices has been introduced. This effect, indeed, refers to the drastic wide swing suffered by a light path entering a PhC when a slight change of the incident light angle is provided [203]. The superprism effect, caused by the strong modification of group velocity of light, reaches its maximum in 3D PhCs, where the achievable light deflection can be up to 500 times higher than that achievable in a classic prism and more than 50 times higher than that achievable in a conventional grating [204]. However, due to the non-standard fabrication technologies often needed for the development of 3D PhCs, research efforts have turned to the development of 1D and 2D PhCs, that show superprism effect as well [205]. Indeed, even if their deflection capabilities are lower than that offered by 3D structures, their performances are still much higher than that offered by conventional prisms. For this reason, the simplest photonic crystal structure (a 1D grating) has been considered in this thesis work due to its relatively easy fabrication process. Indeed, it is possible to demonstrate that, with suitable Bragg grating condition, an analytical formula for the angular deviation of the grating can be calculated [206], as it will be shown below.

3.3.1 Distributed Bragg reflection theory applied to PhCs

PhCs are usually analyzed in analogy with the electron wave propagation in solid crystals [207]. In particular, the forbidden photonic band can be considered equivalent to the bandgap of solid crystals encountered by electrons due to the crystal periodic potential. Moreover, the electronic propagation into crystals can be treated with the Dynamical Diffraction Theory (DDT) [208]; for this reason, also the analysis of a PhC has been treated with the DDT [206]. Considering a dielectric medium with spatially varying properties, it is possible to define a dielectric coefficient $\varepsilon(\vec{r})$ and a contrast function $\chi(\vec{r})$ as:

$$\chi(\vec{r}) = 1 - \frac{\varepsilon_s}{\varepsilon(\vec{r})} \tag{3.2}$$

where ε_s is the dielectric constant background value.

From Maxwell equations, it follows that the propagation inside this medium is regulated by Eq. 3.3:

$$\nabla^2\vec{D} + \nabla\times\nabla\times(\chi\vec{D}) + \omega^2\mu_0\varepsilon_s\vec{D} = 0 \tag{3.3}$$

where μ_0 is the vacuum magnetic permeability. Moreover, a time-harmonic dependence with frequency ω is supposed.

A wave in the form:

$$\vec{D}(\vec{r}) = \sum_h \vec{D}_h e^{2\pi i\vec{k}_h\cdot\vec{r}} \tag{3.4}$$

can be considered as a general solution of Eq. 3.3 with a periodic function χ given by:

$$\chi(\vec{r}) = \sum_h \chi_h e^{2\pi i\vec{h}\cdot\vec{r}} \tag{3.5}$$

where the sum is extended over all the periodicity of the crystal.

By substituting Eq. 3.5 and Eq. 3.4 into Maxwell Eq. 3.3, each component of Eq. 3.4 is given by:

$$\vec{D}_h = \frac{1}{k_h^2 - k_s^2}\sum_{h'}\chi_{h-h'}(\vec{k}_h\times\vec{k}_h\times\vec{D}_{h'}) \tag{3.6}$$

where $k_s = \omega\sqrt{\mu_0\varepsilon_s}$ is the background wavenumber.

The wave vector into the structure can be expressed as [206]:

$$\vec{k}_0 = \vec{k}_B + \vec{\delta} \tag{3.7}$$

where $\vec{k}_0$ is a generic origin vector, $\vec{\delta}$ is an unknown displacement while $\vec{k}_B$ is a vector satisfying the Bragg law, that for a general reciprocal lattice vector $\vec{h}$ can be expressed as:

$$\vec{k}_B\cdot\vec{h} = -h^2/2 \tag{3.8}$$

By looking for vectors close to the Bragg condition, it is possible to consider δ small enough respect to $\vec{k}_B$, therefore the term δ^2 can be neglected into the dispersion equation:

$$\begin{aligned} k_0^2 &= k_B^2 + 2X_0 \\ k_h^2 &= k_B^2 + 2X_h \end{aligned} \tag{3.9}$$

where $h^2 + 2\vec{k}_B \cdot \vec{h} = 0$ (from Eq. 3.8) and

$$\begin{aligned} X_0 &= \vec{k}_B \cdot \vec{\delta} \\ X_h &= (\vec{k}_B + \vec{h}) \cdot \vec{\delta} \end{aligned} \tag{3.10}$$

By substituting Eq. 3.10 into Eq. 3.9, the dispersion equation becomes:

$$\begin{aligned} 4X_0X_h(\chi_p^2 - \chi_h\chi_{-h}) + 2(X_0 + X_h)[\chi_p(k_B^2\chi_p - k_s^2) + \\ -\chi_h\chi_{-h}k_B^2] + (k_B^2\chi_p - k_s^2)^2 - \chi_h\chi_{-h}k_B^4 = 0 \end{aligned} \tag{3.11}$$

where $\chi_p = 1 - \chi_0$.

Equation 3.11 gives all the wavevectors compatibles with the periodic structure of an unlimited crystal. Anyway, to determine which wavevector is effectively excited into the grating, it is necessary to consider at least a semi-infinite crystal with the appropriate boundary conditions by specifying the position of the vector $\vec{h}$ respect to the normal $\vec{n}$ to the surface. Since the superprism effect is related to a beam transmitted into the crystal, the so-called transmission geometry has been the object of this study, considering, for simplicity, the symmetric transmission geometry, when $\vec{h}$ is orthogonal to $\vec{n}$. From Eq. 3.8, it follows that the tangential component of the wavevector satisfying Bragg condition can be expressed as:

$$k_{B_t} = -\frac{h}{2} \tag{3.12}$$

The general expression of $\vec{h}_B$ in Eq. 3.8 allows to do convenient choices for its expression, which can be helpful for simplifying dispersion equations Eq. 3.11. A possible choice from this point of view can be the following:

$$k_B^2 = \frac{k_s^2\chi_p}{\chi_p^2 - \chi_h\chi_{-h}} \tag{3.13}$$

By substituting Eq. 3.13 into Eq. 3.11, the dispersion relation can be simplified as follows:

$$\begin{aligned} X_0X_h &= \frac{\chi_h\chi_{-h}k_B^4 - \left(\frac{k_B^2\chi_h\chi_{-h}}{\chi_p}\right)^2}{4\left(\chi_p^2 - \chi_h\chi_{-h}\right)} = \\ &= \frac{\chi_h\chi_{-h}}{4\chi_p^2}k_B^4 = \frac{\chi_h\chi_{-h}}{4\left(\chi_p^2 - \chi_h\chi_{-h}\right)}k_s^4 \end{aligned} \tag{3.14}$$

In order to clarify the concepts expressed so far, a schematization of the dispersion surface deriving from Eq. 3.14 is shown in Fig. 3.23 [206].

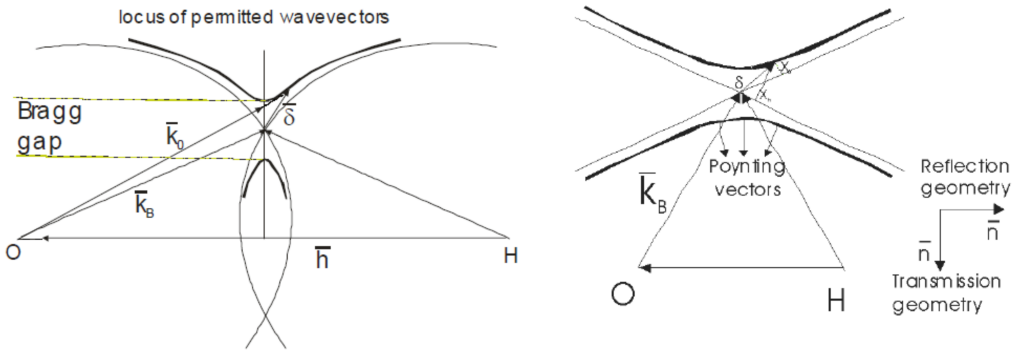


Figure 3.23. On the left, dispersion surface close to the Bragg condition for a reciprocal lattice vector $\vec{h}$. On the right, a detail close to the boundary of the Brillouin zone [206].

Equation 3.14 must be combined with the continuity conditions required for the tangential components of the wavevector, in order to ensure phase front continuity at the boundaries. If $\vec{k_i}$ is the incident wavevector, the tangential component of $\vec{\delta}$ can be defined through Eq. 3.7:

$$\delta_t = k_{B_t} - k_{i_t} \tag{3.15}$$

If a variable γ, function of the incident wave and defined as:

$$\gamma = k_{B_n}\delta_n = k_{B_n}\left(k_{B_n} - k_{i_n}\right) \tag{3.16}$$

is introduced, it is possible to express Eq. 3.10 as follows:

$$\begin{aligned} X_0 &= \gamma + \delta_t \frac{h}{2} \\ X_h &= \gamma - \delta_t \frac{h}{2} \end{aligned} \tag{3.17}$$

Using Eq. 3.17, dispersion relation 3.11 becomes:

$$\delta_t^2 = \frac{\chi_h \chi_{-h}}{\chi_p^2}\frac{k_B^4}{h^2} - \frac{4\gamma^2}{h^2} \tag{3.18}$$

where h is a constant, while the other terms are function of the wavelength $(\chi_p, \chi_h, \chi_{-h}, k_B)$ and of the incident angle (γ).

It is clear that dispersion equation 3.14 represents a hyperbola because the product $X_0 X_h$ is a frequency dependent constant; it represents therefore the so-called *Equi-Frequency Surface* (EFS), shown on the right side of Fig. 3.23. Moreover,

it is known that the direction normal to EFS represents the propagation direction of energy [209]; therefore, it can be shown that the angle α of this energy propagation, respect to the normal, is related to the Bragg angle θ_B through the following relation [210]:

$$tan\,\alpha \;=\; \frac{1-\xi^2}{1+\xi^2}\,tan\,\theta_B \tag{3.19}$$

where the slight deviation respect to the Bragg angle, $\Delta\theta$, is related to the system parameters through:

$$\begin{aligned} \xi \;&=\; \eta \pm \sqrt{\eta^2+1} \\ \eta \;&=\; \frac{\Delta\theta}{\chi_1\,sin\,2\theta_B} \end{aligned} \tag{3.20}$$

where only the first order of the diffraction grating has been considered, that is $\chi_1 = \chi_h$. By considering a 1D photonic crystal constituted by two alternating dielectric media with dielectric constant ε_1 and ε_2, whose thickness are d and a, respectively, as shown in Fig. 3.24, the following relation can be given:

$$\chi_1 \;=\; 2\frac{d}{a}\left(1-\frac{\varepsilon_1}{\varepsilon_2}\right)\,sinc\frac{d}{a} \tag{3.21}$$

The relations derived so far have been used to find the geometrical parameters of the grating which would ensure a good angular amplification, defined as the ratio $\Delta\theta_{Out}/\Delta\theta_{In}$.

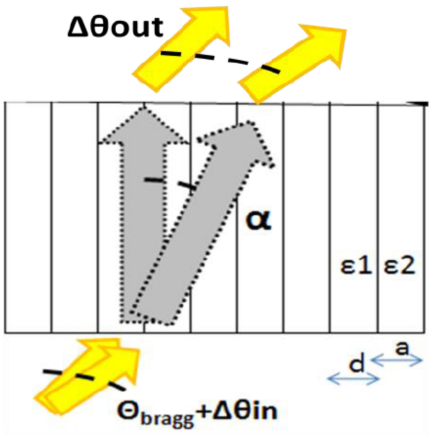


Figure 3.24. Grating parameters schematization.

In the following paragraph, the numerical results are presented together with several considerations about fabrication aspects which must always been taken into account when designing a new device.

3.3.2 Numerical simulations

Several numerical simulations have been carried out in order to find the best parameter set for a superprism-based optical beam deflector. Each of these parameters has been found calculating the α angle trend by varying just one of them at time, while the others are arbitrarily fixed. The only parameter which will remain constant during all the design process is the wavelength of operation, which has been fixed at 1.55 µm in order to develop a device working at telecommunication wavelengths.

The first group of simulations have regarded the choice of the materials constituting the grating. $\Delta n = n_1 - n_2$ has been fixed to 0.5, while the grating period Λ has been fixed to 0.5 µm. In Fig. 3.25 the α trend vs n_1 is reported by considering $\Delta\theta_{In} = 4°$:

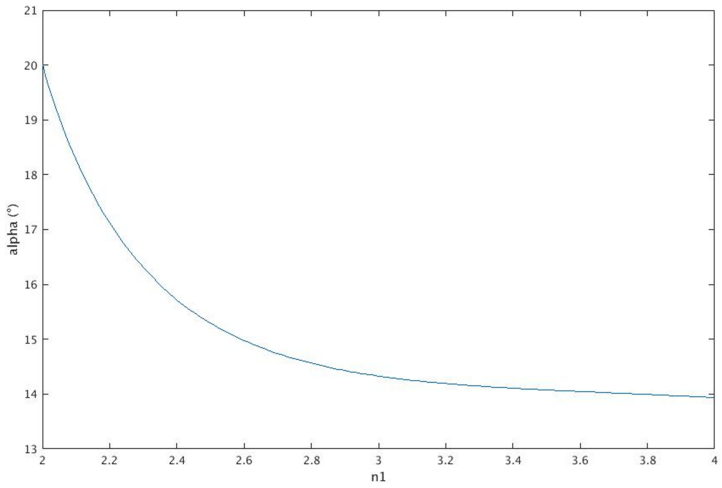


Figure 3.25. α variations vs n_1.

As it can be seen from Fig. 3.25, the highest angle variation is obtained when $n_1 = 2$ is considered (a beam deflection of 20° is obtained for an incident angle variation of 4°). For this reason, silicon carbide (SiC) has been chosen; among all of the possible materials that could have been taken into account, SiC has been preferred due to its high mechanical strength, wide bandgap and large thermal conductivity [211]. The abovementioned properties of SiC make it a promising material even for photonic and optoelectronic applications [212].

The second group of simulation regarded the choice of the layer to be alternated with SiC to constitute the grating. Other simulations have been performed considering $n_1 = 2$ and grating period $\Lambda = 0.5$ µm while observing α variations. Results are shown in Fig. 3.26.

As it can be seen from Fig. 3.26, smaller Δn variations produce higher angle deviations. However, in order to consider the feasibility of the fabrication process, it is worth to notice that these alternating layers are not stacked but are horizontally placed next to each other. For this reason, a more convenient choice should be a $\Delta n = 1$. This, indeed, implies that the grating is constituted by alternating layers of SiC and air (whose refractive index is equal to 1), which is a more practical choice, especially for the fabrication of a proof-of-principle device.

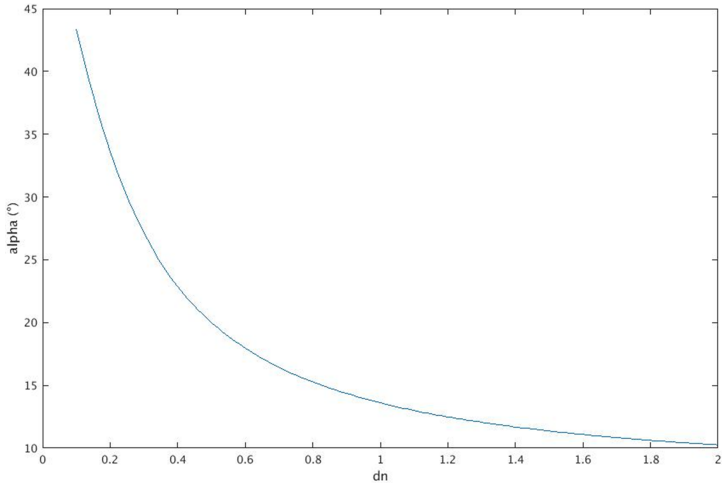


Figure 3.26. α variations vs Δn.

The last group of simulation has been performed considering which d/a ratio (where d = s_h is n_1 material thickness and a = s_l is n_2 material thickness) allows the best device stability performance against the fabrication parameters tolerance. Indeed, when fabricating a device, some tolerance on the geometrical parameters must always be taken into account. It is therefore desirable that the fabricated device performances should be as stable as possible despite a little percentage of variability (typically less than 10 %) on the geometrical parameters. In Fig. 3.27 is reported, for increasing Δn values, the angle deviations for different d/a ratios. It is clear that the ratio d/a = 0.5 allows the best stability in terms of fabrication tolerances, ensuring that the beam deviations are not due to a discrepancy between the fabricated device and the designed one, but are instead due to a real superprism effect.

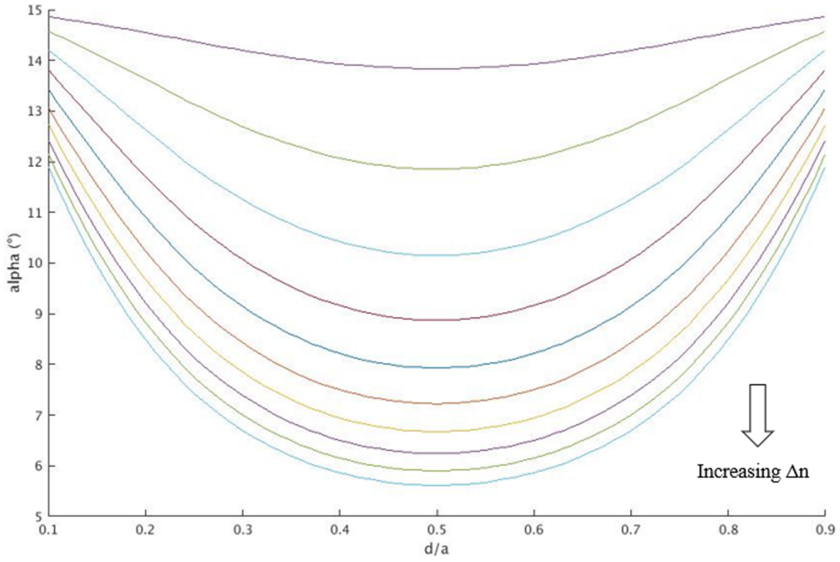


Figure 3.27. α variations vs d/a ratio.

The results deriving from these three simulation runs are here summarized:

- the material constituting the grating are SiC and air;
- a d/a = 0.5 ensures a good stability against fabrication tolerance.

With the constraints derived so far, other simulations were carried out with RSoft Cad Environment^{TM} in order to find the thickness of the layers constituting the grating. RSoft is a Finite Difference Time Domain (FDTD) simulator allowing 3D simulations of optical and photonic devices; in particular, the module FullWAVE^{TM} allows to perform a full-vector simulation of photonic structures even with non-uniform grids. The physical parameters required to perform such simulations are the refractive index distribution in space of the structure and the excitation fields, while the numerical parameters are the dimensions of the computational domain and of the grid size, the boundary conditions, the temporal grid (time steps) and the time required for the simulation.

The first step is to define such parameters; in particular, this definition is possible through a Graphical User Interface (GUI) or a command line interface. During this work, the first option has been used to design the proposed structure, as it can be seen in Fig. 3.28, where the contour plot of the refractive index distribution is shown. Indeed, when designing such structures, it is always preferable to perform a check of the resulting refractive index profile, in order to ensure that structure has been properly designed.

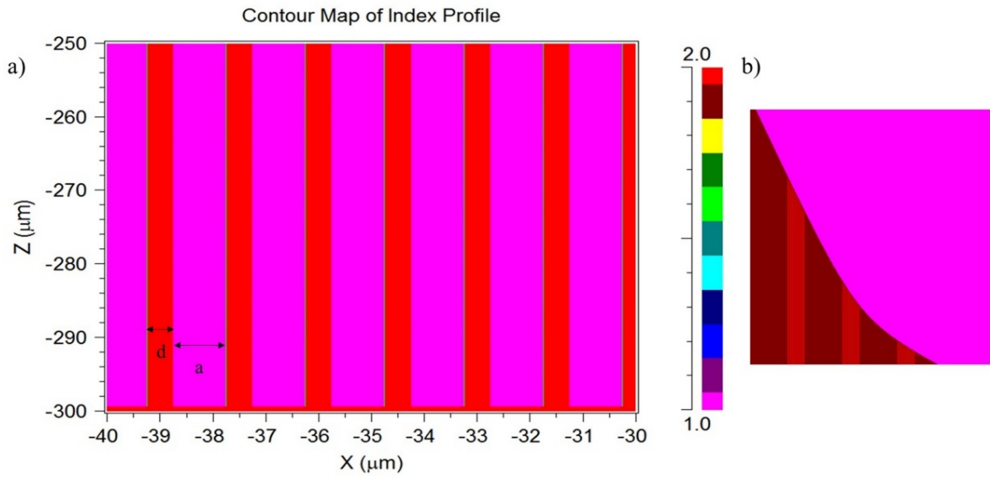


Figure 3.28. Contour plot of refractive index profile of the proposed structure.

In particular, in Fig. 3.28a, a zoom of the structure is shown, while, in Fig. 3.28b, the whole device is represented. The curved output surface empirically replies the hyperbolic dispersion relation (Eq. 3.14); such output surface is needed to avoid that the beam deviation achieved into the grating thanks to the superprism effect is lost due to the conservation of tangential component of the electric field at the crystal edges. On the contrary, an output surface whose shape is similar to the light dispersion inside the crystal will further increase the beam angle deviation [213]. For this reason, the final device output surface has the shape shown in Fig. 3.28b.

Once the desired structure in FullWAVE^{TM} module has been implemented, several simulations have been carried out to find the thickness of the alternating layers of SiC/air that maximizes the angle deviation inside and outside the structures. Results are shown in Fig. 3.29 for the following geometrical parameters:

- d = 0.5 µm;
- a = 1 µm;
- Λ = 1.5 µm.

This set of geometrical parameters ensures an angular amplification, defined as the ratio $\Delta\theta_{Out}/\ \Delta\theta_{In}$ (where $\Delta\theta_{Out}$ and $\Delta\theta_{In}$ are the output and input angular variation, respectively), of ~ 6, which is a good result for a 1D photonic crystal.

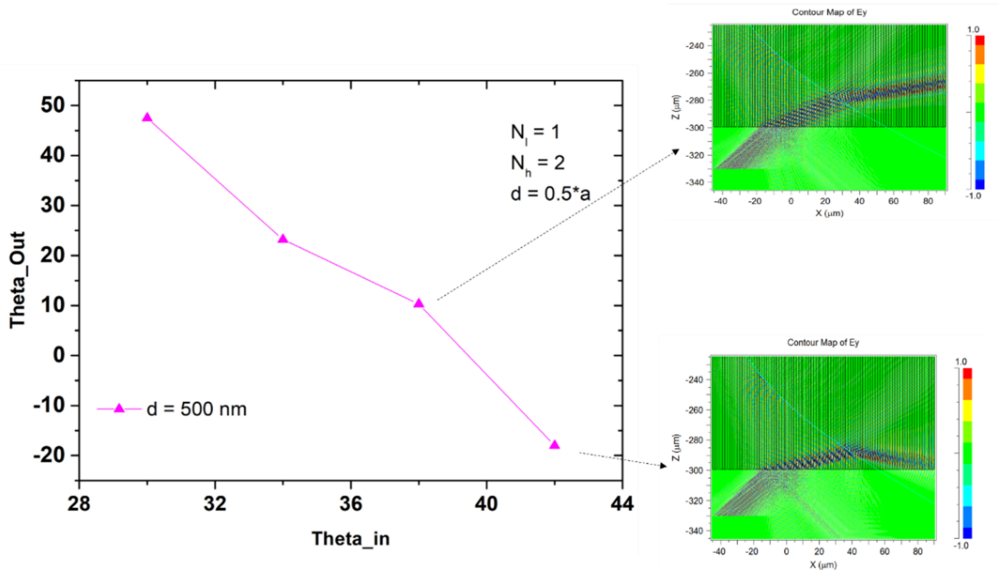


Figure 3.29. θ_{Out} vs θ_{In} for d = 0.5 µm and a = 1 µm. An angular amplification ~ 6 has been obtained for the proposed configuration.

The simulations performed so far to find this set of geometrical parameters have been carried out considering a 2D structure (i.e., the crystal is thought to be infinite in the third dimension, the vertical one) due to the time complexity of such numerical studies. In order to define the last geometrical parameter (the height of the SiC column constituting the grating), some simplified simulations have been performed to find the SiC thickness to ensure that the beam remains confined inside the structure and it is not absorbed by the substrate. In Fig. 3.30 appears clearly that for 1 µm thick SiC pillars the electrical field is strictly confined within the structure without dispersion in the substrate, constituted of a silicon dioxide (SiO_2) optical buffer layer interposed between SiC structure and Si substrate. This buffer layer avoids the light to enter within the Si substrate due to its higher refractive index (3.48 against 2 of SiC). Therefore, the presence of the SiO_2 layer (whose refractive index is 1.48) ensures the right optical confinement together with the correct vertical sizing of the SiC pillars.

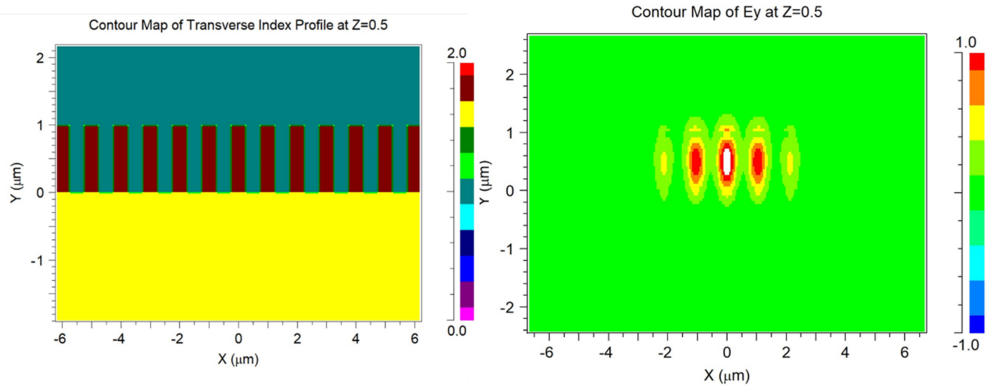


Figure 3.30. Vertical field confinement inside the structure.

Once the full set of geometrical parameters has been found, the device has been fabricated by Electron Beam Lithography and Reactive Ion Etching processes, as it will be shown in the following paragraph.

3.3.3 Fabrication process

The fabrication process flow chart of the proposed structure is summarized in Fig. 3.31; it consists of the following steps:

- deposition of 1 µm-thick SiO_2 film through Low Temperature Oxidation technique;
- deposition of 1 µm-thick SiC film through Plasma Enhanced Chemical Vapor Deposition technique;
- deposition of 5 nm-thick chromium (Cr) layer through DC sputtering technique;
- deposition of $\sim$ 250 nm-thick PMMA layer through spin coating technique;
- deposition of $\sim$ 5 nm-thick gold (Au) layer via DC sputtering technique;
- EBL patterning of the electroresist;
- Au layer wet etching in iodine solution and resist development;
- deposition of $\sim$ 70 nm-thick Cr film via DC sputtering technique;
- lift-off process;
- RIE process;
- Cr wet etching in Chrome Etch 18 solution.

The fabrication flow chart shown in Fig. 3.31 is much complex than those presented in Sect. 3.1.2 for the fabrication of the proposed biochemical sensor and in Sect. 3.2.2 for the fabrication of the proposed optical switch. Indeed, EBL patterning on SiC substrates requires additional fabrication steps, as it will be explained next.

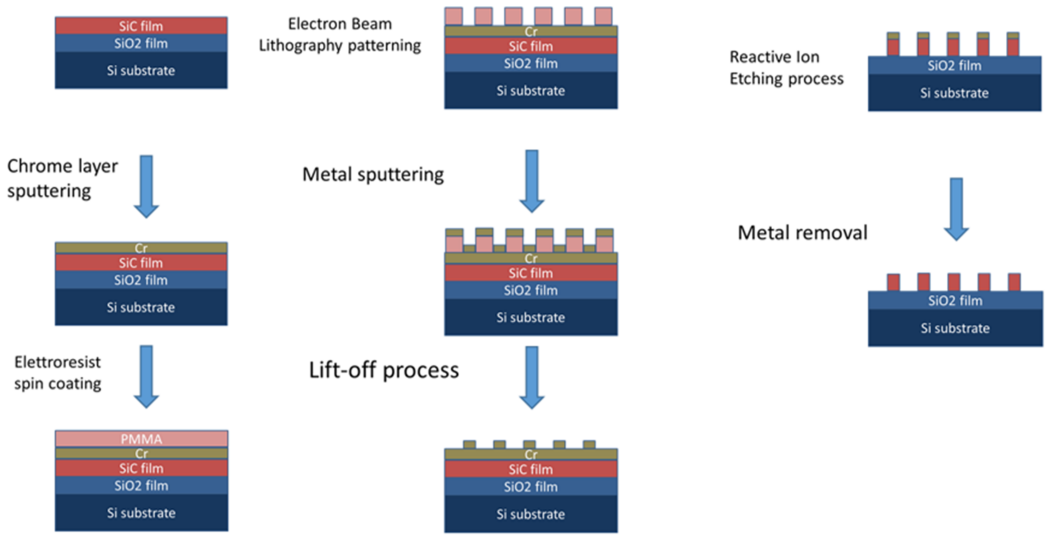


Figure 3.31. Superprism-based grating fabrication flow chart.

The first fabrication step has been the deposition of the 1 µm-thick SiO_2 layer through a Low Pressure Chemical Vapor Deposition (LPCVD). This process has been performed thanks to a collaboration with Dr. Caterina Summonte's group into the Clean Room laboratory (Class 100) of Institute for Microelectronics and Microsystems (National Council of Research) of Bologna by means of a SEMCO MiniLab DF 500 Horizontal LPCVD, shown in Fig. 3.32.



Figure 3.32. SEMCO Minilab DF 500 equipment for LTO deposition.

In particular, the deposited SiO_2 is a Low Temperature Oxide (LTO), that has been obtained through the following reaction at 450° with a deposition rate of 0.275 nm/s:

$$SiH_4 + O_2 = SiO_2 + 2H_2 \tag{3.22}$$

After the deposition of the SiO_2 layer, 1 µm-thick SiC film deposition has been performed by means of Plasma Enhanced Chemical Vapor Deposition (PECVD) into the Clean Room laboratory (Class 100000) of Institute for Microelectronics and Microsystems (National Council of Research) of Bologna. The deposited film is a stochiometric hydrogenated amorphous SiC (a-SiC:H) film, deposited into an Elettrorava - MVSystem, shown in Fig. 3.33.

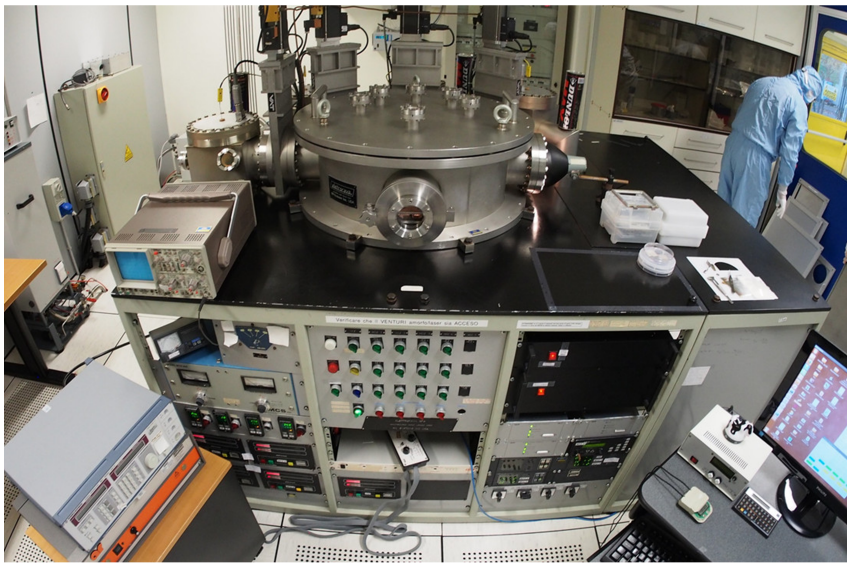


Figure 3.33. Elettrorava - MVSystem employed for the deposition of SiC films.

The a-SiC:H film has been growth on the LTO film previously deposited on Si substrate considering a SiH_4+CH_4+H_2 gas mixture with the following process parameters:

Table 3.3. a-SiC:H PECVD deposition parameters.

RF Frequency	RF Power	Working temperature	Working pressure	SiH_4 flow rate	CH_4 flow rate	H_2 flow rate
100 MHz	50 W	350 °C	0.3 mbar	4 sccm	23 sccm	25 sccm

The optimized set of SiC PECVD deposition parameters summarized in Table 3.3 allowed the deposition of a a-SiC:H film on a 4" silicon wafer with excellent uniformity (film thickness variations are lower than 10%, as shown in Fig. 3.34) and with a refractive index equal to 2.14, as derived from the ellipsometric characterization shown in Fig. 3.35.

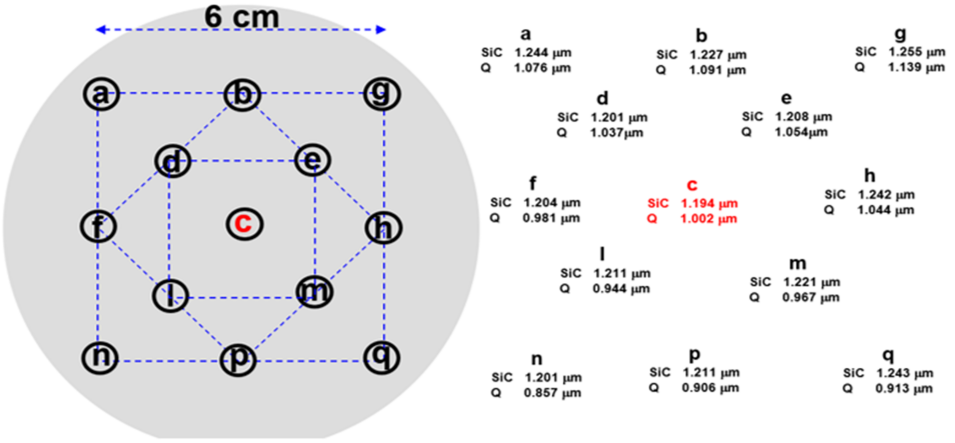


Figure 3.34. Thickness map of PECVD a-SiC:H film and LTO film on Si substrate.

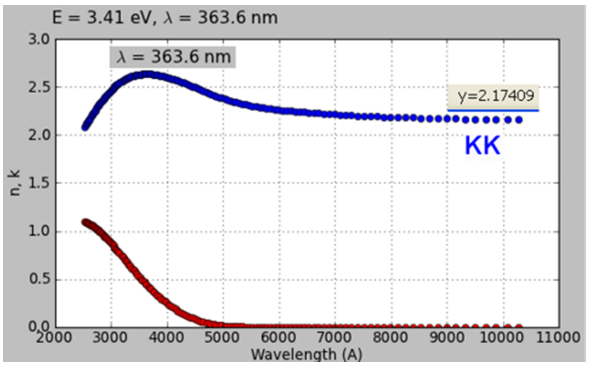


Figure 3.35. Ellipsometric characterization of deposited SiC film performed on three areas of 9 mm^2.

The subsequent fabrication step has been the deposition via DC sputtering of a thin Cr buffer layer ($\sim$ 5 nm) on SiC substrate. This step is required to avoid the extraordinary PMMA adhesion on SiC film, which causes the failure of the lift-off process as shown in Fig. 3.36.

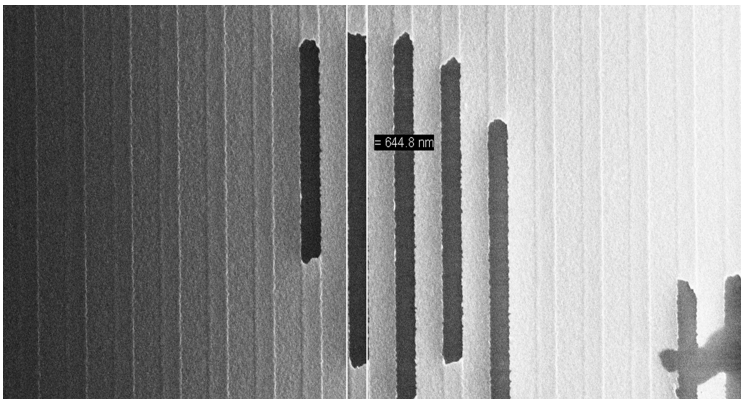


Figure 3.36. A failed lift-off process due to the strong PMMA adhesion on SiC substrate.

This issue is thought to be due to the strong adhesion of the C-atoms of SiC layer to PMMA chains [214], which would prevent the resist peel-off from the substrate as shown in Fig. 3.36. The addition of a thin Cr layer interposed between SiC and PMMA film avoids such adhesion allowing the success of the lift-off process even for more critical dimensions, as shown in Fig. 3.37. The resist deposited on the Cr layer instead of the SiC film has indeed been removed even in the very thin spacing of 63 nm between two adjacent unexposed regions without critical issues.

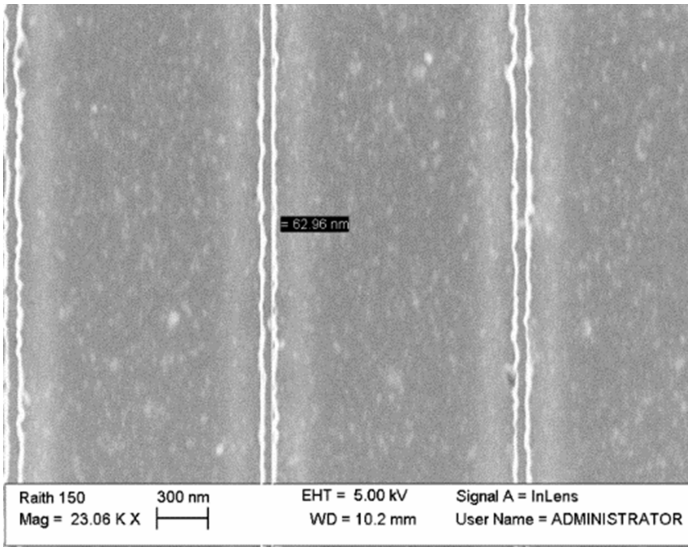


Figure 3.37. A lift-off process successfully carried out on SiC substrate even for a critical dimension of 63 nm when the Cr layer has been interposed between SiC and PMMA layer.

In order to transfer the device design presented in Sect. 3.3.2 into the SiC layer via EBL and RIE processes, a $\sim$ 280 nm-thick PMMA layer must be deposited on the 5 nm-thick Cr layer. In particular, PMMA diluted at 4% in Anisole has been deposited via spin coating at 3000 round-per-minute (rpm) for 60 s, and then baked at 180 °C for 3 minutes. With this spin coating recipe, the final film thickness is about 270 nm. Before patterning the resist film with EBL, a $\sim$ 5 nm-thick Au layer has been deposited on the PMMA layer via DC sputtering to favor the charge dissipation during electron exposure.

The device design provided with RSoft CAD Environment^{TM} has been directly imported into GDSII Raith software thanks to the possibility to export the RSoft .ind files into an ASCII format, which can be converted into the internal GDSII file directly from Raith software. Since a RIE process must be carried out with a metallic Cr mask, obtained via a lift-off, a low-energy EBL patterning has been performed with the following exposure parameters: acceleration voltage of 10 kV, numerical aperture of 30 µm, dose of 120 µC/cm^2 and step size of 20 nm. With this set of exposure parameters, it is possible to expose on the PMMA layer the grating structure in very reasonable times: an exposure area of 400 µm x 200 µm requires only $\sim$ 13 minutes exposure.

The desired design is effectively transferred into the resist layer with the development procedure, which consists of the following steps:

- Au wet etching in iodine solution for $\sim$ 13 s;
- substrate rinsing in de-ionized water;
- PMMA developing into 1:3 MIBK to IPA ratio solution for 45 s;
- substrate rinsing in isopropyl alcohol for 1 min;
- substrate drying under N_2 flux.

Since a Cr etching rate of 0.14 nm/s has been measured for the employed RIE system, a $\sim$ 70 nm Cr mask is thick enough to sustain the whole etching process, which requires that the etching depth of the final structure must be 1 µm. This mask has been obtained by depositing a 70 nm-thick Cr film on the patterned PMMA layer and then by removing the PMMA with a lift-off process, consisting of the following steps:

- warm bath ($\sim$ 80 °C) in PG remover for 15 minutes;
- ultrasonic bath for 10 s;
- substrate rinsing in isopropyl alcohol for few seconds;
- substrate drying under N_2 flux.

A SEM analysis of the fabricated device has been performed in order to verify the structure dimension and, eventually, to apply a correction to the designed mask in order to better match the structure design. In Fig. 3.38 and Fig. 3.39, SEM images of the chromium structure that will act as the mask for the RIE process and the detail of its dimensions are shown.

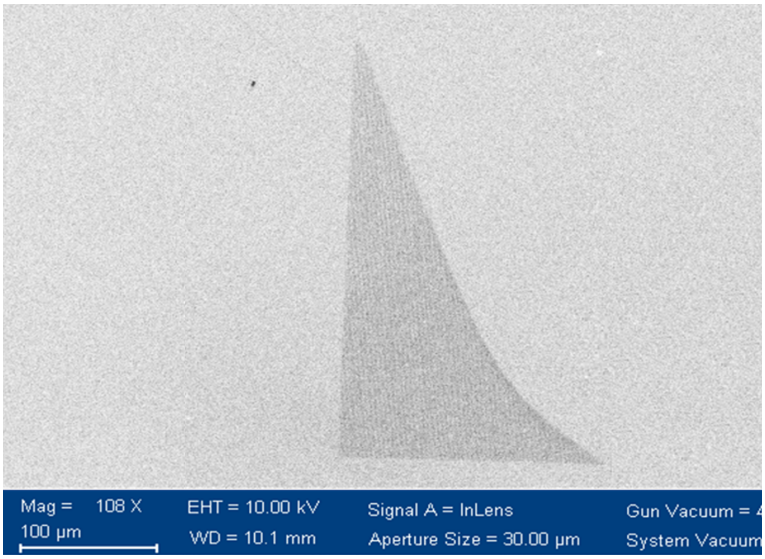


Figure 3.38. SEM image of the chrome mask resulting on SiC substrate after the lift-off process.

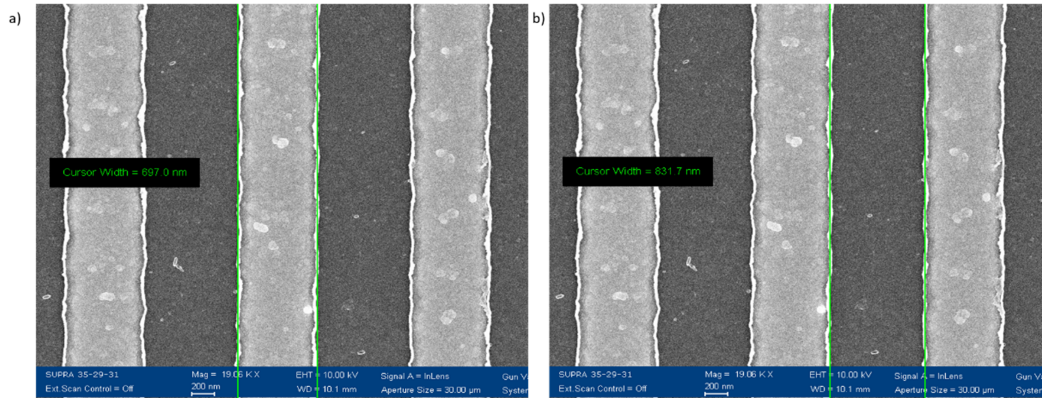


Figure 3.39. SEM metrological analysis of the structure dimensions after lift-off process.

In particular, as it can be seen in Fig. 3.39a, the Cr lines which will protect the SiC substrate during RIE process have been oversized due to the non-perfect anisotropy of the RIE process, while the unprotected SiC zones have been undersized for the same reason (see Fig. 3.39b). Indeed, a low lateral etching occurs, reducing SiC pillars dimensions even under the chrome mask and therefore ensuring the correct sizing of the final device.

Since the lift-off process has been successfully carried out, the structure can be finally transferred into the SiC layer via a RIE process. An Oxford Plasmalab 80 Plus RIE system has been used to etch the structure with a CF_4 and O_2 gas mixture. The parameters of the RIE process are summarized in Table 3.4.

Table 3.4. RIE process parameters employed for the etching the SiC grating.

RF Power	**Bias voltage**	**Working pressure**	**CF_4 flow rate**	**O_2 flow rate**	**Etching time**
300 W	730 V	$1.0{\cdot}10^{-1}$ mbar	50 sccm	2 sccm	5:30 min

The etching rate of SiC with the proposed etching recipe is resulted to be equal to 3.33 nm/s. The first $\sim$ 30 s of the RIE procedure are needed to etch the thin Cr layer deposited on the SiC film to isolate it from the PMMA layer. Only when this Cr layer has been fully etched, the real SiC etching process starts, requiring $\sim$ 5 minutes.

The residual Cr mask is then removed with the following process:

- wet etching in Cr Etch 18 solution for $\sim$ 5 minutes;
- substrate rinsing in de-ionized water;
- substrate drying under N_2 flux.

In order to perform a morphological characterization of the fabricated device, both SEM and AFM analysis have been performed. SEM images, shown in Fig. 3.40, Fig. 3.41a and Fig. 3.41b, demonstrate that the Cr mask oversizing has been correctly dimensioned: the final device dimensions, indeed, correspond to the device design explicated in Sect. 3.3.2.

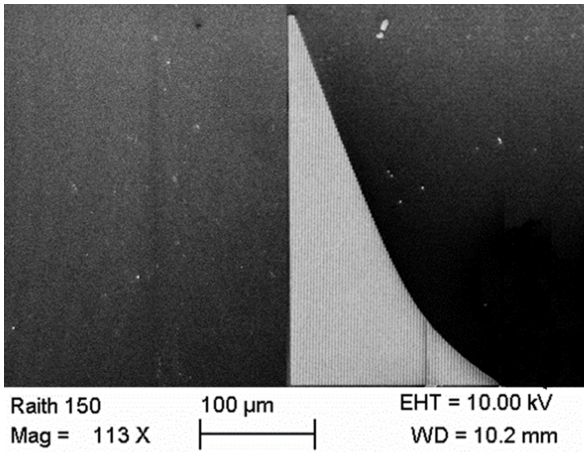


Figure 3.40. A SEM overview image of the fabricated device after the RIE process.

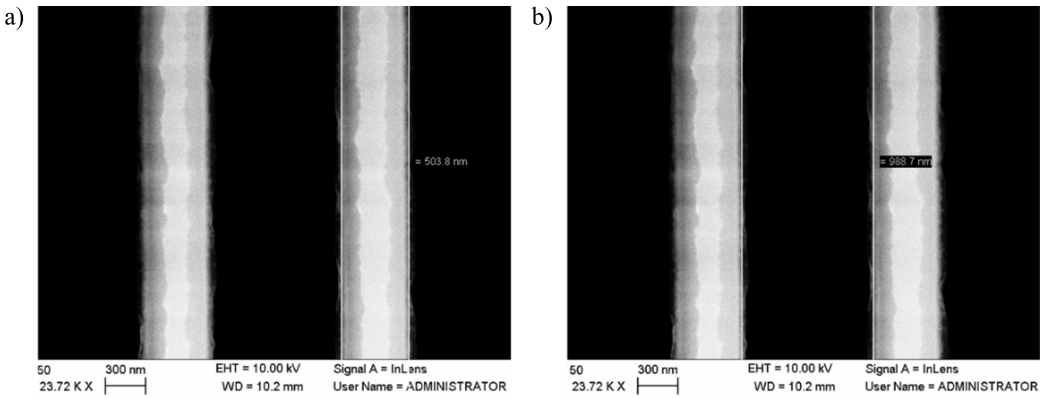


Figure 3.41. SEM metrology of the etched device.

Since the SEM analysis gives informations only on the metrology of the device surface, an atomic force microscopy (AFM) analysis has also been performed in order to check the morphology of the vertical walls of the SiC pillars. Results are shown in Fig. 3.42.

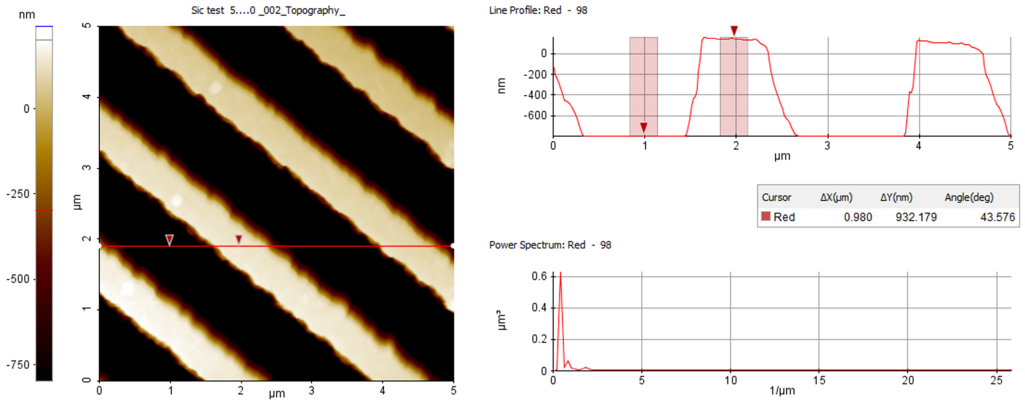


Figure 3.42. AFM analysis of SiC grating.

This analysis confirms that the etching process has been successfully carried out: the device is fully etched between adjacent SiC pillars with a resulting etching depth of $\sim$ 932 nm.

The fabricated device dimensions fulfill the design specifications within a tolerance lower than 10%, that is considered as a good fabrication result.

3.3.4 Device characterization

A preliminary characterization of the fabricated device has been performed by designing two input waveguides at different incident angles (38° and 42°) and four output waveguides at different angles (-20°, 12°, 24° and 48°) following the numerical results presented in Fig. 3.29. The characterized device is shown in Fig. 3.43.

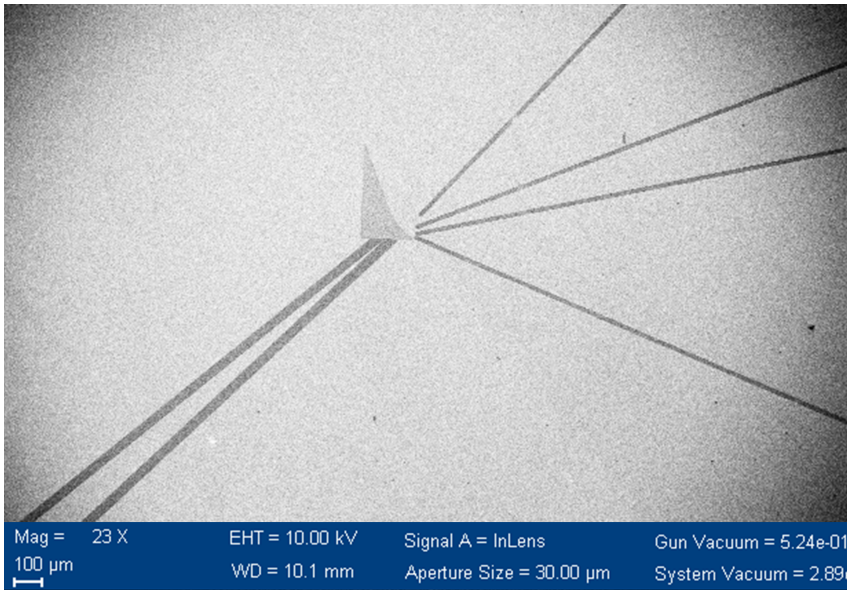


Figure 3.43. SEM image of the measured device.

This device has been characterized by exciting one waveguide at a time with a Melles Griot diode laser at $\lambda = 1.55$ µm and by collimating light with a 20x Mitutoyo objective lens; a Thorlabs multimodal fiber has been used to collect light from the output waveguides and to read the power at the waveguide exit with a Newport power meter. A scheme of the measurement setup is shown in Fig. 3.44.

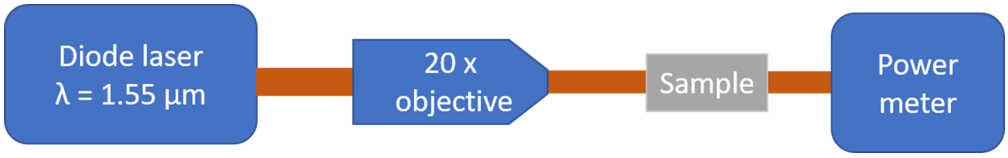


Figure 3.44. Schematization of the preliminary measurement setup.

The objective, the sample and the multimodal fiber are placed on Thorlabs micropositioners to ensure the correct alignment of the different components of the measurement setup, shown in Fig. 3.45.

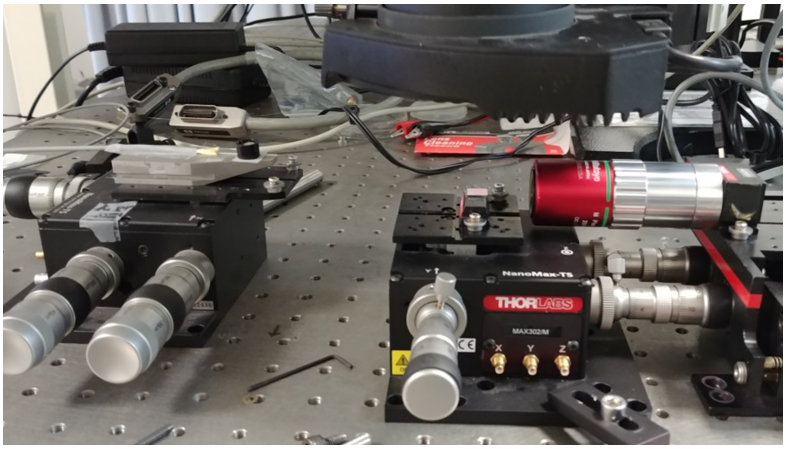


Figure 3.45. Picture of the measurement setup.

By exciting the input waveguide at 42° incident angle, a low power signal has been read from the output waveguide whose angle was -10° while no signal was read by the other output waveguides, as expected from the numerical simulations shown in Fig. 3.29. At the same time, by exciting the 38° incident angle waveguide, a low signal was read from the 12° output waveguide, while no signal was read from the other ones. The low level of the collected signals may be due to the roughness of the input waveguide surfaces or even to the scattering at the output waveguide surface, therefore further improvements have to be performed in order to characterize the proposed device with this measurement configuration.

Other characterizations have been performed, thanks to a collaboration with Dr. Luca Ortolani (CNR – IMM, Unit of Bologna), by cutting the input and output edges of the device with a dicer cut and then by polishing these surfaces with a FIB milling, as shown in Fig. 3.46.

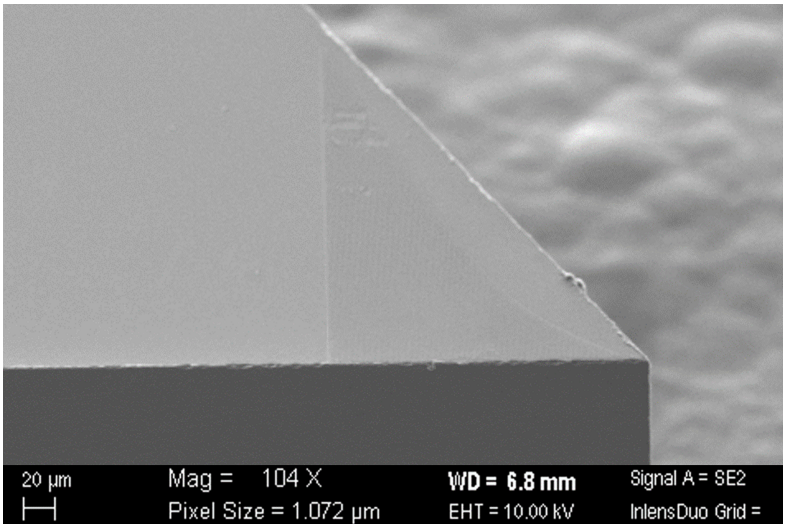


Figure 3.46. SEM image of the device edges cut with a dicer and then polished with FIB milling.

The measurement setup for this device configuration has been slightly modified respect to the one shown in Fig. 3.44: the power meter has been replaced by a CCD camera placed in correspondence of the output surface, while the chip has been placed on a Thorlabs rotation stage, as schematically shown in Fig. 3.47.

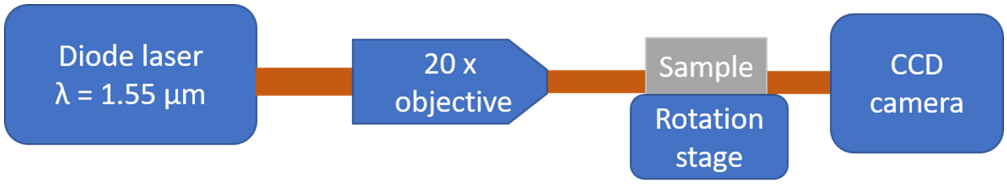


Figure 3.47. Schematization of the measurement setup used for the characterization of the FIB-milled device.

The sample placed on the rotation stage was excited by the impinging light at different angles; unfortunately, for each of these angles the CCD camera recorded several spots of the outcoming light. This may be due to the roughness of the input surface, shown in Fig. 3.48, that causes the scattering of the impinging light and hence the excitation of higher grating orders. Moreover, some of these spots may be due to a partial coupling of the impinging light within the underlying silicon substrate. In order to limit this issue, a thicker SiO_2 buffer layer can be designed and fabricated for the future developments of the proposed device.

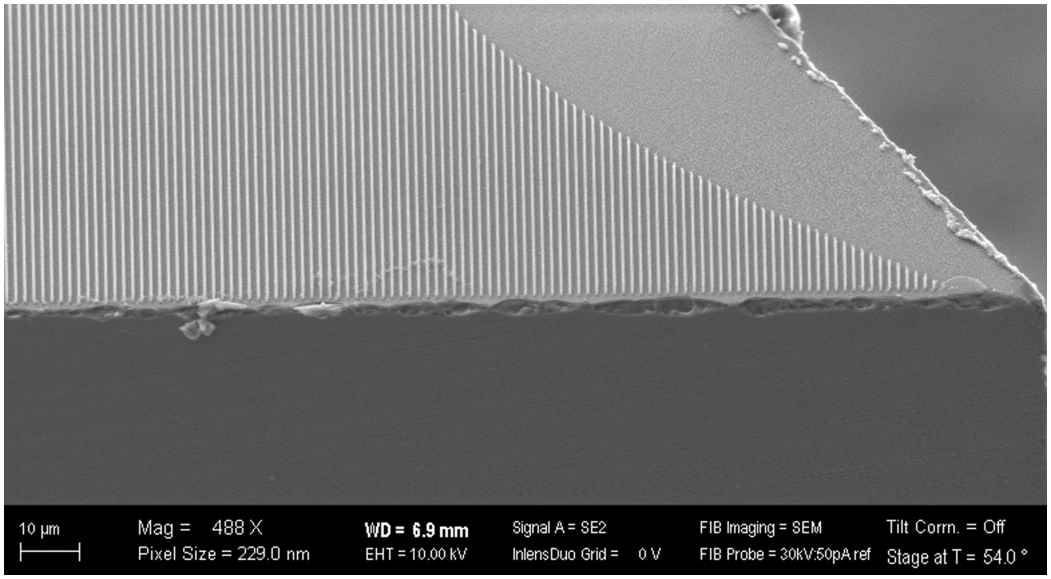


Figure 3.48. SEM image of the input surface after cut and FIB milling.

Although the collected signals in the first measurement configuration were only slightly above the noise signal, these results appear promising for the steering capabilities of the proposed device.

3.3.5 Conclusions and future perspectives

A silicon-based 1D PhC has been designed to work as an in-plane beam steering device at telecommunication wavelength (1.55 µm). The proposed structure is constituted of a SiC/air grating fabricated on a silicon substrate. An optical buffer layer constituted by a SiO_2 film interposed between the SiC film and the Si substrate has also been designed to optically confine the light within the grating structure. The fabrication process that led to the physical realization of the proposed device has been long and complex, but it has been successfully carried out despite the technological issues encountered during the device development.

In the future, several optimizations have to be carried out in order to characterize the device performances: for example, an optimized array of input waveguides at different incident angles can be designed in order to verify the angular deviation offered by the developed device. This characterization method, however, offers the possibility to vary the input angle only in a discrete way; on the other hand, to perform a continuous characterization of the device, a possible solution is the milling of the input surface via FIB system in order to have a smooth input surface that can be directly excited with an impinging light beam with an arbitrary incident angle. However, careful precautions must be taken to ensure that the input and output surfaces are smooth enough to avoid the excitation of higher grating orders that affect the device behavior.

Anyway, although the low-level signals collected during the device characterization, the proposed structure appears as a promising beam steering device operating at telecommunication wavelength without any moving part, being therefore capable to unify the requirements of non-mechanical steering and silicon-based integrated photonic devices.

Conclusions

The aim of this thesis work has been the integration of photonic nanostructures on silicon substrate through micro- and nanofabrication techniques. In particular, the development of three different new devices finding applications in sensing, telecommunications and microelectronics, respectively, has been demonstrated.

The first device is a plasmonic biochemical sensor constituted by an array of gold cross-shaped nanoantennas (NAs) supporting Localized Surface Plasmon Resonances (LSPRs) fabricated by means of Electron Beam Lithography (EBL) and lift-off process on a silicon substrate. The dependence of the LSPR of the NAs shape and geometrical parameters allows to tune the plasmonic resonance in correspondence of almost any region of the electromagnetic spectrum, making therefore this device suitable for Surface Enhanced InfraRed Absorption (SEIRA) spectroscopy. Indeed, when a broadband plasmonic resonance is superimposed with a narrowband molecular vibration signature, a variation of the reflection/transmission coefficient of the NAs array appears, allowing the identification of the adsorbed species even when little amounts of analytes are used. In particular, by varying cross arm length, the LSPR has been tuned in correspondence of the C≡O triple bonding (2100 cm^{-1}) and in correspondence of the C=O stretching vibration (1600 cm^{-1}) for the detection of small and large molecules, respectively. For small molecules detection, the resonant effect did not appear due to the very small molecular weight of the employed compound, but a sensitivity of $\sim$ 600 nm/RIU has been evaluated for a fmol compound amount. On the other hand, in the case of large molecules detection, a sensitivity of $\sim$ 500 nm/RIU has been evaluated and the resonant effect appeared. This allowed to calculate an enhancement factor (which is the union of a gain factor and a geometrical factor) of $\sim$ 45000. This device is therefore very suitable for both sensitive SEIRA spectroscopy and refractive index sensing. As a future perspective, NAs of different materials should be considered in order to make the device fabrication fully CMOS compatible: in this case, the use of gold should be avoided (but at the cost of lower material biocompatibility) in favour of other plasmonic materials, like aluminum.

The second device is a new silicon-based all-optical switch for telecommunication applications. It couples the advantages offered by metamaterials in light manipulation and phase change materials (PCM) in the optically-driven switching among two or more stable phases. As a proof of principle, an array of silicon nanorods has been fabricated on a Silicon-on-Insulator (SOI) substrate and then covered with a thin layer of germanium telluride (GeTe), a PCM showing a very good adhesion to silicon. By thermally inducing the GeTe phase transition from amorphous to crystalline state, a variation of the reflection coefficient of the metasurface is observed with

a contrast ratio (defined as the ratio between the transmitted powers in the two stable phases of the PCM) of ~ 5. However, a Raman spectroscopy analysis shows that even after the transition from amorphous to crystalline phase of the GeTe layer there is a lower amount of crystals on the bottom of the Si nanorod than on the top, due to the different strain suffered by the GeTe film. This suggests that a further improvement of the device (i.e., sharper resonances and higher contrast ratios) can be obtained by designing a metamaterial where the GeTe layer is only on the top of Si nanorods, so that not only smaller amounts of material must change their phase. In addition, the phase change provided by a laser pump would lead to fast, non-volatile and reconfigurable reflection switches.

The third developed device is a new silicon-based integrated grating structure for an in-plane non-mechanical steering of light to act as an interconnection device. Its application could be in smart intra- and inter-chip signal addressing. It has a one-dimensional planar photonic crystal (PhC) structure constituted by alternating wiress of silicon carbide (SiC) and air, capable of a numerical angular amplification (defined as the ratio of the output angular variation on the input angular variation) of ~ 6. Its realization required the overcoming of several fabrication issues, and in particular: 1) the lift-off process was optimized by interposing a thin chromium buffer layer between the SiC film and the resist layer; 2) due to the high depth required for the vertical confinement of light (1 µm), a proper optimization of the etching mask and, above all, of the etching parameters was performed. Finally, a careful process optimization allows an excellent reproducibility of the different fabrication steps, and very good agreement with the design specifications. The device characterization is underway, and several tests are going to be performed in order to demonstrate its effective operation for in-plane interconnect.

In conclusion, the thesis work has explored different silicon-based nanotechnologies that can be successfully exploited in the realization of a next generation of photonic components to be monolithically integrated with other optoelectronic circuits on chip. They span from plasmonic metamaterial structures to all-dielectric photonic crystals, and exploit unconventional materials such as phase transition germanium telluride and silicon carbide. The technological efforts have been addressed to the realization of three new device configurations of actual interest in photonics.

List of Publications

JOURNALS

- P. Malara, A. Crescitelli, V. Di Meo, A. Giorgini, S. Avino, E. Esposito, A. Ricciardi, A. Cusano, I. Rendina, P. De Natale and G. Gagliardi, "Resonant enhancement of plasmonic nanostructured fiber optic sensors", Sensors and Actuators B: Chemical, vol. 273, pp. 1587–1592, 2018.

- G. Quero, P. Vaiano, F. Fienga, M. Giaquinto, V. Di Meo, G. Gorine, P. Casolaro, L. Campajola, G. Breglio, A. Crescitelli, E. Esposito, A. Ricciardi, A. Cutolo, F. Ravotti, S. Buontempo, M. Consales, A. Cusano, "A novel Lab-on-Fiber Radiation Dosimeter for Ultra-high Dose Monitoring", Scientific Reports, vol. 8, no. 1, p. 17841, 2018.

- V. Di Meo, A. Caporale, A. Crescitelli, M. Janneh, E. Palange, A. De Marcellis, M. Portaccio, M. Lepore, I. Rendina, M. Ruvo, E. Esposito, "Metasurface based on cross-shaped plasmonic nanoantennas as chemical sensor for surface-enhanced infrared absorption spectroscopy", Sensors and Actuators B: Chemical, vol. 286, pp. 600–607, 2019.

- E. Petronijevic, G. Leahu, V. Di Meo, A. Crescitelli, P. Dardano, G. Coppola, E. Esposito, I. Rendina, M. Miritello, M. G. Grimaldi, V. Torrisi, G. Compagnini, C. Sibilia, "Near-infrared modulation by means of GeTe/SOI-based metamaterial", Optics letters, vol. 44, no. 6, pp. 1508–1511, 2019.

CONFERENCES

- E. Petronijevic, G. Leahu, V. Di Meo, A. Crescitelli, P. Dardano, G. Coppola, E. Esposito, I. Rendina, M. Miritello, M. G. Grimaldi, C. Sibilia, "Eit-like all-dielectric metamaterials with phase changing layers for all-optical switching applications", 19th Italian National Conference on Photonic Technologies (Fotonica 2017), 2017.

- G. Quero, P. Vaiano, F. Fienga, M. Giaquinto, V. Di Meo, G. Gorine, P. Casolaro, L. Campajola, G. Breglio, A. Crescitelli, E. Esposito, A. Ricciardi, A. Cutolo, F. Ravotti, S. Buontempo, M. Consales, A. Cusano, "Ultra-high Dose Monitoring with Innovative Lab-on-Fiber Radiation Dosimeter", 7th International Symposium on Sensor Science (I3S 2019), MDPI Proceeding, 2019.

Bibliography

[1] Graphcore. https://www.graphcore.ai. Accessed: 2018-10-01.

[2] David AB Miller. Device requirements for optical interconnects to silicon chips. *Proceedings of the IEEE*, 97(7):1166–1185, 2009.

[3] Zhou Fang and Ce Zhou Zhao. Recent progress in silicon photonics: a review. *ISRN Optics*, 2012, 2012.

[4] RA Soref and JP Lorenzo. Single-crystal silicon: a new material for 1.3 and 1.6 μm integrated-optical components. *Electronics Letters*, 21(21):953–954, 1985.

[5] CZ Zhao, EK Liu, GZ Li, N Li, and L Guo. Silicon raised strip waveguides based on silicon and silicon dioxide thermal bonding. *IEEE Photonics Technology Letters*, 9(4):473–474, 1997.

[6] CZ Zhao, EK Liu, GZ Li, and L Guo. Silicon-on-insulator optical intensity modulator based on waveguide-vanishing effect. *Electronics Letters*, 32(18):1667–1667, 1996.

[7] Ce Zhou Zhao, Ai Hua Chen, EK Liu, and GZ Li. Silicon-on-insulator asymmetric optical switch based on total internal reflection. *IEEE Photonics Technology Letters*, 9(8):1113–1115, 1997.

[8] Lukas Chrostowski, Samantha Grist, Jonas Flueckiger, Wei Shi, Xu Wang, Eric Ouellet, Han Yun, Mitch Webb, Ben Nie, Zhen Liang, et al. Silicon photonic resonator sensors and devices. In *Laser Resonators, Microresonators, and Beam Control XIV*, volume 8236, page 823620. International Society for Optics and Photonics, 2012.

[9] Xudong Fan, Ian M White, Siyka I Shopova, Hongying Zhu, Jonathan D Suter, and Yuze Sun. Sensitive optical biosensors for unlabeled targets: A review. *analytica chimica acta*, 620(1-2):8–26, 2008.

[10] Elain Fu, Timothy Chinowsky, Kjell Nelson, Kyle Johnston, Thayne Edwards, Kristen Helton, Michael Grow, John W Miller, and Paul Yager. Spr imaging-based salivary diagnostics system for the detection of small molecule analytes. *Annals of the New York Academy of Sciences*, 1098(1):335–344, 2007.

[11] Shon Schmidt, Jonas Flueckiger, WenXuan Wu, Samantha M Grist, Sahba Talebi Fard, Valentina Donzella, Pakapreud Khumwan, Emily R Thompson, Qian Wang, Pavel Kulik, et al. Improving the performance of silicon photonic rings, disks, and bragg gratings for use in label-free biosensing. In *Biosensing and Nanomedicine VII*, volume 9166, page 91660M. International Society for Optics and Photonics, 2014.

[12] Enxiao Luan, Hossam Shoman, Daniel Ratner, Karen Cheung, and Lukas Chrostowski. Silicon photonic biosensors using label-free detection. *Sensors*, 18(10):3519, 2018.

[13] Loic Laplatine, Enxiao Luan, Karen Cheung, Daniel M Ratner, Yonathan Dattner, and Lukas Chrostowski. System-level integration of active silicon photonic biosensors using fan-out wafer-level-packaging for low cost and multiplexed point-of-care diagnostic testing. *Sensors and Actuators B: Chemical*, 273:1610–1617, 2018.

[14] Wenjian Yang, Shijie Song, Xiaoke Yi, Suen Xin Chew, Liwei Li, and Linh Nguyen. Silicon-on-insulator microring resonator sensor based on an amplitude comparison sensing function. *Optics letters*, 43(1):70–73, 2018.

[15] Adam Densmore, D-X Xu, Philip Waldron, Siegfried Janz, Pavel Cheben, J Lapointe, A Delge, Boris Lamontagne, JH Schmid, and Edith Post. A silicon-on-insulator photonic wire based evanescent field sensor. *IEEE Photonics Technology Letters*, 18(23):2520–2522, 2006.

[16] Shuai Liu, Wenzhao Sun, Yujie Wang, Xiaoyi Yu, Ke Xu, Yongzhen Huang, Shumin Xiao, and Qinghai Song. End-fire injection of light into high-q silicon microdisks. *Optica*, 5(5):612–616, 2018.

[17] Aaron Schweinsberg, Sandrine Hocdé, Nick N Lepeshkin, Robert W Boyd, Christopher Chase, and Julie E Fajardo. An environmental sensor based on an integrated optical whispering gallery mode disk resonator. *Sensors and Actuators B: Chemical*, 123(2):727–732, 2007.

[18] Sourabh Sahu, Jalil Ali, Preecha P Yupapin, and Ghanshyam Singh. Porous silicon based bragg-grating resonator for refractive index biosensor. *Photonic Sensors*, pages 1–7, 2018.

[19] Przemek J Bock, Pavel Cheben, Jens H Schmid, Jean Lapointe, André Delâge, Dan-Xia Xu, Siegfried Janz, Adam Densmore, and Trevor J Hall. Subwavelength grating crossings for silicon wire waveguides. *Optics express*, 18(15):16146–16155, 2010.

[20] Pavel Cheben, Robert Halir, Jens H Schmid, Harry A Atwater, and David R Smith. Subwavelength integrated photonics. *Nature*, 560(7720):565, 2018.

[21] Peter Kozma, Florian Kehl, Eva Ehrentreich-Förster, Christoph Stamm, and Frank F Bier. Integrated planar optical waveguide interferometer biosensors: A comparative review. *Biosensors and Bioelectronics*, 58:287–307, 2014.

[22] Adrián Fernández Gavela, Daniel Grajales García, Jhonattan Ramirez, and Laura Lechuga. Last advances in silicon-based optical biosensors. *Sensors*, 16(3):285, 2016.

[23] Yi Zou, Swapnajit Chakravarty, Liang Zhu, and Ray T Chen. The role of group index engineering in series-connected photonic crystal microcavities for high density sensor microarrays. *Applied physics letters*, 104(14):141103, 2014.

[24] Jian Zhou, Lijun Huang, Zhongyuan Fu, Fujun Sun, and Huiping Tian. Multiplexed simultaneous high sensitivity sensors with high-order mode based on the integration of photonic crystal $1\times$ 3 beam splitter and three different single-slot pcncs. *Sensors*, 16(7):1050, 2016.

[25] Lin Zhang, Zhongyuan Fu, Fujun Sun, Chao Wang, and Huiping Tian. Highly sensitive one chip eight channel sensing of ultra-compact parallel integrated photonic crystal cavities based on silicon-on-insulator platform. In *Lasers and Electro-Optics Pacific Rim (CLEO-PR), 2017 Conference on*, pages 1–2. IEEE, 2017.

[26] Stefan Alexander Maier. *Plasmonics: fundamentals and applications*. Springer Science & Business Media, 2007.

[27] Francisco J Rodríguez-Fortuño, Alba Espinosa-Soria, and Alejandro Martínez. Exploiting metamaterials, plasmonics and nanoantennas concepts in silicon photonics. *Journal of Optics*, 18(12):123001, 2016.

[28] Jolly Xavier, Serge Vincent, Fabian Meder, and Frank Vollmer. Advances in optoplasmonic sensors–combining optical nano/microcavities and photonic crystals with plasmonic nanostructures and nanoparticles. *Nanophotonics*, 7(1):1–38, 2018.

[29] Lorenzo Pavesi. Routes toward silicon-based lasers. *Materials Today*, 8(1):18–25, 2005.

[30] Haisheng Rong, Ansheng Liu, Richard Jones, Oded Cohen, Dani Hak, Remus Nicolaescu, Alexander Fang, and Mario Paniccia. An all-silicon raman laser. *Nature*, 433(7023):292, 2005.

[31] Maria Miritello, Roberto Lo Savio, Fabio Iacona, Giorgia Franzò, Alessia Irrera, Alberto M Piro, Corrado Bongiorno, and Francesco Priolo. Efficient luminescence and energy transfer in erbium silicate thin films. *Advanced Materials*, 19(12):1582–1588, 2007.

[32] S Yerci, R Li, and L Dal Negro. Electroluminescence from er-doped si-rich silicon nitride light emitting diodes. *Applied Physics Letters*, 97(8):081109, 2010.

[33] Jifeng Liu, Xiaochen Sun, Dong Pan, Xiaoxin Wang, Lionel C Kimerling, Thomas L Koch, and Jurgen Michel. Tensile-strained, n-type ge as a gain medium for monolithic laser integration on si. *Optics express*, 15(18):11272–11277, 2007.

[34] Stephan Wirths, Richard Geiger, N Von Den Driesch, G Mussler, T Stoica, S Mantl, Z Ikonic, Ml Luysberg, S Chiussi, JM Hartmann, et al. Lasing in direct-bandgap gesn alloy grown on si. *Nature photonics*, 9(2):88, 2015.

[35] Guang-Hua Duan, Christophe Jany, Alban Le Liepvre, Alain Accard, Marco Lamponi, Dalila Make, Peter Kaspar, Guillaume Levaufre, Nils Girard, François Lelarge, et al. Hybrid iii–v on silicon lasers for photonic integrated circuits on silicon. *IEEE Journal of selected topics in quantum electronics*, 20(4):158–170, 2014.

[36] SM Chen, MC Tang, Junyongf Wu, Qimeng Jiang, VG Dorogan, M Benamara, YI Mazur, GJ Salamo, Alwyn J Seeds, and Huiyun Liu. 1.3 μm inas/gaas quantum-dot laser monolithically grown on si substrates operating over 100°. *Electronics Letters*, 50(20):1467–1468, 2014.

[37] Alan Y Liu, Chong Zhang, Justin Norman, Andrew Snyder, Dmitri Lubyshev, Joel M Fastenau, Amy WK Liu, Arthur C Gossard, and John E Bowers. High performance continuous wave 1.3 μ m quantum dot lasers on silicon. *Applied Physics Letters*, 104(4):041104, 2014.

[38] Tao Chu, Hirohito Yamada, Satomi Ishida, and Yasuhiko Arakawa. Compact 1× n thermo-optic switches based on silicon photonic wire waveguides. *Optics Express*, 13(25):10109–10114, 2005.

[39] Lei Qiao, Weijie Tang, and Tao Chu. Ultra-large-scale silicon optical switches. In *Group IV Photonics (GFP), 2016 IEEE 13th International Conference on*, pages 1–2. IEEE, 2016.

[40] Joris Van Campenhout, William MJ Green, Solomon Assefa, and Yurii A Vlasov. Low-power, 2× 2 silicon electro-optic switch with 110-nm bandwidth for broadband reconfigurable optical networks. *Optics Express*, 17(26):24020–24029, 2009.

[41] Lei Qiao, Weijie Tang, and Tao Chu. 32× 32 silicon electro-optic switch with built-in monitors and balanced-status units. *Scientific Reports*, 7:42306, 2017.

[42] Tae Joon Seok, Niels Quack, Sangyoon Han, Richard S Muller, and Ming C Wu. Large-scale broadband digital silicon photonic switches with vertical adiabatic couplers. *Optica*, 3(1):64–70, 2016.

[43] Piero Orlandi, Francesco Morichetti, Michael John Strain, Marc Sorel, Paolo Bassi, and Andrea Melloni. Photonic integrated filter with widely tunable bandwidth. *Journal of Lightwave Technology*, 32(5):897–907, 2014.

[44] Andrew Huang, Cary Gunn, Guo-Liang Li, Yi Liang, Sina Mirsaidi, A Narashimha, and Thierry Pinguet. A 10gb/s photonic modulator and wdm mux/demux integrated with electronics in 0.13/spl mu/m soi cmos. In *Solid-State Circuits Conference, 2006. ISSCC 2006. Digest of Technical Papers. IEEE International*, pages 922–929. IEEE, 2006.

[45] Stanley Cheung, Tiehui Su, Katsunari Okamoto, and SJB Yoo. Ultra-compact silicon photonic 512× 512 25 ghz arrayed waveguide grating router. *IEEE Journal of Selected Topics in Quantum Electronics*, 20(4):310–316, 2014.

[46] Xiaomeng Sun, Linjie Zhou, Jingya Xie, Zhi Zou, Liangjun Lu, Haike Zhu, Xinwan Li, and Jianping Chen. Tunable silicon fabry–perot comb filters formed by sagnac loop mirrors. *Optics letters*, 38(4):567–569, 2013.

[47] Lu Yangyang, Tian Yonghui, and Yang Lin. Integrated reconfigurable optical add-drop multiplexers based on cascaded microring resonators. *Journal of Semiconductors*, 34(9):094012, 2013.

[48] Safia Arafa, Mohamed Bouchemat, Touraya Bouchemat, and Ahlem Benmerkhi. Design of optical filter based on photonic crystal squared silicon nitride microcavity. *Nanoscience and Nanotechnology*, 6(1A):97–104, 2016.

[49] Wei Yang, Tiantian Li, Zhijuan Tu, Yanping Li, Xingjun Wang, and Ziyu Wang. A novel polarization converter and filter based on mmi couplers in silicon-on-insulator. In *CLEO: Applications and Technology*, pages JW2A–49. Optical Society of America, 2014.

[50] Shuang Zheng, Nan Zhou, Yun Long, Zhengsen Ruan, Jing Du, Xiao Hu, Li Shen, Shuhui Li, and Jian Wang. Compact tunable photonic comb filter on a silicon platform. *Optics letters*, 42(14):2762–2765, 2017.

[51] Po Dong, Ning-Ning Feng, Dazeng Feng, Wei Qian, Hong Liang, Daniel C Lee, BJ Luff, T Banwell, A Agarwal, P Toliver, et al. Ghz-bandwidth optical filters based on high-order silicon ring resonators. *Optics express*, 18(23):23784–23789, 2010.

[52] M Casalino, L Sirleto, L Moretti, M Gioffrè, G Coppola, and Ivo Rendina. Silicon resonant cavity enhanced photodetector based on the internal photoemission effect at 1.55 μ m: Fabrication and characterization. *Applied Physics Letters*, 92(25):251104, 2008.

[53] Shiyang Zhu, MB Yu, GQ Lo, and DL Kwong. Near-infrared waveguide-based nickel silicide schottky-barrier photodetector for optical communications. *Applied Physics Letters*, 92(8):081103, 2008.

[54] E Budianu, M Purica, F Iacomi, C Baban, P Prepelita, and E Manea. Silicon metal-semiconductor-metal photodetector with zinc oxide transparent conducting electrodes. *Thin Solid Films*, 516(7):1629–1633, 2008.

[55] Christine Scales, Ian Breukelaar, and Pierre Berini. Surface-plasmon schottky contact detector based on a symmetric metal stripe in silicon. *Optics letters*, 35(4):529–531, 2010.

[56] Zhen Sheng, Liu Liu, Joost Brouckaert, Sailing He, and Dries Van Thourhout. Ingaas pin photodetectors integrated on silicon-on-insulator waveguides. *Optics express*, 18(2):1756–1761, 2010.

[57] Long Chen and Michal Lipson. Ultra-low capacitance and high speed germanium photodetectors on silicon. *Optics Express*, 17(10):7901–7906, 2009.

[58] Silvia Fama, Lorenzo Colace, Gianlorenzo Masini, Gaetano Assanto, and Hsin-Chiao Luan. High performance germanium-on-silicon detectors for optical communications. *Applied Physics Letters*, 81(4):586–588, 2002.

[59] Donghwan Ahn, Ching-yin Hong, Jifeng Liu, Wojciech Giziewicz, Mark Beals, Lionel C Kimerling, Jurgen Michel, Jian Chen, and Franz X Kärtner. High performance, waveguide integrated ge photodetectors. *Optics express*, 15(7):3916–3921, 2007.

[60] Laurent Vivien, Andreas Polzer, Delphine Marris-Morini, Johann Osmond, Jean Michel Hartmann, Paul Crozat, Eric Cassan, Christophe Kopp, Horst Zimmermann, and Jean Marc Fédéli. Zero-bias 40gbit/s germanium waveguide photodetector on silicon. *Optics express*, 20(2):1096–1101, 2012.

[61] Hongtao Chen, P Verheyen, P De Heyn, G Lepage, J De Coster, S Balakrishnan, P Absil, W Yao, L Shen, Günther Roelkens, et al. - 1 v bias 67 ghz bandwidth si-contacted germanium waveguide pin photodetector for optical links at 56 gbps and beyond. *Optics Express*, 24(5):4622–4631, 2016.

[62] Joost Brouckaert, Gunther Roelkens, Dries Van Thourhout, and Roel Baets. Thin-film iii–v photodetectors integrated on silicon-on-insulator photonic ics. *Journal of Lightwave Technology*, 25(4):1053–1060, 2007.

[63] Harish Subbaraman, Xiaochuan Xu, Amir Hosseini, Xingyu Zhang, Yang Zhang, David Kwong, and Ray T Chen. Recent advances in silicon-based passive and active optical interconnects. *Optics express*, 23(3):2487–2511, 2015.

[64] EJ Teo, AA Bettiol, P Yang, MBH Breese, BQ Xiong, GZ Mashanovich, WR Headley, and GT Reed. Fabrication of low-loss silicon-on-oxidized-porous-silicon strip waveguide using focused proton-beam irradiation. *Optics letters*, 34(5):659–661, 2009.

[65] Anthony P Hope, Thach G Nguyen, Arnan Mitchell, and Wim Bogaerts. Quantitative analysis of tm lateral leakage in foundry fabricated silicon rib waveguides. *IEEE Photonics Technology Letters*, 28(4):493–496, 2016.

[66] Chengcheng Gui, Chao Li, Qi Yang, and Jian Wang. Demonstration of terabit-scale data transmission in silicon vertical slot waveguides. *Optics express*, 23(8):9736–9745, 2015.

[67] Kazuisao Tsuruda, Masayuki Fujita, and Tadao Nagatsuma. Extremely low-loss terahertz waveguide based on silicon photonic-crystal slab. *Optics Express*, 23(25):31977–31990, 2015.

[68] Valentina Donzella, Ahmed Sherwali, Jonas Flueckiger, Samantha M Grist, Sahba Talebi Fard, and Lukas Chrostowski. Design and fabrication of soi micro-ring resonators based on sub-wavelength grating waveguides. *Optics express*, 23(4):4791–4803, 2015.

[69] Zhengsen Ruan, Li Shen, Shuang Zheng, and Jian Wang. Subwavelength grating slot (swgs) waveguide on silicon platform. *Optics express*, 25(15):18250–18264, 2017.

[70] Alexey V Krasavin and Anatoly V Zayats. Silicon-based plasmonic waveguides. *Optics express*, 18(11):11791–11799, 2010.

[71] Graham T Reed, G Mashanovich, F Yand Gardes, and DJ Thomson. Silicon optical modulators. *Nature photonics*, 4(8):518, 2010.

[72] Francesco Giuseppe Della Corte, Massimo Merenda, Giuseppe Cocorullo, Mario Iodice, Ivo Rendina, and Pasqualina M Sarro. Modulation speed improvement in a fabry-perot thermo-optical modulator through a driving signal optimization technique. *Optical Engineering*, 48(7):074601, 2009.

[73] Ansheng Liu, Richard Jones, Ling Liao, Dean Samara-Rubio, Doron Rubin, Oded Cohen, Remus Nicolaescu, and Mario Paniccia. A high-speed silicon optical modulator based on a metal–oxide–semiconductor capacitor. *Nature*, 427(6975):615, 2004.

[74] Zhao Jiate, Zhao Yong, Wang Wanjun, Hao Yinlei, Zhou Qiang, Yang Jianyi, Wang Minghua, and Jiang Xiaoqing. Analysis of the thermo-optic effect in lateral-carrier-injection soi ridge waveguide devices. *Journal of Semiconductors*, 31(6):064009, 2010.

[75] Kapil Debnath, David J Thomson, Weiwei Zhang, Ali Z Khokhar, Callum Littlejohns, James Byers, Lorenzo Mastronardi, Muhammad K Husain, Kouta Ibukuro, Frederic Y Gardes, et al. All-silicon carrier accumulation modulator based on a lateral metal-oxide-semiconductor capacitor. *Photonics Research*, 6(5):373–379, 2018.

[76] María Félix Rosa, Lotte Rathgeber, Raik Elster, Niklas Hoppe, Thomas Föhn, Martin Schmidt, Wolfgang Vogel, and Manfred Berroth. Design of a carrier-depletion mach-zehnder modulator in 250 nm silicon-on-insulator technology. *Advances in Radio Science*, 15:269–281, 2017.

[77] Hong C Nguyen, Satoshi Hashimoto, Mizuki Shinkawa, and Toshihiko Baba. Compact and fast photonic crystal silicon optical modulators. *Optics express*, 20(20):22465–22474, 2012.

[78] Stefan Wolf, Heiner Zwickel, Clemens Kieninger, Matthias Lauermann, Wladislaw Hartmann, Yasar Kutuvantavida, Wolfgang Freude, Sebastian Randel, and Christian Koos. Coherent modulation up to 100 gbd 16qam using silicon-organic hybrid (soh) devices. *Optics express*, 26(1):220–232, 2018.

[79] Weijie Chang, Xinshu Ren, Yingquan Ao, Longhui Lu, Mengfan Cheng, Lei Deng, Deming Liu, and Minming Zhang. Inverse design and demonstration of an ultracompact broadband dual-mode 3 db power splitter. *Optics express*, 26(18):24135–24144, 2018.

[80] Liangshun Han, Bill P-P Kuo, Nikola Alic, and Stojan Radic. Ultra-broadband multimode 3db optical power splitter using an adiabatic coupler and a y-branch. *Optics express*, 26(11):14800–14809, 2018.

[81] Ruixuan Chen, Qingzhong Deng, and Zhiping Zhou. Ultra low loss asymmetric multimode interference power splitters. In *2018 IEEE 15th International Conference on Group IV Photonics (GFP)*, pages 1–2. IEEE, 2018.

[82] Isa Kiyat, Atilla Aydinli, and Nadir Dagli. A compact silicon-on-insulator polarization splitter. *IEEE Photonics Technology Letters*, 17(1):100–102, 2005.

[83] Junbo Yang, Zhengzheng Shao, Kuo Zhou, Suzhi Xu, and Jia Xu. High performance and compact polarization beam splitter based on silicon-on-insulator subwavelength grating coupler. In *2013 International Conference on Optical Instruments and Technology: Micro/Nano Photonics and Fabrication*, volume 9047, page 90470D. International Society for Optics and Photonics, 2013.

[84] Wei Yang, Yue Xu, Yanping Li, Xingjun Wang, and Ziyu Wang. A compact and wide-band polarization beam splitter based on wedge-shaped mmi coupler in silicon-on-insulator. In *Optical Fiber Communication Conference*, pages W2A–12. Optical Society of America, 2015.

[85] Yule Xiong, Dan-Xia Xu, Jens H Schmid, Pavel Cheben, Siegfried Janz, and N Ye Winnie. Fabrication tolerant and broadband polarization splitter and rotator based on a taper-etched directional coupler. *Optics express*, 22(14):17458–17465, 2014.

[86] Hakki H Refai, James J Sluss, and Monte P Tull. Digital micromirror device for optical scanning applications. *Optical Engineering*, 46(8):085401, 2007.

[87] Jihwan Kim, Chulwoo Oh, Michael J Escuti, and Steve Serati. Wide-angle nonmechanical beam steering using thin liquid crystal polarization gratings. In *Advanced Wavefront Control: Methods, Devices, and Applications VI*, volume 7093, page 709302. International Society for Optics and Photonics, 2008.

[88] Cui Zheng. Nanofabrication: principles, capabilities and limits. *Springer, Germany*, 2008.

[89] David Attwood and Anne Sakdinawat. *X-rays and Extreme Ultraviolet Radiation: Principles and Applications*. Cambridge university press, 2017.

[90] Kurt Ronse. Optical lithography—a historical perspective. *Comptes Rendus Physique*, 7(8):844–857, 2006.

[91] R Fabian Pease and Stephen Y Chou. Lithography and other patterning techniques for future electronics. *Proceedings of the IEEE*, 96(2):248–270, 2008.

[92] Yong Chen and Anne Pepin. Nanofabrication: Conventional and nonconventional methods. *Electrophoresis*, 22(2):187–207, 2001.

[93] Thomas T Hill. Introduction to photographic principles (larmore, lewis), 1967.

[94] X Hiao. *Introduction to semiconductor manufacturing technology*. Prentice Hall, 2000.

[95] Daniel P Sanders. Advances in patterning materials for 193 nm immersion lithography. *Chemical reviews*, 110(1):321–360, 2010.

[96] Burn-Jeng Lin. Immersion lithography and its impact on semiconductor manufacturing. *Journal of Micro/Nanolithography, MEMS, and MOEMS*, 3(3):377–501, 2004.

[97] Alongkorn Pimpin and Werayut Srituravanich. Review on micro-and nanolithography techniques and their applications. *Engineering Journal*, 16(1):37–56, 2012.

[98] Peipei Liang, Zhifeng Gan, and Qiang Wu. Challenges and solutions of few-line patterns with freeform illumination in immersion lithography. In *Semiconductor Technology International Conference (CSTIC), 2018 China*, pages 1–3. IEEE, 2018.

[99] Jung Sik Kim and Jinho Ahn. Mask materials and designs for extreme ultra violet lithography. *Electronic Materials Letters*, pages 1–15, 2018.

[100] Chris A Mack. *Field guide to optical lithography*, volume 6. SPIE Press Bellingham, WA, 2006.

[101] Takakazu Kimoto, Takehiko Naruoka, Hisashi Nakagawa, Tomohisa Fujisawa, Motohiro Shiratani, Tomoki Nagai, Ramakrishnan Ayothi, Yoshi Hishiro, Masafumi Hori, Kenji Hoshiko, et al. Novel euv resist development for sub-14nm half pitch. *Journal of Photopolymer Science and Technology*, 28(4):519–523, 2015.

[102] Henry I Smith and Franco Cerrina. X-ray lithography for ulsi manifacturing. *Microlithography world*, 6(1):10, 1997.

[103] AF Mayadas and RB Laibowitz. One-dimensional superconductors. *Physical Review Letters*, 28(3):156, 1972.

[104] Kenji Yamazaki and Hideo Namatsu. 5-nm-order electron-beam lithography for nanodevice fabrication. *Japanese journal of applied physics*, 43(6S):3767, 2004.

[105] Ranveig Flatabø, Akshay Agarwal, Richard Hobbs, Martin M Greve, Bodil Holst, and Karl K Berggren. Exploring proximity effects and large depth of field in helium ion beam lithography: large-area dense patterns and tilted surface exposure. *Nanotechnology*, 29(27):275301, 2018.

[106] Marek Edward Schmidt, Takuya Iwasaki, Manoharan Muruganathan, Mayeesha Haque, Huynh Van Ngoc, Shinichi Ogawa, and Hiroshi Mizuta. Structurally controlled large-area 10 nm pitch graphene nanomesh by focused helium ion beam milling. *ACS applied materials & interfaces*, 10(12):10362–10368, 2018.

[107] Rosa Cordoba, Alfonso Ibarra, Dominique Mailly, and Jose Ma De Teresa. Vertical growth of superconducting crystalline hollow nanowires by he+ focused ion beam induced deposition. *Nano letters*, 18(2):1379–1386, 2018.

[108] Jordi Llobet, Gemma Rius, Alex Chuquitarqui, Xavier Borrisé, R Koops, M van Veghel, and F Perez-Murano. Arrays of suspended silicon nanowires defined by ion beam implantation: mechanical coupling and combination with cmos technology. *Nanotechnology*, 29(15):155303, 2018.

[109] Heinz D Wanzenboeck and Simon Waid. Focused ion beam lithography. In *Recent Advances in Nanofabrication Techniques and Applications*. InTech, 2011.

[110] PFA Alkemade and H Miro. Focused helium-ion-beam-induced deposition. *Applied Physics A*, 117(4):1727–1747, 2014.

[111] S Dworetsky, R Novick, WW Smith, and N Tolk. Electron bombardment ion source for low energy beams. *Review of Scientific Instruments*, 39(11):1721–1723, 1968.

[112] LW Swanson. Liquid metal ion sources: Mechanism and applications. *Nuclear Instruments and Methods in Physics Research*, 218(1-3):347–353, 1983.

[113] W Driesel, Ch Dietzsch, and R Mühle. In situ observation of the tip shape of auge liquid alloy ion sources using a high voltage transmission electron microscope. *Journal of Vacuum Science & Technology B: Microelectronics and Nanometer Structures Processing, Measurement, and Phenomena*, 14(5):3367–3380, 1996.

[114] Richard H Livengood, Shida Tan, Roy Hallstein, John Notte, Shawn McVey, and FHM Faridur Rahman. The neon gas field ion source—a first characterization of neon nanomachining properties. *Nuclear Instruments and Methods in Physics Research Section A: Accelerators, Spectrometers, Detectors and Associated Equipment*, 645(1):136–140, 2011.

[115] Gowa Tomoko, Tomohiro Takahashi, Toshitaka Oka, Takashi Murakami, Akihiro Oshima, Seiichi Tagawa, and Masakazu Washio. Ion beam irradiation effects on resist materials. *Journal of Photopolymer Science and Technology*, 23(3):399–404, 2010.

[116] Khalil Arshak, Miroslav Mihov, Shohei Nakahara, Arous Arshak, and Declan McDonagh. A novel focused-ion-beam lithography process for sub-100 nanometer technology nodes. *Superlattices and Microstructures*, 36(1-3):335–343, 2004.

[117] Anders Persson, Greger Thornell, and Hugo Nguyen. Rapid prototyping of magnetic tunnel junctions with focused ion beam processes. *Journal of Micromechanics and Microengineering*, 20(5):055039, 2010.

[118] Christian Boit, Rudolf Schlangen, Uwe Kerst, and Ted Lundquist. Physical techniques for chip-backside ic debug in nanotechnologies. *IEEE Design & Test of Computers*, 25(3):250–257, 2008.

[119] Ivo Utke, Patrik Hoffmann, and John Melngailis. Gas-assisted focused electron beam and ion beam processing and fabrication. *Journal of Vacuum Science & Technology B: Microelectronics and Nanometer Structures Processing, Measurement, and Phenomena*, 26(4):1197–1276, 2008.

[120] Marc A McCord and Michael J Rooks. Electron beam lithography. In *Handbook of Microlithography, Microfabrication and Microsystems*. SPIE Press, 1997.

[121] Stuart Boden and Xiaoqing Shi. Helium ion beam lithography for sub-10 nm pattern definition. *SPIE Newsroom*, 2017.

[122] THP Chang. Proximity effect in electron-beam lithography. *Journal of vacuum science and technology*, 12(6):1271–1275, 1975.

[123] LD Jackel, RE Howard, PM Mankiewich, HG Craighead, and RW Epworth. Beam energy effects in electron beam lithography: The range and intensity of backscattered exposure. *Applied Physics Letters*, 45(6):698–700, 1984.

[124] KJ Polasko, YW Yau, and RFW Pease. Low energy electron beam lithography. In *Submicron Lithography I*, volume 333, pages 76–83. International Society for Optics and Photonics, 1982.

[125] Xiaoxiang Xia, Haifang Yang, Zongli Wang, Yunlong Li, Zheng Cui, Yifang Chen, and Changzhi Gu. Fabrication of near-infrared and optical metamaterials on insulating substrates by lift-off using pmma/al stack. *Microelectronic engineering*, 84(5-8):1144–1147, 2007.

[126] Carl zeiss microscopy gmbh. https://www.zeiss.com/microscopy/int/products/scanning-electron-micoscopes/geminisem.html. Accessed: 2018-10-10.

[127] Paddy French, Gijs Krijnen, and Fred Roozeboom. Precision in harsh environments. *Microsystems & nanoengineering*, 2:16048, 2016.

[128] Frederik C Krebs. Fabrication and processing of polymer solar cells: a review of printing and coating techniques. *Solar energy materials and solar cells*, 93(4):394–412, 2009.

[129] Elba Gomar-Nadal, Josep Puigmartí-Luis, and David B Amabilino. Assembly of functional molecular nanostructures on surfaces. *Chemical Society Reviews*, 37(3):490–504, 2008.

[130] Jaleh Mansouri, Evi Yapit, and Vicki Chen. Polysulfone filtration membranes with isoporous structures prepared by a combination of dip-coating and breath figure approach. *Journal of membrane science*, 444:237–251, 2013.

[131] Levich Landau and B Levich. Dragging of a liquid by a moving plate. In *Dynamics of Curved Fronts*, pages 141–153. Elsevier, 1988.

[132] Jeffrey C Brinker. Dip coating. In *Chemical solution deposition of functional oxide thin films*, pages 233–261. Springer, 2013.

[133] K Norrman, A Ghanbari-Siahkali, and NB Larsen. 6 studies of spin-coated polymer films. *Annual Reports Section" C"(Physical Chemistry)*, 101:174–201, 2005.

[134] Marc J Madou. *Manufacturing techniques for microfabrication and nanotechnology*, volume 2. CRC press, 2011.

[135] Microchem. https://microchem.com/Prod-PMMA.html. Accessed: 2018-10-12.

[136] J Thornton. Physical vapor deposition. In *Semiconductor Materials and Process Technology Handbook*. Noyes Publications, 1988.

[137] Aída Serrano Rubio. *Modified Au-based nanomaterials studied by surface plasmon resonance spectroscopy*. Springer, 2015.

[138] Stephen Rossnagel. Sputtering and sputter deposition. In *Handbook of Thin Film Deposition Processes and Techniques (Second Edition)*, pages 319–348. Elsevier, 2001.

[139] Ronald Powell and Stephen Rossnagel. *PVD for Microelectronics: Sputter Deposition Applied to Semiconductor Manifacturing*. Elsevier, 1999.

[140] Daniel Dobkin and Michael K Zuraw. *Principles of chemical vapor deposition*. Springer Science & Business Media, 2003.

[141] Caroline Elizabeth Knapp. *Synthesis, chemical vapour deposition and structural studies of group 13 alkoxides*. PhD thesis, UCL (University College London), 2010.

[142] A Stoffel, A Kovacs, W Kronast, and B Müller. Lpcvd against pecvd for micromechanical applications. *Journal of Micromechanics and Microengineering*, 6(1):1, 1996.

[143] Frank Jansen. Plasma-enhanced chemical vapor deposition. In *Handbook of Vacuum Science and Technology*. Academic Press, 1998.

[144] Gary S May and Costas J Spanos. *Fundamentals of semiconductor manufacturing and process control*. John Wiley & Sons, 2006.

[145] AK Paul, K Sodhi, AK Dimri, PC Banerjie, and RP Bajpai. Reactive ion etching (rie) system design and its characterisation. *IETE Technical Review*, 15(1-2):49–54, 1998.

[146] Daniel L Flamm, Vincent M Donnelly, and John A Mucha. The reaction of fluorine atoms with silicon. *Journal of applied physics*, 52(5):3633–3639, 1981.

[147] DL Flamm, CJ Mogab, and ER Sklaver. Reaction of fluorine atoms with sio2. *Journal of Applied Physics*, 50(10):6211–6213, 1979.

[148] TJ Chuang. Electron spectroscopy study of silicon surfaces exposed to xef2 and the chemisorption of sif4 on silicon. *Journal of Applied Physics*, 51(5):2614–2619, 1980.

[149] Kazuo Nojiri. Mechanism of dry etching. In *Dry Etching Technology for Semiconductors*, pages 11–30. Springer, 2015.

[150] JW Coburn. Plasma-assisted etching. *Plasma Chemistry and Plasma Processing*, 2(1):1–41, 1982.

[151] Hojoon Lee and Samuel Wood. Optimization of reactive ion etching (rie) parameters for selective removal of mosfet gate dielectric and evaluation of its physical and electrical properties. *Journal of Undergraduate Research at Minnesota State University, Mankato*, 11(1):5, 2011.

[152] Mihai Lazar, Heu Vang, Pierre Brosselard, Christophe Raynaud, P Cremillieu, J-L Leclercq, A Descamps, Sigo Scharnholz, and Dominique Planson. Deep sic etching with rie. *Superlattices and microstructures*, 40(4-6):388–392, 2006.

[153] John Chalmers and Peter Griffiths. *Handbook of Vibrational Spectroscopy, 5 volumes set.* Wiley, 2002.

[154] DF Swinehart. The beer-lambert law. *Journal of chemical education*, 39(7):333, 1962.

[155] Jiri Homola, Sinclair S Yee, and Gunter Gauglitz. Surface plasmon resonance sensors. *Sensors and Actuators B: Chemical*, 54(1-2):3–15, 1999.

[156] M Janneh, A De Marcellis, E Palange, AT Tenggara, and D Byun. Design of a metasurface-based dual-band terahertz perfect absorber with very high q-factors for sensing applications. *Optics Communications*, 416:152–159, 2018.

[157] WJ Padilla, MT Aronsson, C Highstrete, Mark Lee, AJ Taylor, and RD Averitt. Electrically resonant terahertz metamaterials: Theoretical and experimental investigations. *Physical Review B*, 75(4):041102, 2007.

[158] Frank Neubrech, Christian Huck, Ksenia Weber, Annemarie Pucci, and Harald Giessen. Surface-enhanced infrared spectroscopy using resonant nanoantennas. *Chemical reviews*, 117(7):5110–5145, 2017.

[159] Ronen Adato, Serap Aksu, and Hatice Altug. Engineering mid-infrared nanoantennas for surface enhanced infrared absorption spectroscopy. *Materials today*, 18(8):436–446, 2015.

[160] Lukas Novotny. Effective wavelength scaling for optical antennas. *Physical Review Letters*, 98(26):266802, 2007.

[161] Ronen Adato, Ahmet A Yanik, and Hatice Altug. On chip plasmonic monopole nano-antennas and circuits. *Nano letters*, 11(12):5219–5226, 2011.

[162] Jharna Paul, M Richard, and Nigel P Johnson. Gold asymmetric-split ring resonators (a-srrs) for proteins sensing. In *Metamaterials X*, volume 9883, page 98831C. International Society for Optics and Photonics, 2016.

[163] Frank Neubrech, Annemarie Pucci, Thomas Walter Cornelius, Shafqat Karim, Aitzol García-Etxarri, and Javier Aizpurua. Resonant plasmonic and vibrational coupling in a tailored nanoantenna for infrared detection. *Physical review letters*, 101(15):157403, 2008.

[164] Kai Chen, Thang Duy Dao, and Tadaaki Nagao. Tunable nanoantennas for surface enhanced infrared absorption spectroscopy by colloidal lithography and post-fabrication etching. *Scientific Reports*, 7:44069, 2017.

[165] Pedro Baptista, Eulália Pereira, Peter Eaton, Gonçalo Doria, Adelaide Miranda, Inês Gomes, Pedro Quaresma, and Ricardo Franco. Gold nanoparticles for the development of clinical diagnosis methods. *Analytical and bioanalytical chemistry*, 391(3):943–950, 2008.

[166] Shahin Bagheri, Ksenia Weber, Timo Gissibl, Thomas Weiss, Frank Neubrech, and Harald Giessen. Fabrication of square-centimeter plasmonic nanoantenna arrays by femtosecond direct laser writing lithography: effects of collective excitations on seira enhancement. *ACS Photonics*, 2(6):779–786, 2015.

[167] Ronen Adato and Hatice Altug. In-situ ultra-sensitive infrared absorption spectroscopy of biomolecule interactions in real time with plasmonic nanoantennas. *Nature communications*, 4:2154, 2013.

[168] L Businaro, O Limaj, V Giliberti, M Ortolani, A Di Gaspare, G Grenci, Gabriele Ciasca, A Gerardino, A De Ninno, and S Lupi. Mid-infrared nanoantenna arrays on silicon and caf2 substrates for sensing applications. *Microelectronic Engineering*, 97:197–200, 2012.

[169] A De Marcellis, E Palange, M Janneh, C Rizza, A Ciattoni, and S Mengali. Design optimisation of plasmonic metasurfaces for mid-infrared high-sensitivity chemical sensing. *Plasmonics*, 12(2):293–298, 2017.

[170] Jorge Zuloaga, Emil Prodan, and Peter Nordlander. Quantum plasmonics: optical properties and tunability of metallic nanorods. *ACS nano*, 4(9):5269–5276, 2010.

[171] Jorg Bochterle, Frank Neubrech, Tadaaki Nagao, and Annemarie Pucci. Angstrom-scale distance dependence of antenna-enhanced vibrational signals. *ACS nano*, 6(12):10917–10923, 2012.

[172] Huanjun Chen, Xiaoshan Kou, Zhi Yang, Weihai Ni, and Jianfang Wang. Shape-and size-dependent refractive index sensitivity of gold nanoparticles. *Langmuir*, 24(10):5233–5237, 2008.

[173] Fardad Koohyar, Abbas Ali Rostami, Mohammad Javad Chaichi, and Farhoush Kiani. Refractive indices, viscosities, and densities for l-cysteine hydrochloride monohydrate+ d-sorbitol+ water, and glycerol+ d-sorbitol+ water in the temperature range between t= 303.15 k and t= 323.15 k. *Journal of solution chemistry*, 40(7):1361–1370, 2011.

[174] Blake N Johnson and Raj Mutharasan. Regeneration of gold surfaces covered by adsorbed thiols and proteins using liquid-phase hydrogen peroxide-mediated uv-photooxidation. *The Journal of Physical Chemistry C*, 117(3):1335–1341, 2013.

[175] Frank Neubrech, Sebastian Beck, Tobias Glaser, Mario Hentschel, Harald Giessen, and Annemarie Pucci. Spatial extent of plasmonic enhancement of vibrational signals in the infrared. *ACS nano*, 8(6):6250–6258, 2014.

[176] Microchem. https://microchem.com/pdf/PMMA_Data_sheet.pdf. Accessed: 2018-10-17.

[177] Cristiano D'Andrea, Jorg Bochterle, Andrea Toma, Christian Huck, Frank Neubrech, Elena Messina, Barbara Fazio, Onofrio M Marago, Enzo Di Fabrizio, Marc Lamy de La Chapelle, et al. Optical nanoantennas for multiband surface-enhanced infrared and raman spectroscopy. *ACS nano*, 7(4):3522–3531, 2013.

[178] Rostislav Bukasov, Tamer A Ali, Peter Nordlander, and Jennifer S Shumaker-Parry. Probing the plasmonic near-field of gold nanocrescent antennas. *Acs Nano*, 4(11):6639–6650, 2010.

[179] Daehan Yoo, Daniel A Mohr, Ferran Vidal-Codina, Aurelian John-Herpin, Minsik Jo, Sunghwan Kim, Joseph Matson, Joshua D Caldwell, Heonsu Jeon, Ngoc-Cuong Nguyen, et al. High-contrast infrared absorption spectroscopy via mass-produced coaxial zero-mode resonators with sub-10 nm gaps. *Nano letters*, 18(3):1930–1936, 2018.

[180] Martina Abb, Yudong Wang, Nikitas Papasimakis, CH De Groot, and Otto L Muskens. Surface-enhanced infrared spectroscopy using metal oxide plasmonic antenna arrays. *Nano letters*, 14(1):346–352, 2013.

[181] Ari Sihvola. Metamaterials in electromagnetics. *Metamaterials*, 1(1):2–11, 2007.

[182] Kan Yao and Yongmin Liu. Plasmonic metamaterials. *Nanotechnology Reviews*, 3(2):177–210, 2014.

[183] Saman Jahani and Zubin Jacob. All-dielectric metamaterials. *Nature nanotechnology*, 11(1):23, 2016.

[184] Hou-Tong Chen, Willie J Padilla, Joshua MO Zide, Arthur C Gossard, Antoinette J Taylor, and Richard D Averitt. Active terahertz metamaterial devices. *Nature*, 444(7119):597, 2006.

[185] Simone Raoux. Phase change materials. *Annual Review of Materials Research*, 39:25–48, 2009.

[186] A Zakery and SR Elliott. An introduction to chalcogenide glasses. *Optical Nonlinearities in Chalcogenide Glasses and Their Applications*, pages 1–28, 2007.

[187] Ran-Young Kim, Ho-Gi Kim, and Soon-Gil Yoon. Structural properties of ge 2 sb 2 te 5 thin films by metal organic chemical vapor deposition for phase change memory applications. *Applied Physics Letters*, 89(10):102107, 2006.

[188] Tun Cao, Chenwei Wei, Robert E Simpson, Lei Zhang, and Martin J Cryan. Rapid phase transition of a phase-change metamaterial perfect absorber. *Optical Materials Express*, 3(8):1101–1110, 2013.

[189] Stephen E Harris, JE Field, and A Imamoğlu. Nonlinear optical processes using electromagnetically induced transparency. *Physical Review Letters*, 64(10):1107, 1990.

[190] E Petronijevic and C Sibilia. All-optical tuning of eit-like dielectric metasurfaces by means of chalcogenide phase change materials. *Optics express*, 24(26):30411–30420, 2016.

[191] Emilija Petronijevic. *Nanostructured semiconductor-based surfaces for nanoscale light manipulation.* PhD thesis, University of Rome "La Sapienza", 2017.

[192] E Carria, AM Mio, S Gibilisco, M Miritello, C Bongiorno, MG Grimaldi, and E Rimini. Amorphous-crystal phase transitions in gexte1-x alloys. *Journal of The Electrochemical Society*, 159(2):H130–H139, 2011.

[193] Emilija Petronijevic, Grigore Leahu, Valentina Di Meo, Alessio Crescitelli, Principia Dardano, Giuseppe Coppola, Emanuela Esposito, Ivo Rendina, Maria Miritello, Maria G Grimaldi, and Concita Sibilia. Eit-like all-dielectric metamaterials with phase changing layers for all-optical switching applications. In *19th Italian National Conference on Photonic Technologies*, pages 1–4. IET, 2017.

[194] H Gokan, S Esho, and Y Ohnishi. Dry etch resistance of organic materials. *Journal of the electrochemical Society*, 130(1):143–146, 1983.

[195] Yuanmu Yang, Ivan I Kravchenko, Dayrl P Briggs, and Jason Valentine. All-dielectric metasurface analogue of electromagnetically induced transparency. *Nature communications*, 5:5753, 2014.

[196] Behrad Gholipour, Jianfa Zhang, Kevin F MacDonald, Daniel W Hewak, and Nikolay I Zheludev. An all-optical, non-volatile, bidirectional, phase-change meta-switch. *Advanced materials*, 25(22):3050–3054, 2013.

[197] KS Andrikopoulos, SN Yannopoulos, GA Voyiatzis, AV Kolobov, Michel Ribes, and J Tominaga. Raman scattering study of the a-gete structure and possible mechanism for the amorphous to crystal transition. *Journal of Physics: Condensed Matter*, 18(3):965, 2006.

[198] Yaguang Yang. Analytic solution of free space optical beam steering using risley prisms. *Journal of Lightwave Technology*, 26(21):3576–3583, 2008.

[199] Yuichi Ninomiya. Ultrahigh resolving electrooptic prism array light deflectors. *IEEE Journal of Quantum Electronics*, 9(8):791–795, 1973.

[200] F Vasey, FK Reinhart, R Houdre, and JM Stauffer. Spatial optical beam steering with an algaas integrated phased array. *Applied optics*, 32(18):3220–3232, 1993.

[201] Paul F McManamon, Philip J Bos, Michael J Escuti, Jason Heikenfeld, Steve Serati, Huikai Xie, and Edward A Watson. A review of phased array steering for narrow-band electrooptical systems. *Proceedings of the IEEE*, 97(6):1078–1096, 2009.

[202] DP Resler, DS Hobbs, RC Sharp, LJ Friedman, and TA Dorschner. High-efficiency liquid-crystal optical phased-array beam steering. *Optics letters*, 21(9):689–691, 1996.

[203] Hideo Kosaka, Takayuki Kawashima, Akihisa Tomita, Masaya Notomi, Toshiaki Tamamura, Takashi Sato, and Shojiro Kawakami. Superprism phenomena in photonic crystals. *Physical review B*, 58(16):R10096, 1998.

[204] Hideo Kosaka, Takayuki Kawashima, Akihisa Tomita, Masaya Notomi, Toshiaki Tamamura, Takashi Sato, and Shojiro Kawakami. Superprism phenomena in photonic crystals: Toward microscale lightwave circuits. *Journal of lightwave technology*, 17(11):2032–2038, 1999.

[205] Lijun Wu, Michael Mazilu, Tim Karle, and Thomas F Krauss. Superprism phenomena in planar photonic crystals. *IEEE Journal of Quantum Electronics*, 38(7):915–918, 2002.

[206] P Ciancia, I Rendina, G Cocorullo, and V Mocella. Revisiting the superprism effect: a theory close to the bragg condition. In *Integrated Optics: Physics and Simulations*, volume 8781, page 87811D. International Society for Optics and Photonics, 2013.

[207] John D Joannopoulos, Steven G Johnson, Joshua N Winn, and Robert D Meade. *Photonic crystals: molding the flow of light*. Princeton university press, 2011.

[208] André Authier. *Dynamical theory of X-ray diffraction*, volume 11. Oxford University Press on Demand, 2004.

[209] Max Born and Emil Wolf. *Principles of optics: electromagnetic theory of propagation, interference and diffraction of light*. Elsevier, 2013.

[210] Pierfelice Ciancia. Sistema di beam-steering non meccanico in ottica integrata. Master's thesis, University of Calabria, 2012.

[211] Gary Lynn Harris. *Properties of silicon carbide*, volume 13. Iet, 1995.

[212] Bong-Shik Song, Shota Yamada, Takashi Asano, and Susumu Noda. Demonstration of two-dimensional photonic crystals based on silicon carbide. *Optics express*, 19(12):11084–11089, 2011.

[213] SN Tandon, M Soljačić, GS Petrich, JD Joannopoulos, and LA Kolodziejski. The superprism effect using large area 2d-periodic photonic crystal slabs. *Photonics and nanostructures-fundamentals and applications*, 3(1):10–18, 2005.

[214] Y Takagaki, E Wiebicke, H Kostial, and KH Ploog. Fabrication of ghz-range surface-acoustic-wave transducers on linbo3 using imprint lithography. *Nanotechnology*, 13(1):15, 2001.

Acknowledgments

The first person I would like to thank is my supervisor, Prof. Giuseppe Cocorullo, who gave me the opportunity to take the research path that brought me here. I would also like to thank Dr. Ivo Rendina, who build up the Unit of Naples of Institute for Microlectronics and Microsystems – National Council of Research (CNR – IMM), where I performed the experimental activities described into this thesis work. I would moreover like to express my deepest gratitude to Dr. Emanuela Esposito, who has guided me during the last four years through the nanofabrication world, and to Dr. Alessio Crescitelli, who supported and encouraged me during these years. In addition, I'm grateful to all my CNR – IMM colleagues, especially Dr. Silvia Romano, Dr. Vito Mocella, Eng. Giuseppe Coppola and Eng. Maurizio Casalino, for supporting me during the experimental work of this thesis.

I want also to thank all of the researchers with whom I collaborated, in particular Dr. Caterina Summonte, Prof. Elia Palange, Prof. Concita Sibilia and Prof. Maria Lepore.

In addition, I want to thank a lot Proff. Domenico Caputo and Giampiero de Cesare, who allowed me to temporary use their laboratory instruments when the machines I was using for the fabrication of the proposed nanostructures suffered an unexpected break. Thank you all for making it possible to achieve the results shown in this thesis.

Ringraziamenti

"E quindi uscimmo a riveder le stelle" (Inferno, XXXIV, 139).

Sono giunta alla fine di questo lungo percorso che, come tutti i percorsi importanti della vita, è stato un alternarsi di alti e bassi, di risate e di lacrime, di successi e fallimenti. La prima persona che sento di voler ringraziare sono io, per aver avuto la caparbietà di non mollare e di andare avanti, anche quando non vedevo spiragli di luce avanti a me.

Ringrazio Emanuela ed Alessio, che mi sono stati accanto, moralmente e professionalmente, sin dal primo momento in cui ci siamo conosciuti ed abbiamo iniziato il nostro percorso professionale insieme.

Ringrazio poi Nicola, che, quando "con gli occhi bassi stavo in fila con i disillusi, mi ha raccolto come un gatto e mi ha portato con sé". Ringrazio Peppe e Rosanna, per avermi accolta in casa come una figlia, e per aver avuto la pazienza di comprendere i miei sbalzi d'umore. Ringrazio anche Leonardo ed Ilaria, che insieme ai loro cuccioli hanno portato parecchie ventate d'allegria nella mia vita. Ovviamente una menzione speciale va a Nino, mio impeccabile aiutante durante la stesura di questa tesi, dolce scaldacollo e tenero giocherellone sempre in grado di strapparmi una risata.

Infine, il ringraziamento più caldo e sentito va alla mia famiglia, che da sempre mi sostiene, supporta, e soprattutto sopporta. Senza di voi non sarei la persona che sono e non avrei mai avuto la possibilità di essere dove sono. La famiglia non si sceglie, è quella che ci capita. Quello che però voi avete scelto indubbiamente è di essere le persone più presenti nella mia vita, pilastro fondamentale e luce guida anche nei momenti più bui. So che siete sempre al mio fianco, e so anche che non è scontato, per questo vi ringrazio di cuore, scusandomi per i momenti in cui tutto il mio affetto non è trasparso dai miei gesti.

Un grazie di cuore a tutti quelli che mi sono vicini in questo momento di gioia, e che condivideranno con me gli eventuali ulteriori successi che la vita mi riserverà.

Valentina